Technische Universität München
Fakultät für Chemie
Professur für Organische Chemie

Concurrent optimization of robust refocused pulse sequences for magnetic resonance spectroscopy

Wolfgang Kallies

Vollständiger Abdruck der von der Fakultät für Chemie der Technischen Universität München zur Erlangung des akademischen Grades eines

Doktors der Naturwissenschaften

genehmigten Dissertation.

Vorsitzender	Prof. Dr. Klaus Köhler
Prüfer der Dissertation	1. Prof. Dr. Steffen J. Glaser
	2. Prof. Dr. Bernd Reif

Die Dissertation wurde am 19.12.2017 bei der Technischen Universität München eingereicht und durch die Fakultät für Chemie am 14.03.2018 angenommen.

Concurrent optimization of robust refocused pulse sequences for magnetic resonance spectroscopy

Dissertation

angefertigt im Arbeitskreis
Organische Chemie

an der TU München

unter Betreuung von
Prof. Dr. S. J. Glaser

Wolfgang Kallies

1 Abstract

The Hahn echo experiment is one of the most common building blocks in magnetic resonance spectroscopy. It consists of an excitation and a refocusing pulse. Conventional approaches to improve the performance of echo experiments focused on the optimization of individual pulses. Here we present an approach to concurrently design both pulses such that they also compensate each others imperfections. Due to mutual error compensation Hahn echo performance is improved compared to conventional approaches.

Das Hahn Echo Experiment ist einer der gebräuchlichsten Pulsblöcke in der Magnetresonanzspektroskopie. Es besteht aus einem Anregungs- und einem Refokussierungspuls. Herkömmliche Anstze zur Optimierung der Transfereffizienz beschränkten sich auf die Optimierung einzelner Pulse. Hier beschreiben wir einen Ansatz zur gleichzeitigen Optimierung beider Pulse, deren Fehler sich gegenseitig kompensieren, sodass die Transfereffizienz verglichen mit herkömmlichen Ansätzen steigt.

Contents

Glossary

+1QF +1-Quantum Filter. 62, 64, 124

-1QF -1-Quantum Filter. 62, 124

BEBOP Broadband Excitation By Optimized Pulse. 27

BIBOP Broadband Inversion By Optimized Pulse. 27

BURBOP Broadband Universal Rotation By Optimized Pulse. 28

CPMG Carr-Purcell-Meiboom-Gill. 23, 31

cw continious wave. 13

DOF Degree Of Freedom. 17, 28

ENDOR Electron Nuclear DOuble Resonanc. 31

EPR Electron Paramagnetic Resonance. 13

ESEEM Electron Spin Echo Envelope Modulation. 31

GRAPE GRadient Ascent Pulse Engineering. 23, 24, 26

ICEBERG Inherent Coherence Evolution Broadband Excitation Resulting in constant phase Gradient. 27

INADEQUATE Incredible Natural-Abundance DoublE-QUAntum Transfer Experiment. 23, 31

INEPT Insensitive Nuclei Enhancement by Polarization Transfer. 14, 30

IR impulse response. 29

MRI Magnetic Resonance Imaging. 30

ms-coop Multi Scan COOPerative pulses. 28

MW MicroWave. 13

NMR Nuclear Magnetic Resonance. 13

PELDOR Pulsed ELectron DOuble Resonance. 31

PGSE Pulsed Gradient Spin Echo. 30, 31

PP Point-to-Point. 27, 28

RF Radiofrequency. 13, 14, 16

s^2 COOP same scan cooperative. 6, 29, 50, 52, 53, 57, 68–71, 74, 77, 123, 125

UR Universal Rotation. 28

WURST Wideband, Uniform Rate, Smooth Truncation. 24

ZQF Zero Quantum Filter. 59

Nomenclature

Physics

arg	argument of a complex number	
τ^{echo}	echo time	
τ^{sequence}	duration of pulse sequence	
B_0	strength of a constant external magnetic field	
B_1	strength of an oscillating external magnetic field	
γ	gyromagnetic ratio	
Φ	fidelity	
Ψ	wave function	
$\mathcal{H}^{\text{rot}}$	Hamiltonian in the rotating frame	
$\mathcal{H}_{\text{coupl}}$	coupling Hamiltonian	
$\mathcal{H}_{\text{cs}}$	chemical shift Hamiltonian	
$\mathcal{H}_{\text{rf}}$	radio frequency Hamiltonian	
$\mathcal{H}$	Hamiltonian	
H	Hamilton functional	
ν_{rf}	radio frequency amplitude	$\frac{1}{s}$
ω_{rf}	radio frequency amplitude	$\frac{\text{rad}}{s}$
ω^{res}	resonance angular velocity	$\frac{\text{rad}}{s}$
ρ	density matrix	
τ_p	pulse duration	
$S^{(1)}$	first pulse in a COBBLE or COBBLE3 sequence	
$S^{(2)}$	second pulse in a COBBLE or COBBLE3 sequence	
$S^{(3)}$	third pulse in a COBBLE3 sequence	

$T^{(1)}$ duration of first pulse in a COBBLE or COBBLE3 sequence

$T^{(2)}$ duration of second pulse in a COBBLE or COBBLE3 sequence

$T^{(3)}$ duration of third pulse in a COBBLE3 sequence

$\tau^{(1,2)}$ delay between $S^{(1)}$ and $S^{(2)}$ pulse in a COBBLE or COBBLE3 sequence

$\tau^{(2,3)}$ duration of pulse sequence

2 Publications

Parts of the thesis at hand are (in preparation to be) published in

1. W. Kallies, S. J. Glaser, Cooperative broadband spin echoes through optimal control, J Magn Reson 286, 2018, 115 - 137

2. S. Asami, W. Kallies, J. Günther, M. Stavropoulou, S. J. Glaser, M. Sattler, Ultrashort Broadband Cooperative Pulses for Multi-dimensional Biomolecular NMR Experiments, Angew Chem Int Ed, accepted

3. P. Spindler, P. Schöps, W. Kallies, S. J. Glaser, T. F. Prisner, Perspectives of shaped pulses for EPR spectroscopy, J Magn Reson 280, 2016, 30 - 45

4. F. M. Hrubesch, W. Kallies, L. Stelzer, S. J. Glaser, M. S. Brandt, Optimal Control Pulses for Electrically Detected Magnetic Resonance, in preparation

3 Introduction

Magnetic resonance spectroscopy is an analytic technique developed in the mid 20th century. Observations, that electrons and specific atomic nuclei possess a magnetic moment, were attributed to a property called spin, which is comparable to an intrinsic angular momentum.[1] In magnetic resonance spectroscopy, spin related properties of particles are examined, with or without the presence of an external magnetic field[2–5]

Experimentally magnetic resonance spectroscopy is implemented as either continious wave (cw) or pulsed spectroscopy. Here we focus on pulsed NMR experiments, where a sample is brought into a homogeneous magnetic field and exposed to a series of Radiofrequency (RF) pulses in Nuclear Magnetic Resonance (NMR) spectroscopy or MicroWave (MW) in Electron Paramagnetic Resonance (EPR) spectroscopy, whereupon a signal is acquired and analyzed.

Electromagnetic wave induced transfer between spin states is subject to apparatus limitations and imperfections and sample dependent. For example, in solution NMR, the sample is put into a glass tube and irradiated by an RF coil. Composition and thickness of the glass tube affects the field experienced by the sample. Furthermore, the field generated by the RF coils is not spatially homogeneous and local field densities and directions depend on the coil design.[6] The chemical environment influences spin dynamics as well.

Robust rf pulses steer spin systems from a given initial to a desired target state with close to ideal transfer efficiency for a broad range of the aforementioned conditions. Several approaches were employed to optimize robust individual pulses separately that tolerate said effects (see section 4.4). These individually optimized pulses are suitable for single pulse experiments as well as in multipulse experiments. However, in many multipulse experiments it is not necessary for *each individual pulse* to be perfect. The sequence as a whole has to provide sufficient transfer efficiency. Each of the individual pulses that make up the pulse sequence can be imperfect as long as their imperfections compensate each other.

In 2014, Braun et al. presented a method for optimizing a pulse train, where the errors of the individual pulses cancel each other.[7] The approach was applied to the Ramsey sequence with two $\pi/2$ pulses. We adapted the procedure for the nigh ubiquitious Hahn echo building block, which consists of a $\pi/2$ and a π pulse. Even though a corresponding numeric optimization scheme was successfully implemented, in contrast to said Ramsey sequence optimizations, the procedure got stuck in local maxima frequently. A heuristic approach was developped that allows for significantly faster convergence (c.f. section 6.2.3 and 7.1.2).

It is possible to incorporate effects of free evolution into a pulse. This has been applied to both individually as well as cooperatively optimized pulses and yielded substantial

gains in pulse performance both for individually optimized broadband excitation pulses [8] and concurrently optimized Ramsey sequences. [7] Inclusion of an auxiliary free evolution delay δ into Hahn echo sequences was investigated. Here, minor improvements of pulse sequence performance were found.

At a given radio frequency amplitude, the ideal ratio of pulse durations in a sequence of standard rectangular pulses can be determined analytically. For example, in a broadband Hahn echo experiment with a fixed maxmimum RF amplitude, the second pulse is twice as long as the first one. The duration of the first pulse is one third, the duration of the second pulse two thirds of the duration of the entire sequence. For concurrently optimized pulse trains the ideal ratio is *a priori* unknown. We suspected that the ideal ratio is tied to the amount of effective evolution into the pulse. Our findings are summarized in sec. 7.1.6.

We measured the performance of cooperatively optimized Hahn echo sequences against standard rectangular pulses as well as Hahn echoes comprised of individually optimized pulses of the same rf amplitude and pulse duration. The latter one include adiabatic chirp pulses according to the Böhlen-Bodenhausen scheme (sec. 4.3.3) and individually optimized pulses.

We found a slight gain in signal amplitude as well as massive improvements in phase adjustments for cooperatively optimized pulses (see section 7.1.6). Tests on a NMR spectrometer are in agreement with theoretical predictions.

Interpreting amplitude and phase modulated pulses is not straightforward in most cases. Joint time-frequency representations are intuitively interpretable representations for frequency-swept pulses. [9] Even though the amplitude and phase modulation of pulses optimized with a GRAPE algorithm in general are not simple frequency sweeps, spectrograms are generally more accessible than the intricate amplitude and phase modulations. In section 7.1.11 and 7.2.9 we provide joint time-frequency representations of cooperative sequences. An even simpler representation based on effective evolution times obtained from Euler angle decomposition is introduced in sections 6.2.5 and 6.3.5. which facilitates understanding pulse effects and cooperativity.

Some experiments require a Hahn echo building block complemented by a $\pi/2$ pulse, i.e. a $\frac{\pi}{2} - \pi - \frac{\pi}{2}$ sequence. Among them is the common Insensitive Nuclei Enhancement by Polarization Transfer (INEPT) building block in NMR for transferring magnetization from one spin to another as well as EPR echo experiments conducted by the group of M. Brandt, where final z-magnetization is detected. $\frac{\pi}{2} - \pi - \frac{\pi}{2}$ experiments could be conducted combining a cooperatively optimized Hahn echo sequence with an individually optimized pulse, however additional performance gains are expected if the entire sequence is optimized a whole.

For optimized $\frac{\pi}{2} - \pi - \frac{\pi}{2}$ pulse trains, similar analysis compared to Hahn echo sequences is conducted. The ideal ratio of pulse duration is examined as well as the performance compared to trains of conventional rectangular and individually optimized pulses. For application in experiments by our collaborators from the group of M. Brandt, pulse distortions by transient effects were considered and band-selective pulses were optimized. Findings are presented in section 7.2.

4 Theory

4.1 Basics of Magnetic Resonance Experiments

The discovery of nuclear spin started with the discovery of the hyperfine splitting in 1881.[10] In 1924, Wolfgang Pauli attributed them to an intrinsic angular momentum of the nuclei, which, as nuclei are charged particles, gives rise to a magnetic moment.[1,11] This intrinsic angular momentum is called spin. Pauli's findings are backed up by the Stern-Gerlach experiments conducted three years earlier. Otto Stern and Walther Gerlach sent atomic beams through an inhomogeneous magnetic field and observed, that the beam trajectories were altered by the magnetic field. In addition, the beam hit a detector at specific positions only. This confirmed that

1. atomic nuclei possess a magnetic moment.

2. The moment is quantized.

In 1946, Bloch and Purcell reported the observation of nuclear magnetic resonance through a current in an induction coil.[12,13] This technique, which was awarded a Nobel prize in 1952, is commonly used in NMR spectrometers nowadays.

4.1.1 Spectrum Acquisition

In the early days of magnetic resonance spectroscopy, continuous wave spectroscopy was heavily used for spectrum acquisiton in NMR and is still commonly employed in EPR today. However, in NMR spectroscopy, most experiments are pulsed experiments, and in EPR, pulsed spectroscopy is becoming more popular.[14] A short rf (or mw) pulse is applied to the system; in the case of NMR, thereupon a free induction decay is detected by a receiver coil.

4.1.2 Physical Background of NMR Transitions

4.1.2.1 Energy Levels in the Presence of an External Magnetic Field

In section 4.1, we established that particles possess a quantized intrinsic angular momentum called spin which gives rise to a magnetic moment. Projections of the angular momentum on cartesian axes are observable, commonly the z axis is chosen. For spin 1/2 particles, the projection can be $-1/2$ or $1/2$.

In the presence of an external magnetic field, the corresponding spin states undergo Zeeman splitting. The strength of the splitting depends on the strength of the external

magnetic field B_0 and on the gyromagnetic ratio γ of the particle in the field. The following condition specifies the allowed energy levels:

$$E = \pm\frac{1}{2}\hbar\gamma B_0. \tag{4.1}$$

In magnetic resonance spectroscopy, transitions between states are induced by photon (RF) irradiation.

4.1.2.2 Transition Rates

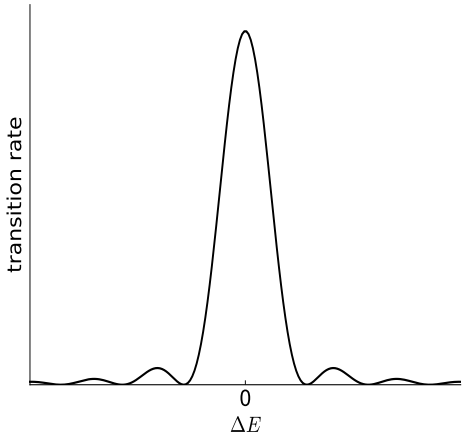

Figure 4.1: Here we show transition rates between states of energies E_1 and E_2 in the presence of an oscillating field with a frequency ν. ΔE satisfies $\Delta E = E_2 - E_1 + 2\pi\hbar\nu$.

During a magnetic resonance experiment, a sample is exposed to an oscillating magnetic and electric field. Quantum mechanical treatment of the interaction through time-dependent perturbation theory is well described in standard textbooks.[15] Transition rates between states of different energies E_1 and E_2 in the presence of an oscillating field are approximated by Fermi's golden rule:

$$w_{km}(\omega) \propto \frac{e^{i(\omega_{km}\pm\omega)\tau} - 1}{(\omega_{km} \pm \omega)}$$

Transitions occur between state k and state m. ω_{km} denotes the corresponding energy difference in multiples of $\hbar$, τ refers to the interaction time and ω to the angular velocity of the interacting oscillating field.

For sufficiently large interaction times τ, this can be rewritten as

$$w_{km}(\omega) \propto \delta(\omega_{km} \pm \omega)$$

where δ denotes the delta function. When the frequency of the oscillating field matches

the energy difference between two states, transition rates increase by orders of magnitude (Fig. 4.1).

4.1.3 Quantum Mechanical Treatment of the Dynamics of a System

A formalism for treating spin dynamics is required to conduct pulse sequence optimization. Here we briefly sum up the results, further in-depths treatment is provided in standard textbooks.[3,16,17] Bloch equations are a classical description and limited to uncoupled spin-$\frac{1}{2}$ systems. Coupled systems are considered in section 7.1.9. Therefore, a general quantum mechanical treatment for both coupled and uncoupled systems is briefly reviewed.

4.1.3.1 Quantum Mechanical Description of the State of a Spin System

According to the first postulate of quantum mechanics, the state of a system is fully characterized by a wave function $|\Psi\rangle$. This wave function is a function of all spatial and spin coordinates of all particles, i.e. nuclei and electrons, that constitute the observed system. In magnetic resonance spectroscopy, it is not necessary to consider all these DOF. Calculations are restricted to a reduced space with operators acting exclusively on spin variables. The remaining interactions are treated as generalized lattice.[3] This vastly reduces the demand for computational power.

For a spin-$\frac{1}{2}$ particle, there are two basis states: spin up ($|\alpha\rangle$) and spin down ($|\beta\rangle$). The corresponding wavefunction $|\Psi\rangle$ is made up of a linear combination of these basis states:

$$|\Psi\rangle = c_1 |\alpha\rangle + c_2 |\beta\rangle , \tag{4.2}$$

where c_1 and c_2 correspond to the projection of the whole wavefunction onto the respective basis state, i.e. the probability of finding the system in the respective state.

While some EPR experiments work with single spins,[18] most applications in NMR consider samples with $\approx 10^{18}$ spins. A common description of spin ensembles is given by the density operator formalism, which is employed in the thesis at hand. A densitiy matrix ρ is given by the outer product of the wave function

$$\rho = |\Psi\rangle \langle\Psi| . \tag{4.3}$$

When (4.2) is used in (4.3), we obtain:

$$\begin{aligned} \rho &= |\Psi\rangle \langle\Psi| \\ &= \begin{pmatrix} c_1 c_1^* & c_1 c_2^* \\ c_1^* c_2 & c_2 c_2^* \end{pmatrix} \end{aligned} \tag{4.4}$$

For an ensemble of spins, the averaged density operator ρ_{ensemble} describes the state of the system:

$$\rho_{\text{ensemble}} = \overline{\rho} \tag{4.5}$$

It is useful to employ a hermitian bases $\mathfrak{B} = \{\frac{1}{2}1, I_x, I_y, I_z\}$, where the basis states have real eigenvalues. The terms I_x, I_y, I_z refer to Pauli matrices.

$$\begin{aligned} I_x &= \frac{1}{2}\begin{pmatrix} 0 & 1 \\ 1 & 0 \end{pmatrix} \\ I_y &= \frac{1}{2}\begin{pmatrix} 0 & -i \\ i & 0 \end{pmatrix} \\ I_z &= \frac{1}{2}\begin{pmatrix} 1 & 0 \\ 0 & -1 \end{pmatrix} \end{aligned} \tag{4.6}$$

In the concurrent pulse optimization, raising and lowering operators I^+ and I^- are employed, which are constructed from the I_x and I_y matrices:

$$\begin{aligned} I^+ &= I_x + iI_y = \begin{pmatrix} 0 & 1 \\ 0 & 0 \end{pmatrix} \\ I^- &= I_x - iI_y = \begin{pmatrix} 0 & 0 \\ 1 & 0 \end{pmatrix} \end{aligned} \tag{4.7}$$

In analogy to wave functions, each state can be decomposed into its bases states. This is achieved by projecting on a basis state ψ_b. A scalar product can be defined as

$$\langle \psi_b | \rho \rangle = \text{Tr}\{\psi_b^\dagger \rho\}. \tag{4.8}$$

The projection of ρ onto basis states I_x, I_y and I_z equates to the magnitude of the components of the corresponding magnetization vector.

4.1.3.2 Quantum Mechanical Description of the Dynamics of a Spin System

In section 4.1.3.1 we established a description of the states of a spin system. Here, the dynamics of a spin system characterized by free evolution contributions and radio frequency irradiation are laid out.

The interactions within a spin system are defined by a Hamiltonian $\mathcal{H}$. Radio frequency terms are referred to as $\mathcal{H}_{\text{rf}}$, offset as $\mathcal{H}_{\text{off}}$ and coupling terms as $\mathcal{H}_{\text{coupl}}$.

$$\mathcal{H} = \mathcal{H}_{\text{rf}} + \mathcal{H}_{\text{off}} + \mathcal{H}_{\text{coupl}} \tag{4.9}$$

The time evolution of a spin system characterized by a state ρ under a Hamiltonian $\mathcal{H}$ is given by the Liouville-von Neumann equation:

$$\dot{\rho} = -\frac{i}{\hbar}[\mathcal{H}, \rho] \tag{4.10}$$

Note that from hereon we drop $\hbar$ of the Hamiltonion $\mathcal{H}$. The solution to this differential equation is given by the Heisenberg formalism:

$$\rho(t + \Delta t) = e^{-i\mathcal{H}t}\rho(t)e^{i\mathcal{H}t} \tag{4.11}$$

for time-constant Hamiltonians.

The components of the Hamiltonian $\mathcal{H}$ (c.f. 4.9) can be expressed in matrix representation:

$$\mathcal{H}_{\mathrm{rf}} \propto \cos(\omega_{\mathrm{rf}}t)I_x \tag{4.12}$$
$$\mathcal{H}_{\mathrm{off}} = \Sigma_i \omega_i I_{iz} \tag{4.13}$$
$$\mathcal{H}_{\mathrm{coupl}} = 2\pi\Sigma_{k<l} J_{k,l} I_k \otimes I_l \tag{4.14}$$

ω_{rf} represents the transmitter frequency at which the sample is irradiated. ω_i the resonance frequencies of spin i and $J_{k,l}$ the coupling constant between spin two spins I with axial vector components k and spin l.

Couplings ($\mathcal{H}_{\mathrm{coupl}}$) and, at a constant external field B_0, offset ($\mathcal{H}_{\mathrm{off}}$) are constant properties of a system and time independent; the expression for radio frequency irradiation ($\mathcal{H}_{\mathrm{rf}}$) is based on a linearly polarized wave. It corresponds to either continuous wave or a rectangular pulse with constant amplitude and phase. For simplicities sake, this example was chosen, later an expansion to shaped pulses is shown. The systems treated here require irradiation of a single spin only. For the uncoupled homonuclear and coupled heteronuclear systems that we consider here, further contributions to the radio frequency hamiltonian $\mathcal{H}_{\mathrm{rf}}$ are ignored.

Eq. (4.11) requires that the hamiltonian $\mathcal{H}$ is time independent. A time independent description is provided by choosing a frame of reference that oscillates at the transmitter frequency ω_{rf}. For the applications optimized for the thesis at hand, coupling contribtuions with $i \neq z$ in (4.14) are neglected. The time-dependent Hamiltonian $\mathcal{H}$ transforms as

$$\mathcal{H}^{\mathrm{rot}} = U\mathcal{H}U^{\dagger} \tag{4.15}$$
$$\mathcal{H}^{\mathrm{rot}}_{\mathrm{rf}} \propto I_x + \cos(2\omega t)I_x - i\sin(2\omega t)I_y \tag{4.16}$$
$$\mathcal{H}^{\mathrm{rot}}_{\mathrm{off}} = -\omega I_z + \Sigma_i \omega_i I_{iz} \tag{4.17}$$
$$\mathcal{H}^{\mathrm{rot}}_{\mathrm{coupl}} = 2\pi\Sigma_l J_{z,l} I_z \otimes I_l \tag{4.18}$$

and is denoted $\mathcal{H}^{\mathrm{rot}}$ in the rotating frame, where the transformation matrix U is given by

$$U = e^{-i\omega t I_z}.$$

The rf Hamiltonian contains a time dependent contribution oscillating at twice the speed of the transmitter frequency. As demonstrated in section 4.1.2.2, these contributions are negligibly small and may be disregarded. Therefore we find that

$$\mathcal{H}_{\mathrm{rf}}^{\mathrm{rot}} \propto I_x,$$

i.e. all contributions to the hamiltonian are time independent in case of constant amplitude and frequency of the emitter.

For shaped pulses, the emitter frequency and amplitude changes throughout the irradiation period. However, frequency changes can be translated into a phase modulation.

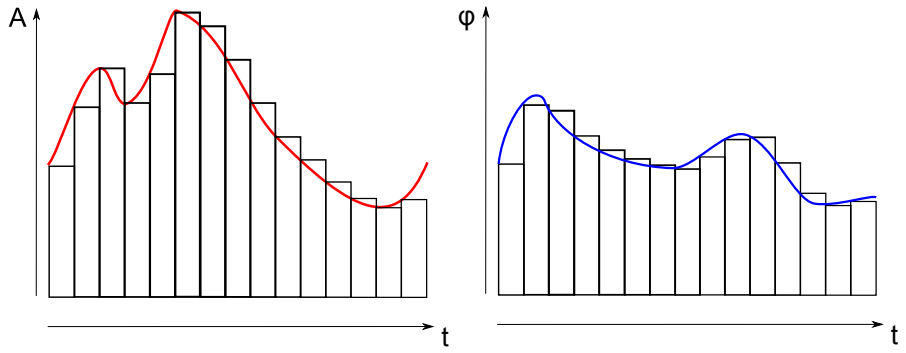

Figure 4.2: Graphical representation of the implementation of shaped pulses: an amplitude and frequency modulated pulse is expressed in terms of a time dependent amplitude (A) and phase (φ). The phase and amplitude shapes (or the corresponding x and y shapes) are discretized and approximated by piecewise constant time slices. This approximation is valid assuming time digitization is reasonably fine.

Figure 4.2 demonstrates how such a time dependent phase and amplitude modulation is treated: The shape is discretized into timeslices with a piecewise constant amplitude and phase. The Heisenberg formalism is applicable for computing the time evolution in each timeslice, For a shaped pulse discretized in n timesteps, the final state ρ_f is characterized by the propagation of the initial state ρ_0 under U_{tot}:

$$\rho_f = U_{\mathrm{tot}} \rho_0 U_{\mathrm{tot}}^{\dagger} \tag{4.19}$$

The overall propagator U_{eff} is the product of the individual propagators at timeslice i up until the final slice n:

$$U_{\mathrm{tot}} = U_n U_{n-1} \dots U_2 U_1 \tag{4.20}$$

4.2 Rotations in NMR

The transformations in NMR can be described as tensor transformations under rotations.[19] For the uncoupled spin $\frac{1}{2}$ case, in the absence of couplings, this includes the effects of rf pulses and offset and is equivalent to rotations of a vector on the Bloch sphere.

Here we summarize the transformation of the SU(2) rotation matrices into Euler angles and angle-axis parameters.[20–22]

Euler angles can be used to describe rotations in cartesian space.[19] Three successive rotations are carried out around cartesian axis, with no consecutive rotations around the same axis. Here, active rotations are used, where the magnetization vector is rotated as opposed to passive rotations which describe rotations of the coordinate system.[23] With three distinct cartesian axis, 12 unique active rotation descriptions exist. The most common decompostion in magnetic resonance spectroscopy is a zyz decomposition about the respective Euler angles γ, β and α.

The corresponding rotation matrix can be written as

$$U = \begin{pmatrix} \cos\left(\frac{\beta}{2}\right) e^{-i\frac{\alpha+\gamma}{2}} & -\sin\left(\frac{\beta}{2}\right) e^{-i\frac{\alpha-\gamma}{2}} \\ \sin\left(\frac{\beta}{2}\right) e^{i\frac{\alpha-\gamma}{2}} & \cos\left(\frac{\beta}{2}\right) e^{i\frac{\alpha+\gamma}{2}} \end{pmatrix} \tag{4.21}$$

Angle axis parameters are characterized by the x, y and z components n_x, n_y and n_z of a rotation axis and a corresponding flip angle Φ.[21]

$$U = \begin{pmatrix} \cos\left(\frac{\Phi}{2}\right) - in_z \sin\left(\frac{\Phi}{2}\right) & (-n_y + in_x)\sin\left(\frac{\Phi}{2}\right) \\ (n_y - in_x)\sin\left(\frac{\Phi}{2}\right) & \cos\left(\frac{\Phi}{2}\right) + in_z \sin\left(\frac{\Phi}{2}\right) \end{pmatrix}. \tag{4.22}$$

Here n_x, n_y and n_z correspond to the components of the rotation axis normalized such that

$$n_x^2 + n_y^2 + n_z^2 = 1.$$

4.3 Pulse Types

4.3.1 Motivation

In magnetic resonance spectroscopy and quantum computing, a spin system has to be driven from a given initial state ρ_0 into a target state ρ_t. Parts of the Hamiltonian may be known, i.e. the coupling Hamiltonian $\mathcal{H}_{\text{coupl}}$ or the chemical shift Hamiltonian $\mathcal{H}_{\text{cs}}$, or just a specific range these values might cover even though the exact property is unknown. These properties are sample inherent and cannot be changed at measurement time, i.e. they cannot be controlled. They are referred to as a *drift* part or *free evolution Hamiltonian*.[3,24]

Shaped pulses can compensate free evolution during a pulse. In the following the properties of rectangular and shaped pulses are briefly reviewed.

4.3.2 Rectangular Pulses

Rectangular pulses are the workhorse of magnetic resonance spectroscopy. A constant field is applied at a constant frequency for a short time. The flip angle β in radian is

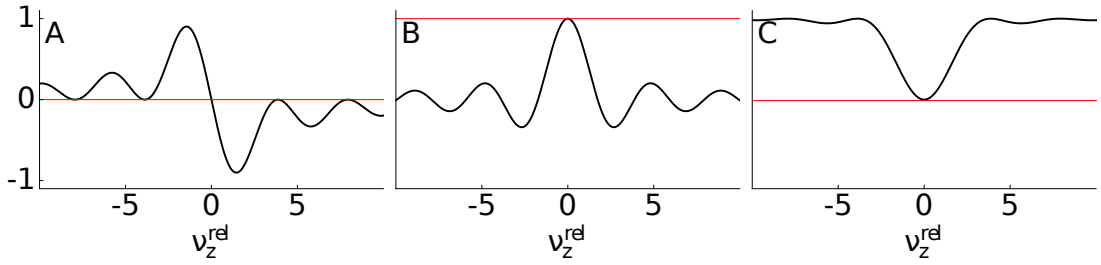

Figure 4.3: Excitation profile of a rectangular $\frac{\pi}{2}$ $-x$ pulse as a function of offset ν_z^{rel} relative to the amplitude. Plot A depicts x-magnetization, plot B y-magnetization and plot C z-magnetization. In each plot, the solid black line signifies the actual magnetization after the rectangular pulse, the solid red line refers to magnetization after an ideal δ pulse.

computed as

$$\beta = \tau_p \cdot \omega$$

where ω refers to the radio frequency amplitude in Hz and τ_p the pulse duration. The pulses are straightforward to implement on modern spectrometer hardware.

For broadband applications, it is desirable that the pulse mimics the behaviour of an ideal δ pulse with infinite amplitude ω and infinitely short duration τ_p. It is, however, not possible to create ideal δ pulses. Pulse power P is proportional the square of the amplitude A:

$$P \propto A^2 \tau_p$$

and is experimentally limited by the rf coil and in case of protein samples the temperature at which the structure of the biomolecule changes.

Broadband capabilities of a rectangular pulse are limited. Figure 4.3 shows the excitation profile of a rectangular pulse with a flip angle $\frac{\pi}{2}$ and a phase of $-x$. Ideally, for broadband applications, the excitation should be uniform across the entire observed bandwidth. Instead, a sinc shaped excitation profile with a full width half maximum at twice the pulse amplitude is created instead.

Within this region, considerable phase distortions are experienced, which results in dispersive line shapes in multidimensional spectra.[25]

For certain applications it is desirable to employ selective pulses, which affect only a certain bandwidth. The bandwidth of rectangular pulses can be tuned by adjusting the pulse duration. However, rectangular pulses generate side bands (c.f. Fig. 4.3).[25]

4.3.3 Shaped Pulses

The term 'shaped pulses' refers to amplitude and frequency modulated pulses, and spans a large variety of approaches. Feasible pulse shapes were extensively reviewed

before,[25–27] here we sum up properties of composite pulses which also apply to numerically GRAPE (GRadient Ascent Pulse Engineering) optimized pulses, pulse shapes obtained from closed function expressions, commonly used frequency swept pulses and pulses obtained through numeric optimization with GRAPE.

4.3.3.1 Composite Pulses

Composite pulses consist of a small number of subsequent rectangular pulses. Amplitude, phase and duration of each rectangular pulse differ. Design and use of composite pulses was first reported by Levitt et al.[28] This composite pulse consists of a π pulse, which is preceded and followed by a $\frac{\pi}{2}$ pulse, i.e. consists of three subpulses. Later, a composite pulse with nine subpulses was described by the same group.[29] For uncoupled spin $\frac{1}{2}$ systems, they are comparatively easy to model and understand.[30] Analytical expressions for the equation of motion are available: the dynamics consist of rotations on a (Bloch) sphere and can be modeled by Euler angles or quaternions.[20,31] This pulse class is robust to field inhomogeneities[29,30,32–40] and noise.[41]

They are implemented in the standard library of most modern NMR spectrometers. In addition, due to their relatively simple appearance, experimentalists are more inclined to employ them in their daily work.

Multipulse experiments that employ composite pulses include spin echoes,[32] Carr-Purcell-Meiboom-Gill (CPMG) sequences[42] and the Incredible Natural-Abundance DoublE-QUAntum Transfer Experiment (INADEQUATE) experiment.[43]

4.3.3.2 Arbitrarily Shaped Pulses

In section 4.1.3.2 it was mentioned that a shaped pulse is approximated by a series of rectangular pulses,i.e. arbitrary pulse shapes can be modeled by a composite pulses composed of sufficiently many subpulses. Many shapes are reported, sometimes with only slight variations of parameters.[26,27] Examples include, but are not limited to: sinc shapes, hermite shapes, Lorentians, gaussian pulses, hyperbolic secans, or Hanning shapes.[44]

4.3.3.3 Adiabatic Pulses

Adiabatic Pulses are a subclass of frequency swept pulses.[45] The adiabaticity criterion has to be met to classify pulses as adiabatic:

$$\frac{d\theta}{dt} \ll |\gamma| B_{\text{eff}}(\omega^{\text{res}}, t). \tag{4.23}$$

B_{eff} refers to the effective field a spin at resonance frequency ω^{res} experiences at a time t, and θ corresponds to the tangens of the angle between the effective field and the z axis.[27,46] Its time-derivative in (4.23) reflects the sweep rate. As long as the adiabaticity criterion is met, the flip angle is largely independent from the B_1 field strength, which makes this category of pulses appealing for systems with considerable B_1 inhomogeneities.[47]

Amplitude modulations corresponding to the aforementioned Lorentz, Hyperbolic Secant, Gauss, Hanning or constant windows are reported by Tannus and Garwood.[44] The corresponding phase modulation depends on the on the function chosen for the amplitude modulation.[14]

Here we focus on Wideband, Uniform Rate, Smooth Truncation (WURST) pulses first designed by Kupce et al.[48] This pulse class is commonly used in pulsed EPR experiments today which employ Hahn echo type transfer.[14]

The amplitude modulation of WURST pulses corresponds to chirp pulses with a linear frequency sweep. Their amplitude is modulated with a function of the form

$$\omega_1(t) = \omega_{\max} \cdot (1 - |\sin(\beta t)|^n) \tag{4.24}$$

The frequency offset $\Delta\omega$ is given by

$$\Delta\omega(t) = kt \tag{4.25}$$

n reflects the sharpness of the cutoff function, βt is set between $-\frac{\pi}{2}$ and $\frac{\pi}{2}$.

Chirp $\pi/2$ pulses generate a quadratic phase which cannot be compensated by setting the receiver phase or additional evolution. Böhlen and Bodenhausen showed that a second pulse with twice the sweep rate of the first pulse compensates the quadratic term.[49] Although this scheme creates a linearly offset-dependent phase over a range of offsets, it is susceptible to B_1 field inhomogeneities.[14] A three pulse sequence to mitigate these effects was developped by Shaka et al., however the increased pulse duration partly offsets the performance gains through increased robustness.

4.4 Pulse Optimization

4.4.1 General Remarks

In 4.1.3 we introduced shaped pulses as a series of subsequent rectangular pulses whose amplitude and phase are modulated to approximate the shapes introduced in section 4.3.3. When creating these shapes, we are tasked with the challenge to find suitable values for shape parameters. Here, suitable refers to robust pulses and pulse sequences and in case of $\frac{\pi}{2} - \pi - \frac{\pi}{2}$ sequences for EPR applications, band-selectivity.

Band-selective pulses can be optimized through linear response theory. Linear response theory states that the response y of a system to an input x is linear. For small flip angles we can identify y with the acquired signal and x with the pulse.[27]

For small flip angles and sufficiently off-resonant frequencies the approximation is valid and has been used in GRadient Ascent Pulse Engineering (GRAPE)-based pulse shaping to create selective pulses.[50] This approximation is not valid in the frequency range that should be excited.

Creating robust pulse shapes can be formulated as an optimal control problem. Here a control function $u(t)$ is optimized which steers a spin system from a given state $x(0)$ at time $t = 0$ into a specific target state $x(t_f)$ at a final time t_f.[51]

Optimal control problems are characterized by a cost functional J which is minimized. The cost functional $\mathcal{J}$ consists of a sum of a final cost functional ϕ and a running cost functional $\int_0^{t_f} \mathcal{L}$:

$$\mathcal{J} = \phi(x(t_f), t_f) + \int_0^{t_f} \mathcal{L}(t, x(t), u(t))dt \tag{4.26}$$

The optimization problem is constrained in that the dynamics are governed by the Liouville-von Neumann or the Bloch equations.

i constraints g_i, i.e. satisfaction of the Bloch equations or the Liouville-von Neumann equation are recognized in the Hamilton functional H:[52]

$$H = \mathcal{J} - \sum_i \lambda_i g_i, \tag{4.27}$$

where λ_i denotes the ith Lagrange multipliers and g_i the ith constraint. The optimization procedure is subject not only to constraints imposed by the physics of the system, but to technical constraints such as pulse power limits as well, which introduces additional Lagrange multipliers.

A suitable control has to fulfill the Pontryagin Minimum Principle:

$$H(\lambda, u, x) \geq H(\lambda, u_{\text{opt}}, x) \tag{4.28}$$

i.e. the Hamilton functional is minimized with respect to the controls u. Various strategies have been applied to find a pulse shape that satisfies (4.28).[27] In most cases a trial shape is assessed through the excitation profile obtained by the Bloch or the Liouville-von Neumann equation. An optimization algorithm is applied to improve the trial shape. The range of algorithms include standard optimization procedures such as the simplex algorithm, gradient based methods,[27] simulated annealing,[27] artificial neural networks,[27] genetic algorithms[53–56] or differential evolution.[57]

These types of optimization problems are generally well behaved, i.e. searches for local maxima end up in local maxima close to the ideal value. In the following we focus on gradient methods that work on pulse shapes that were discretized in n time slices, whose amplitude and phase modulation is characterized e.g. by one of the functions mentioned in section 4.3.3 with i free parameters k_i or by a set of i Fourier coefficients k_i.

1. Guess initial values for k_i.
2. Evaluate the final cost ϕ_{current} for the current set of controls.
3. If a stop criterion is met, break.
4. For each index i increment k_i by a small δ and evaluate the corresponding fidelity ϕ_i.

Table 4.1: Types of composite pulses described by Malcolm Levitt [29]

type	rotation	state-to-state transfer	uniform target phase
a	✓	✓	✓
b	✓	✓	X
c	X	✓	✓
d	X	✓	X

5. For each index i evaluate $\frac{d\phi}{dk_i} \approx \phi_i - \phi_{\text{current}}$.

6. For each index i, update k_i based on the gradient computed in 5.

7. Go to 2.

This algorithm is known as steepest descent and is linear in both i and n.[58] When i is increased, the amount of free parameters is increased; when n is increased, the time resolution is improved.

The thesis at hand focuses on optimizations of u_x and u_y for each individual time slice, i.e. where

$$i = 2n$$

and correspondingly a scaling $\mathcal{O}(n^2)$.

A linearly scaling gradient based optimization scheme based on Bloch equations was developed by Skinner and Glaser in 2003.[52] A general approach for arbitrary systems is presented in chapter 4.4.3 and 4.4.4.

4.4.2 Optimization Types

Levitt described four distinct types of robust composite pulses:[29]

- composite pulses whose corresponding effective rotation matrix matches a target rotation matrix (c.f. section 4.4.4), that carry out a specific rotation for all basis vectors.

- composite pulses that are optimized for the transformation of a single basis vector. (c.f. section 4.4.3)

In addition, he distinguished between uniform and non-uniform target phases (c.f. table 4.1).

Similar distinctions were made by Khaneja et al[59] for pulses optimized with the GRAPE algorithm. For robust broadband pulses a uniform target phase is required. Optimization of single pulses corresponding to case a and c are discussed in section 4.4.4 and 4.4.3 respectively.

4.4.3 State-to-State Optimization

Here we briefly review the optimization procedure provided by Khaneja et al.[59] for optimizations corresponding to Levitt's type c case, henceforth called Point-to-Point (PP) pulses. The transfer of a single basis vector is optimized, the behaviour of other states under the PP pulse is not considered in the optimization procedure and undefined.

Here a final state ρ_f is achieved by a pulse with an effective propagator U_{tot} from a given initial state $\rho(0)$:

$$\rho_f = U_{\text{tot}} \rho(0) U_{\text{tot}}^{\dagger} \tag{4.29}$$

A figure of merit Φ is given by the projection of the final state ρ_f onto the desired target state or costate λ_f :

$$\Phi = \langle \lambda_f | \rho_f \rangle \,. \tag{4.30}$$

A corresponding gradient is calculated as

$$\begin{aligned} \frac{\partial \Phi}{\partial u_x(t)} &= - \langle \lambda(t) | i \Delta t [I_x, \rho(t)] \rangle \\ \frac{\partial \Phi}{\partial u_y(t)} &= - \langle \lambda(t) | i \Delta t [I_y, \rho(t)] \rangle \,. \end{aligned} \tag{4.31}$$

$u_x(t)$ and $u_y(t)$ refer to the radio frequency components at at time t, $\lambda(t)$ to the costate at time t and $\rho(t)$ to the state at time t. $\rho(t)$ corresponds to the forward trajectory of the initial state and $\lambda(t)$ to the backward trajectory of the final state.

The computationally intensive time propagation of the initial and the final state need to be carried out once for the state ρ and once for the costate λ, i.e. the computational demand scales linearly with the number of timeslices n.

The GRAPE algorithm presented here implies updating all controls concurrently. In contrast, Krotov-type algorithms update them sequentially. Differences between the two were reviewed by Machnes et al.[60] Here we employ the former and do not elaborate on the latter.

Applications of PP pulses include excitation BEBOP and inversion Broadband Inversion By Optimized Pulse (BIBOP) pulses,[61–63] the former ones both without and with an auxiliary delay δ[8] in Inherent Coherence Evolution Broadband Excitation Resulting in constant phase Gradient (ICEBERG) pulses. Spin system parameters such as broad spin distributions[52,64] and relaxation effects were considered.[65–67] Individually optimized PP pulses were successfully employed as part of multipulse experiments.[68] Pulses for excitation of maximum quantum coherence, used in structure determination of large coupled systems,[69,70] were optimized with GRAPE by Köcher et al.[71]

4.4.4 Universal Rotation Optimization

Universal Rotation (UR) pulses correspond to Levitt's type *a* case. Whereas PP pulses are well defined for the transformation of a single state, UR pulses fix the transformation matrix, i.e. the transformation of all basis states is defined. Optimization was first conducted by Emsley and Bodenhausen,[72] here we review the method introduced by Khaneja et al.[59]

In the optimization of UR pulses, the fidelity Φ is given by the projection of the total propagator U_{tot} onto a target propagator U_t corresponding to the costate $\lambda(t_f)$:

$$\Phi = \langle U_{\text{tot}} | U_t \rangle = \langle U_{\text{tot}} | \lambda(t_f) \rangle \,. \tag{4.32}$$

A gradient is computed as

$$\begin{aligned} \frac{\partial \Phi}{\partial u_x(t)} &= -\text{Re}\{\langle U(t) | i\Delta t I_x \lambda(t) \rangle\} \\ \frac{\partial \Phi}{\partial u_y(t)} &= -\text{Re}\{\langle U(t) | i\Delta t I_y \lambda(t) \rangle\}. \end{aligned} \tag{4.33}$$

Properties and performance limits for broadband Broadband Universal Rotation By Optimized Pulse (BURBOP) were systematically studied by Kobzar et al.[73] UR pulses are more widely applicable than PP pulses at the expense of transfer efficiency at a given pulse duration.

In principle, broadband universal rotation pulses can also be constructed from broadband PP pulses,[74] however, individual optimization is more efficient.

Similar to ICEBERG pulses, coherence evolution can be included into the pulse, as has been examined by Köcher et al.[75] For the thesis at hand, π pulses have to be considered as refocusing pulses, for these, no gains were found for constant offset-dependent effective evolution.

In 2017, van Damme et al. presented an analytic solution for both broadband B_1 robust UR and PP pulses without considering an effective delay.[76]

4.4.5 Cooperative Optimization

Most NMR experiments consist of multiple pulses and data acquisition carried out over multiple scans. The signal is recorded after the last pulse, the data employed in the spectrum is a combination of the data of each scan. The overall fidelity is not directly dependent on the fidelity of each individual pulse, but on the entire sequence. Recently, general approaches for the concurrent optimization of cooperative pulses using optimal control methods were introduced.[7,77–81] Such cooperative pulses can exploit additional DOF which are provided by the fact that the individual pulses do not need to be perfect, provided the overall performance of the pulse sequences is optimized. It is useful to distinguish two types of cooperative pulses:

Multi Scan COOPerative pulses (ms-coop) pulses[78,80] are designed to provide close to ideal performance for the signal averaged over several scans and hence can be viewed

as a generalization of phase cycling and difference spectroscopy.[3]

s^2 *COOP*[7,77,79,81] are designed to compensate each others imperfections in a single scan and are the focus of this thesis. Singlescan COOP sequences can be optimized by inserting suitable filter elements between (composite or shaped) pulses, which depend on the specific application. For example, in the case of Ramsey-type sequences consisting of two 90° pulses, a single-quantum filter is used after the first pulse and a zero-quantum filter after the second pulse.[7,77]

The filters affect the dynamics of the system, i.e. the state $\rho(t)$ and the costate $\lambda(t)$. The algorithm presented in section 4.4.3 in Eq. (4.31) is directly applicable.

4.4.6 Optimization Procedure

The algorithm for gradient computation laid out in sections 4.4.3 and 4.4.4 is a first order approximation.[59] De Fouquières et al. demonstrated how to compute higher order gradients[82] and obtain convergence in less iterations at the expense of computational cost.

Convergence is also improved by turning from steepest descent to (pseudo-) Newton methods. The optimizations conducted here employed the L-BFGS-B algorithm implemented in IPOPT.[83]

Anand et al. and Goodwin et al. describe approaches to obtain the full Hessian with linear scaling.[84,85] Note that linear scaling refers to the regime where computation of forward and backward trajectory is computationally cheaper than computation of the n^2 elements in a Hessian with n controls. This may be the case at a few hundred timeslices with two controls each. For the optimizations conducted here we consider a few hundred time slices. Since no significant gains in wallclock time were expected, we chose not to implement analytic Hessians in the optimization procedure.

4.4.7 Compensation of transient effects

When spectrometer hardware is asked to generate e.g. a rectangular shape, the generated modulation does not strictly resemble the desired shape. The spectrometer does not switch from zero field strength to full rf (or mw) amplitude within an instant; it may overshoot and oscillate before reaching the desired rf power, i.e. the input controls u^{in} are distorted by the apparatus. This behaviour is characterized by an impulse response (IR). Assuming the distortions are linear, the output controls u^{out} can be characterized by folding with the IR:

$$\begin{aligned} u^{\mathrm{out}}(t) &= u^{\mathrm{in}}(t) * \mathrm{IR}(t) \\ &= \int_{-\infty}^{\infty} u^{\mathrm{in}}(\tau)\mathrm{IR}(t-\tau)d\tau \end{aligned} \tag{4.34}$$

where the time dependent controls $u(t)$ are treated as complex array:

$$u(t) = u_x(t) + iu_y(t) \tag{4.35}$$

In the frequency domain, a convolution becomes a multiplication:

$$f * g = \mathrm{IFFT}\{\mathrm{FFT}(f) \cdot \mathrm{FFT}(g)\} \tag{4.36}$$

Spindler et al.[86] suggested an optimization scheme for pulses that accomodate pulse distortions by the apparatus. Unfortunately, even though we tested the optimized pulses mentioned by Spindler et al., we were not able to reproduce their results. A more elaborate discussion is found in the methods section 6.3.7. We ultimately adapted the approach by Hincks et al.[87] Here, a distortion operator ϕ is constructed from the impulse response (IR), that transforms the input controls into the output controls:

$$u^{\mathrm{out}} = \phi u^{\mathrm{in}} \tag{4.37}$$

The corresponding input gradient is obtained by

$$\nabla u^{\mathrm{in}} = \phi^T \nabla u^{\mathrm{out}} \tag{4.38}$$

4.4.8 Software Packages that implement GRAPE

By now (October 2017) GRAPE is implemented in a variety of free open source software packages. The list includes (but is not limited to) Simpson[88] (written in C), QuTIP[89,90] (written in Python), DYNAMO[60] and Spinach[91] (both written in Matlab).

For the thesis at hand, the non-public optimization program OCTOPUS/Spinne was employed which is considerably faster for the examples considered here. The program was adapted to be capable of both individual as well as cooperative pulse optimization.

4.5 The Hahn Echo Experiment in Magnetic Resonance Spectroscopy

In 1950, Hahn discovered that two equally long rectangular pulses separated by an interpulse delay $\tau^{(1,2)}$ generated a signal, an echo, at

$$\tau^{\mathrm{sequence}} + \tau^{(1,2)}$$

where τ^{sequence} corresponds to the duration of the pulse sequence.

Spin echo can be created through gradient echos popular in Magnetic Resonance Imaging (MRI), three-pulse echoes and the two-pulse Hahn echo. The latter one consists of a PP excitation pulse and a UR π pulse.

It became a common building block in magnetic resonance spectroscopy and imaging. In nuclear magnetic resonance spectroscopy, it is employed e.g. in Pulsed Gradient Spin Echo (PGSE) experiments for diffusion measurements,[92–95] and in any experiment that contains an INEPT building block.[4,96–99]

Individually optimized (shaped) pulses have been applied in Hahn type experiments to supplant common rectangular pulses, e.g. composite pulses in Hahn echo experiments,[32]

CPMG[42] or an INADEQUATE experiment.[43]

Adiabatic chirp pulses generate a quadratic offset-dependent phase, Boehlen and Bodenhausen developped a scheme for broadband chirp excitation and refocusing pulse such that the quadratic phases of excitation and inversion pulse compensate each other.[49] Later on, Shaka et al. presented a sequence of chirp pulses that are robust towards B_1 inhomogeneities.[100] These were successfully applied in EPR.[101,102] Sets of GRAPE-optimized pulses for application in multidimensional NMR including Hahn-type transfers were successfully implemented and experimentally tested.[68]

In nuclear magnetic resonance imaging, the Hahn echo and the gradient echo are the basis of most experiment types.[103–107] For these applications, gradients are employed to phase- and frequency-encode spatial information. In turn slice selective pulses are required, as optimized by optimal control.[50,108] Applications include mostly soft tissues such as the liver,[109–114] the lung,[115] the brain[116,117] joints such as the knee[118–120] or the shoulder,[121] or blood vessels.[122]

In addition, Hahn type transfers are found in (pulsed) EPR spectroscopy.[123,124] The dynamics of electron spins occur on a different time scale than NMR transitions, but are guided by similar dynamics. As such, apparatus requirements are stricter, but some experiments resemble its NMR counterpart closely.[125–127]

Similar to NMR, Hahn echoes were used in conjunction with gradients for e.g. diffusion measurements in PGSE experiments.[128–130] Similar pulse and gradient trains are required for EPR imaging[131–134]

Further echo experiments that employ Hahn type transfers are Electron Spin Echo Envelope Modulation (ESEEM),[135,136] Pulsed ELectron DOuble Resonance (PELDOR) experiments for distance measurements in proteins,[137–140] or Electron Nuclear DOuble Resonanc (ENDOR) experiments for structure determination.[124,141]

Note that shaped pulses were employed in EPR for such experiments as well[101,142]

Different subclasses of Hahn-type experiments can be distinguished and impose different conditions for the cooperative optimization of the entire echo sequence. In some applications, such as dead time compensation or diffusion measurements with varying magnetic field gradients, only a single fixed delay is required. However, in many important applications, such as in the measurement of transverse relaxation[3] or in ESEEM,[124] it is desirable to have the ability to choose an arbitrary delay between the excitation and refocusing pulses, without the need to reoptimize the pulses. Furthermore, Hahn echo experiments can be performed with or without the application of crusher gradients or EXORCYCLE coherence transfer pathway selection.[2,103,143] Finally, Hahn-type sequences consisting of an excitation and refocusing pulse are also applied in heteronuclear spin systems to remove the effects of chemical shifts and/or couplings. Here, we focus on Hahn echo building blocks for uncoupled spins with variable delays in the presence of crusher gradients or EXORCYCLE coherence transfer pathway selection. In the following, we discuss the design of single-scan cooperative Hahn sequences and compare their performance to conventional echo sequences based on rectangular pulses and to echo sequences based on individually optimized excitation and refocusing elements.

5 Motivation

As outlined in section 4.5, the Hahn echo experiment is a widely applied building block in magnetic resonance spectroscopy. Due to its abundant occurrence in pulse sequences, it was chosen as a target for optimization. Even though an optimized Hahn echo sequence could be obtained combining individually optimized pulses, exploiting cooperativity provides additional degrees of freedom in the pulse sequence optimizaton, allowing for better performance at a given duration τ^{sequence} or by shorter pulse durations at a given fidelity compared to individually optimized pulses.

We show that as opposed to Ramsey-type sequences optimized with a similar approach, the algorithm presented in section 4.4.3 gets frequently stuck in local maxima. We suggest a pre-optimization scheme that shows improved convergence.

In a standard Hahn echo experiment with rectangular pulses at a given maximum amplitude, the π-refocusing pulse is twice as long as the excitation pulse. These relations do not necessarily hold up when investigating shaped pulses. Therefore we investigate the ideal ratio systematically.

It is possible to include the effect of external evolution into the pulse. Standard rectangular pulses inherently encompass effective evolution of $2/\pi \cdot \tau_p$.[144] Gershenzon et al. demonstrated that PP excitation pulses significantly improved including effective evolution into GRAPE-optimization.[8] Braun et al. included similar approaches for cooperatively optimized Ramsey-type sequences.[7] Köcher et al demonstrated, that no gain was to be expected for individually optimized refocusing pulses.[75] Cooperative Hahn echoes contain both PP as well as UR pulses. We systematically investigate the dependence of the transfer efficiency Φ as a function of both effective evolution as well as total pulse duration T^{tot} and the duration of the excitation pulse $T^{(1)}$ (and the corresponding duration of the refocusing pulse, which is fixed at a given total pulse duration T^{tot}).

Initial optimizations are conducted for uncoupled spin systems. The behaviour of shaped pulse sequences in the presence of coupling is not *a priori* known. Studying the effects of coupling on the pulse, assuming strong enough couplings that their effect during the irradiation period is non-negligible, is in order.

The spin dynamics in NMR and EPR are guided by similar principles. Hyperfine couplings in EPR, however, are described by more terms J-coupling in NMR in the weak-coupling limit. We further investigated the requirements in the optimization procedure for Hahn echo applications in EPR experiments and systematically studied sequences that were optimized for Ising coupling.

EDMR applications require $\frac{\pi}{2} - \pi - \frac{\pi}{2}$ type transfers. The first two pulses of this sequence constitute a Hahn echo, and supplanting these with cooperatively optimized broadband excitation pulses is a valid approach. However, larger gains are to be expected

when the entire sequence is optimized in a cooperative manner. We therefore conduct similar studies for the cooperatively optimized $\frac{\pi}{2} - \pi - \frac{\pi}{2}$ building block. It is not clear whether the properties of cooperative $\frac{\pi}{2} - \pi - \frac{\pi}{2}$ sequences are similar to cooperative Hahn echoes. For example, the ideal ratio of pulse durations within a cooperative Hahn echo might or might not be different from standard rectangular pulses, the ration of the ideal durations $T^{(1)}_{\frac{\pi}{2}-\pi-\frac{\pi}{2}}$, $T^{(2)}_{\frac{\pi}{2}-\pi-\frac{\pi}{2}}$ and $T^{(3)}_{\frac{\pi}{2}-\pi-\frac{\pi}{2}}$ of the three pulses that constitute a cooperative $\frac{\pi}{2} - \pi - \frac{\pi}{2}$ experiment might differ from the ideal ratio of $T^{(1)}_{\text{Hahn echo}}$ and $T^{(2)}_{\text{Hahn echo}}$.

We therefore conduct an indepth study of the properties of $\frac{\pi}{2} - \pi - \frac{\pi}{2}$ sequences similar to the analysis for Hahn echoes.

6 Methods

6.1 Computational Methods and Concepts

6.1.1 Computation of Euler angles

In section 4.2 we established that the unitary transformations which constitute NMR transitions can be expressed as Euler rotations. Here a scheme is lined out to obtain the Euler angles γ, β and α for a zyz rotation scheme with fixed axes, that acknowledges the inherent 4π-perodicity [145] of the underlying SU2 rotation matrices.

(4.21) established the relation between Euler angles and the SU2 rotation matrix: [21]

$$U = \begin{pmatrix} \cos\left(\frac{\beta}{2}\right) e^{-i\frac{\alpha+\gamma}{2}} & -\sin\left(\frac{\beta}{2}\right) e^{-i\frac{\alpha-\gamma}{2}} \\ \sin\left(\frac{\beta}{2}\right) e^{i\frac{\alpha-\gamma}{2}} & \cos\left(\frac{\beta}{2}\right) e^{i\frac{\alpha+\gamma}{2}} \end{pmatrix}$$

The matrix elements are identified by the complex-valued Caley-Klein parameters a and b as

$$U = \begin{pmatrix} a & b \\ -b^* & a^* \end{pmatrix} \tag{6.1}$$

We introduce the phases φ_a and φ_b corresponding to the arguments of the Caley-Klein parameters:

$$\varphi_a = \arg\{a\} \tag{6.2}$$
$$\varphi_b = \arg\{b\} \tag{6.3}$$

The Euler angles γ corresponding to first z-rotation, β to a y-rotation and α to the final z-rotation are given as

$$\alpha = -\varphi_a - \varphi_b + \pi \tag{6.4}$$
$$\beta = 2\,\mathrm{acos}(|a|) \tag{6.5}$$
$$\gamma = -\varphi_a + \varphi_b - \pi. \tag{6.6}$$

In order to map Euler angles into the ranges $0 \leq \alpha < 4\pi$, $0 \leq \beta \leq \pi$, and $0 \leq \gamma < 2\pi$, [146] we adjust the obtained results as follows:

- if $-\pi \leq \alpha < 0$, adjust $\alpha \to \alpha + 2\pi$ and $\gamma \to \gamma + 2\pi$.

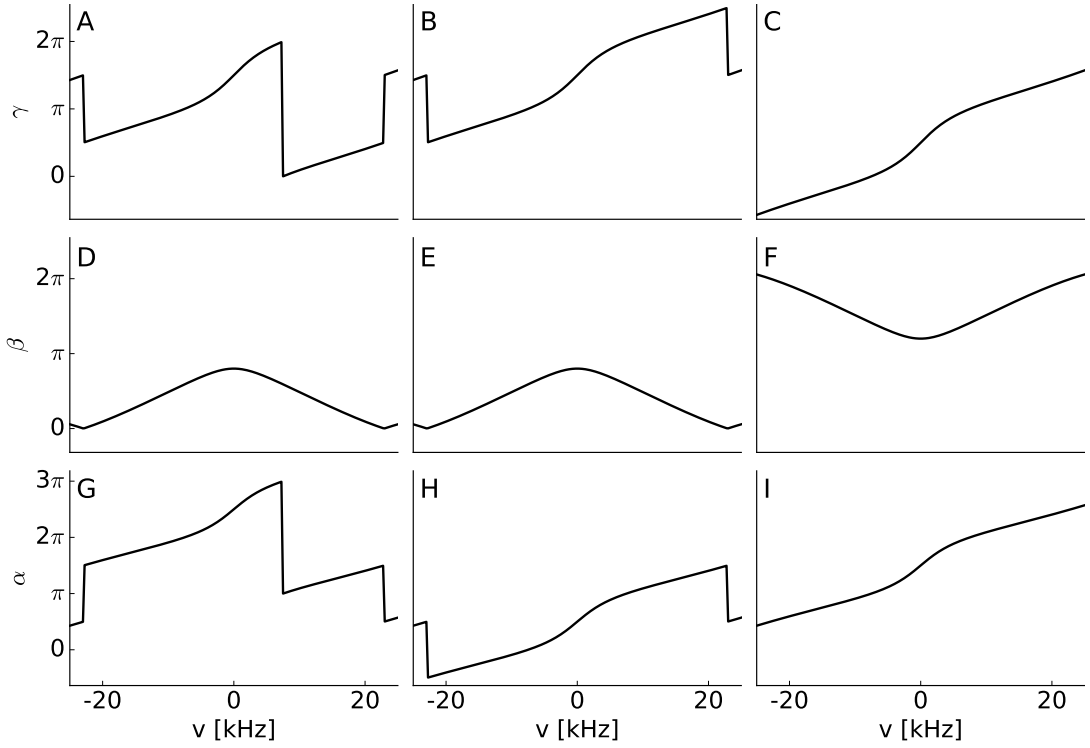

Figure 6.1: effect of unwrapping procedure on Euler angles γ (no unwrapping (A), step 1 (B) and step 3 (C)), β (no unwrapping (D), step 1 (E) and step 3 (F)) and α (no unwrapping (G), step 1 (H) and step 3 (I)) for a rectangular pulse with a pulse duration $\tau_p = 40$ μs at an amplitude $\nu^{\mathrm{rf}} = 10$ kHz.

- if $\alpha > 2\pi$, adjust $\alpha \to \alpha - 2\pi$ and $\gamma \to \gamma - 2\pi$.
- if $\gamma < 0$, adjust $\gamma \to \gamma + 4\pi$.

Note that any of these changes adjust $\alpha + \gamma$ by 4π and $\alpha - \gamma$ by 0. As such, the phase factor of the rotation matrix is maintained. β is not adjusted, since the acos function is positive and smaller than $\frac{\pi}{2}$ for arguments larger than 0.

As outlined in section 6.1.2, offset-dependent smoothly-varying Euler angles are required to determine effective evolution times. With the above scheme and confining Euler angles to the aforementioned intervals, phase jumps occur. We present an unwrapping procedure that maintaints the global phase of the propagator.

1. use a standard function (such as *numpy.unwrap* for python or *unwrap* in matlab) to unwrap the functions $\alpha(\nu)$ and $\gamma(\nu)$ by integer multiples of 2π

2. a) starting from the smallest offset (or from the last offset for which a discontinuity by π was detected), iterate through α until a discontinuity by π is found at a corresponding offset ω_j. If there are none, break.

   b) adjust $\alpha(\omega > \omega_j) \rightarrow \alpha(\omega > \omega_j) - \pi$
   c) adjust $\beta(\omega > \omega_j) \rightarrow 2\pi - \beta(\omega > \omega_j)$
   d) adjust $\gamma(\omega > \omega_j) \rightarrow \gamma(\omega > \omega_j) - \pi$
   e) go to 2(a)

3. use a standard function (such as *numpy.unwrap* for python or *unwrap* in matlab) to unwrap the functions $\alpha(\omega)$, $\beta(\omega)$, and $\gamma(\omega)$ by integer multiples of 2π

4. for one offset (e.g. $\omega : k = \omega_{\min}$), compare the pulse propagator $U(\omega_k)$ and the propagator $U'(\omega_k) = \exp\{-i\alpha(\omega_k)I_z\}\exp\{-i\beta(\omega_k)I_y\}\exp\{-i\gamma(\omega_k)I_z\}$. If $U(\nu_k) = -U'(\omega_k)$, $\alpha(\omega) \rightarrow \alpha(\omega) + 2\pi$ for all ω.

This procedure is motivated by the occurrence of two types of phase jumps:

1. phase jumps about 2π in $\alpha(\omega)$ and $\gamma(\omega)$

2. simultaneous phase jumps about π in $\alpha(\omega)$ and $\gamma(\omega)$ and change of the curvature of β

Type 1 phase jumps are removed by step 1, the type 2 by step 2. However step 2 is not guaranteed not to introduce phase jumps of type 1. They are removed by step 3.

Step 4 is necessary because the information about the global phase of the pulse propagators $U'(\omega)$ is not preserved by steps 1 and 3 and hence $U'(\omega)$ can be either $U(\omega)$ or $-U(\omega)$. Assuming the considered offset increments are small enough to provide smooth functions, $\alpha(\omega)$, $\beta(\omega)$, and $\gamma(\omega)$ after step 4, it is guaranteed that there is no discontinuity in the global phase factor of the pulse propagator and hence it is sufficient to consider only a single offset ω_k for the comparison of $U'(\omega)$ and $U(\omega)$.

Figure 6.1 demonstrates the effects of the unwrapping procedure on a rectangular pulse, leaving out the (trivial) step 3.

6.1.2 Computation of Effective Evolution Times

Effective evolution periods are calculated from Euler angles. As outlined in section 4.2, in the zyz Euler decomposition commonly used in magnetic resonance spectroscopy, for a given offset ω the effect of any (rectangular, composite or shaped) pulse on (uncoupled) spins can be decomposed into a rotation $\gamma_z(\omega)$ around the z axis, followed by a rotation $\beta_y(\omega)$ around the y axis, followed by a rotation $\alpha_z(\omega)$ around the z axis. Here, we reinterpret the offset-dependent angles $\gamma(\omega)$ and $\alpha(\omega)$ in terms of offset-dependent effective evolution periods $\tau_\gamma(\omega)$ and $\tau_\alpha(\omega)$ and offset-independent constant rotation angles γ_0 and α_0. For simplicity, here we focus on the Euler angle $\alpha(\omega)$, but the same arguments apply analogously to $\gamma(\omega)$. The angle $\alpha(\omega)$ can always be expressed in the form

$$\alpha(\omega) = \alpha_0 + \tilde{\alpha}(\omega).$$

The offset-independent angle

$$\alpha_0 = \alpha(0)$$

is given by the Euler angle α at offset $\omega = 0$ and the offset-dependent angle $\tilde{\alpha}(\omega) = \alpha(\omega) - \alpha_0$ can be expressed in the form

$$\tilde{\alpha}(\omega) = \omega \ \tau_\alpha(\omega).$$

Conversely, we can define

$$\tau_\alpha(\omega) = \frac{\tilde{\alpha}(\omega)}{\omega} \quad \text{for} \ \ \omega \neq 0. \tag{6.7}$$

Note that this definition is not unique, because the angle $\tilde{\alpha}(\omega)$ is equivalent to $\tilde{\alpha}(\omega) + n2\pi$, where n is an integer, c.f. supplementary material. For simplicity, here we disregard this subtlety. The definition of $\tau_\alpha(\omega)$ in Eq. (6.7) is valid, except for $\omega = 0$. This gap can be closed by interpolation of $\tau_\alpha(\omega)$ between $\omega = -\epsilon$ and $\omega = \epsilon$ for a small ϵ, i.e. $0 < \epsilon \ll 1$. Equivalently, $\tau_\alpha(0)$ can be defined as

$$\begin{aligned} \tilde{\alpha}(\omega) &= \omega\tau_\alpha(\omega) \\ \frac{d\tilde{\alpha}}{d\omega} &= \frac{d\omega\tau_\alpha(\omega)}{d\omega} \\ &= \underbrace{\omega\frac{d\tau_\alpha(\omega)}{d\omega}}_{=0 \text{ for } \omega=0} + \underbrace{\tau_\alpha(\omega)\frac{d\omega}{d\omega}}_{=\tau_\alpha(\omega)} \\ &\Updownarrow \\ \tau_\alpha(0) &= \frac{d\tilde{\alpha}(\omega)}{d\omega}|_0 \end{aligned} \tag{6.8}$$

Similarly, for the Euler angle γ we define

$$\begin{aligned} \gamma(\omega) &= \gamma_0 + \tilde{\gamma}(\omega) \\ \gamma_0 &= \gamma(0) \\ \tau_\gamma(\omega) &= \frac{\tilde{\gamma}(\omega)}{\omega} \quad \text{for} \ \ \omega \neq 0, \end{aligned} \tag{6.9}$$

and

$$\tau_\gamma(0) = \frac{d\tilde{\gamma}(\omega)}{d\omega}|_0. \tag{6.10}$$

Table 6.1: EXORCYCLE pulse and receiver phases to select ±2 coherence transfers

step	phase of $S^{(2)}$	receiverphase
1	0	0
2	90	180
3	180	0
4	270	180

6.2 Hahn echoes

6.2.1 Euler angle analysis of Hahn echo sequences

A thorough understanding of the degrees of freedom in a Hahn echo sequence is important for the design of optimal pulse sequences. Braun et al. analyzed Ramsey-type sequences (consisting of two 90° pulse blocks separated by a delay) in detail based on the Euler angle decomposition of the pulse blocks, which resulted in a lucid classification of Ramsey-type sequences.[7] Here we use a similar approach for the analysis of Hahn echo sequences consisting of a 90° excitation pulse and a 180° refocusing pulse block separated by a delay. The first and second pulses are denoted $S^{(1)}$ and $S^{(2)}$, respectively. The duration of the first pulse is $T^{(1)}$, the duration of the second pulse is $T^{(2)}$, and the total pulse duration is denoted

$$T^{tot} = T^{(1)} + T^{(2)}. \tag{6.11}$$

We call the delay between the end of the first pulse ($S^{(1)}$) and the beginning of the second pulse ($S^{(2)}$) $\tau^{(1,2)}$. The delay between the end of the second pulse $S^{(2)}$ and the time where the echo has its maximum is denoted τ^{echo} (c.f. 6.4).

The offset-dependent effect of the pulses $S^{(k)}$ (with $k \in \{1,\ 2\}$) can always be represented by three subsequent Euler rotations $\gamma_z^{(k)}(\omega)$, $\beta_y^{(k)}(\omega)$, $\alpha_z^{(k)}(\omega)$, around the (fixed) rotation axes z, y, and z,[20,21] as shown schematically in 6.3 A. In order to simplify the following derivations, here we assume that the offset-dependent Euler angles have been *unwrapped* such that they vary smoothly in the considered offset range of interest, see section 6.1.1 for a more detailed discussion of the unwrapping algorithm for the excitation and refocusing pulses.

During the delay between the two pulses, a spin with offset ω experiences a rotation by the angle $\omega\tau^{(1,2)}$ around the z axis (represented as $(\omega\tau^{(1,2)})_z$ in Fig. 6.3). After the end of the second pulse, the spin is rotated by $(\omega t)_z$. Coherence transfer pathway selection based on crusher gradients or EXORCYCLE (c.f. table 6.1) corresponds to the application of a +1-quantum filter (+1QF) after the excitation pulse $S^{(1)}$ and a −1-quantum filter (−1QF) before detection, c.f. dashed vertical lines in Fig. 6.2. (Note that the coherence order does not change during a delay without rf irradiation and hence a multiple-quantum filter has the same effect if it is applied at the beginning or at the end of a given delay). Using standard transformation rules for the operators I_z, I^+ and

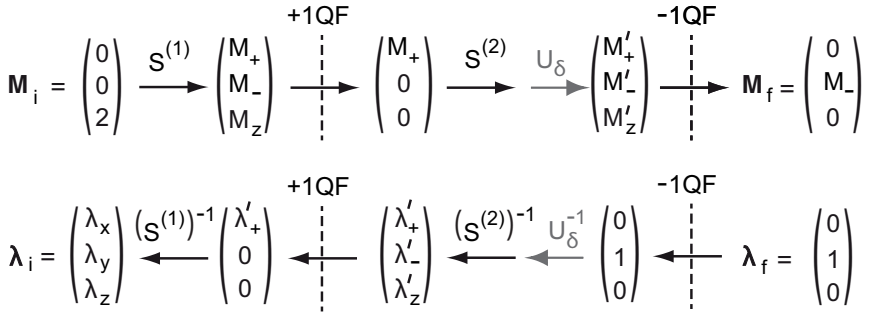

Figure 6.2: Schematic representation of the forward evolution of the magnetization vector M and the backward evolution of the co-state vector λ on which the GRAPE algorithm is based[7,59] for the case of a vanishing inter-pulse delay $\tau^{(1,2)}$. Here, the components of the vectors are the expectation values $\langle I^+\rangle$, $\langle I^-\rangle$, and $\langle I_z\rangle$.[147] $S^{(1)}$ and $S^{(2)}$ represent the propagators of the excitation and refocusing pulses to be optimized and $U_\delta = \exp(-\mathrm{i}\delta I_z)$ corresponds to the propagator of the auxiliary delay δ. (A dark grey font was used for the propagator U_δ to indicated that this step can be omitted in the optimization of the COOP_0 echo sequences of Fig. 1B. The dashed lines labeled "+1QF" and "−1QF" represent +1 and −1 quantum filters, respectively.

I^- under rotations around the z and y axis,[3] the transfer function s representing the transfer

$$2I_z \xrightarrow{\gamma_z^{(1)}} \xrightarrow{\beta_y^{(1)}} \xrightarrow{\alpha_z^{(1)}} \xrightarrow{\mathbf{+1QF}} \xrightarrow{(\omega\tau^{(12)})_z} \xrightarrow{\gamma_z^{(2)}} \xrightarrow{\beta_y^{(2)}} \xrightarrow{\alpha_z^{(2)}} \xrightarrow{\mathbf{-1QF}} \xrightarrow{(\omega t)_z} s\ I^- \tag{6.12}$$

between the initial state $2I_z$ before the first pulse and the −1-quantum filtered state at time t after the second pulse can be calculated in a straightforward way (c.f. 6.2.2) and results in

$$s(t,\omega) = -\sin\beta^{(1)}\sin^2\frac{\beta^{(2)}}{2}e^{-\mathrm{i}(\alpha^{(1)}+\omega\tau^{(1,2)}+\gamma^{(2)}-\alpha^{(2)}-\omega t)}, \tag{6.13}$$

with the offset-dependent Euler angles $\gamma_z^{(k)}(\omega)$, $\beta_y^{(k)}(\omega)$, $\alpha_z^{(k)}(\omega)$. Note that we have chosen the initial density operator $\rho(0) = 2I_z$ (rather than $\rho(0) = I_z$) in transformation (6.12) in order to normalize $s(t,\omega)$ such that it can reach a maximum value of 1.

For a given offset ω, the detected NMR signal at a given time t is proportional to this offset-dependent transfer function $s(t,\omega)$. The transfer function $s(t,\omega)$ is independent of the Euler angle $\gamma^{(1)}$, because the $\gamma_z^{(1)}$ rotation has no effect on initial z-magnetization. This is indicated schematically in Fig. 6.3 A by a darker box for the $\gamma_z^{(1)}(\omega)$ rotations. Fig. 6.3 shows the equivalent simplified scheme of Euler rotations for the two pulses and

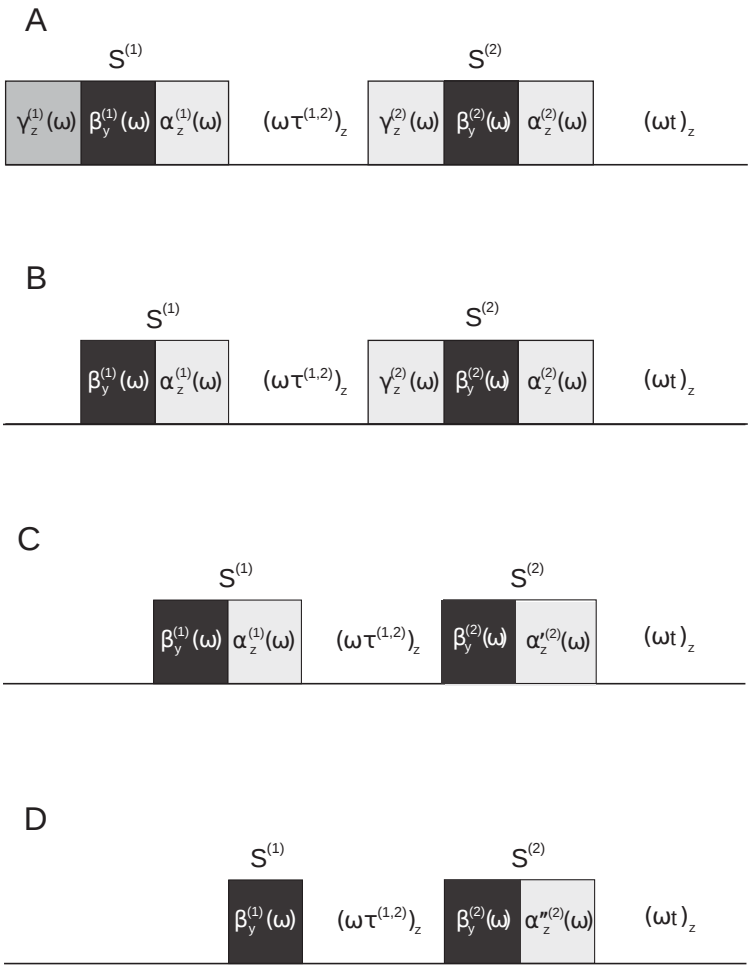

Figure 6.3: Characterization of general Hahn echo sequences based on the offset-dependent Euler angles of the excitation and refocusing pulses $S^{(1)}$ and $S^{(2)}$ and the offset-dependent z rotations during the delays $\tau^{(1,2)}$ and t. To guide the eye, the Euler rotations $\beta_y^{(1)}$ and $\beta_y^{(2)}$ are represented by black rectangles. (A) The first Euler rotation $\gamma_z^{(1)}$ (indicated by a dark grey rectangle) has no effect on initial z-magnetization and has been dropped in the simplified sequence of rotations shown in (B). This sequence can be further simplified by replacing the Euler angles $\gamma^{(2)}$ and $\alpha^{(2)}$ by the Euler angles $\alpha'^{(2)} = \alpha^{(2)} - \gamma^{(2)}$ and $\gamma'^{(2)} = 0$ (not shown), resulting in (C). Sequences (B) and (C) are equivalent in the presence of the +1 quantum filter before and a 1quantum filter after $S^{(2)}$ (or if $\beta^{(2)} = \pi$). Finally, in the presence of the $\pm$1-quantum filters (or for $\beta^{(2)} = \pi$), sequence (C) can be transformed to the equivalent sequence (D) by replacing the Euler angles $\alpha^{(1)}$ and $\alpha'^{(2)}$ by $\alpha''^{(1)} = 0$ (not shown) and $\alpha''^{(2)} = \alpha'^{(2)} - \alpha^{(1)}$.

of the z rotations during the delays. Due to the coherence order selection scheme, the transfer function $s(t,\omega)$ depends only on the difference $\gamma^{(2)}(\omega) - \alpha^{(2)}(\omega)$, i.e. the scheme of Fig.6.3 B can be further simplified to the scheme of Fig. 6.3 C, where the Euler angles $\gamma^{(2)}(\omega)$ and $\alpha^{(2)}(\omega)$ were replaced by the modified Euler angles

$$\alpha'^{(2)} = \alpha^{(2)} - \gamma^{(2)} \quad \text{and} \quad \gamma'^{(2)} = 0 \tag{6.14}$$

and (6.13) can be rewritten in the form

$$s(t,\omega) = -\sin\beta^{(1)} \sin^2 \frac{\beta^{(2)}}{2} e^{-\mathrm{i}(\omega(\tau^{(1,2)}-t)+\alpha^{(1)}-\alpha'^{(2)})}. \tag{6.15}$$

This can also be written in the form

$$s(t,\omega) = \sin\beta^{(1)} \sin^2 \frac{\beta^{(2)}}{2} e^{-\mathrm{i}(\omega(\tau^{(1,2)}-t)+\alpha^{(1)}-\alpha'^{(2)}+\pi)}, \tag{6.16}$$

where the minus sign has been absorbed in the exponential function by adding π in the exponent.

For a given range of offset frequencies $-\omega_{max} \leq \omega \leq \omega_{max}$, the total signal $s_{tot}(t)$ is given by integrating over the individual signals at each offset:

$$s_{tot}(t) = \int_{-\omega_{\max}}^{\omega_{\max}} s(t,\omega) d\omega, \tag{6.17}$$

(assuming for simplicity a constant spin density as a function of offset). An echo is formed at $t = \tau^{\text{echo}}$ if the signals $s(t,\omega)$ add up constructively. This is the case if the phase factor $\exp\{-\mathrm{i}(\omega(\tau^{(1,2)} - \tau^{\text{echo}}) + \alpha^{(1)}(\omega) - \alpha'^{(2)}(\omega) + \pi\}$ in Eq. (6.15) is offset-independent. Hence, the following echo condition must be fulfilled:

$$\omega(\tau^{(1,2)} - \tau^{\text{echo}}) + \alpha^{(1)}(\omega) - \alpha'^{(2)}(\omega) + \pi \stackrel{!}{=} \text{const} = \varphi_{\text{echo}}, \tag{6.18}$$

where φ_{echo} is the phase of the echo. For example, if the echo is formed along the x or $-x$ axis, φ_{echo} is 0 or π, respectively. (Note that the left and right sides of Eq. (6.18) only need to be identical up to multiples of 2π. For simplicity the corresponding modulus operator is suppressed and is assumed to be taken implicitly into account).

Without restriction of generality, for simplicity we assume in the following that we want to form the echo along the $-x$ axis, i.e. $\varphi_{\text{echo}} = \pi$. Based on (6.18), an auxiliary offset-dependent echo delay $\tau^{\text{echo}}(\omega)$ can be defined as

$$\tau^{\text{echo}}(\omega) = \tau^{(1,2)} + \frac{\alpha^{(1)}(\omega) - \alpha'^{(2)}(\omega)}{\omega}. \tag{6.19}$$

Following the approach by Braun et al.,[7] this expression can be further simplified by decomposing the offset-dependent Euler angles in

$$\alpha^{(1)}(\omega) = \alpha^{(1)\text{lin}}(\omega) + \alpha^{(1)\text{nl}}(\omega) \tag{6.20}$$

and

$$\alpha'^{(2)}(\omega) = \alpha'^{(2)\mathrm{lin}}(\omega) + \alpha'^{(2)\mathrm{nl}}(\omega), \tag{6.21}$$

where the linear parts $\alpha^{(1)\mathrm{lin}}(\omega)$ and $\alpha'^{(2)\mathrm{lin}}(\omega)$ are proportional to ω and the proportionality factors can be interpreted as effective delays defined as

$$\tau_\alpha^{(1)\mathrm{lin}} = \frac{\alpha^{(1)\mathrm{lin}}}{\omega}, \tag{6.22}$$

$$\tau_\alpha'^{(2)\mathrm{lin}} = \frac{\alpha'^{(2)\mathrm{lin}}}{\omega}. \tag{6.23}$$

The remaining terms $\alpha^{(1)\mathrm{nl}}(\omega)$ and $\alpha'^{(2)\mathrm{nl}}(\omega)$ consist of terms with non-linear dependence on ω and possible offset independent terms $\alpha_0^{(k)}$ and $\gamma_0'^{(k)}$. With these definitions, the general expression for the offset-dependent delay $\tau^{\mathrm{echo}}(\omega)$ can be written based on (6.19) in the form

$$\tau^{\mathrm{echo}}(\omega) = \tau^{(1,2)} + \delta + \epsilon(\omega) \tag{6.24}$$

with the offset-independent auxiliary delay

$$\delta = \tau_\alpha^{(1)\mathrm{lin}} - \tau_\alpha'^{(2)\mathrm{lin}} \tag{6.25}$$

and the offset-dependent delay

$$\epsilon(\omega) = \frac{\alpha^{(1)\mathrm{nl}}(\omega) - \alpha'^{(2)\mathrm{nl}}(\omega)}{\omega}. \tag{6.26}$$

For an ideal Hahn echo, an offset-independent echo delay τ^{echo} is required, and hence the echo condition of Eq. (6.18) can be reduced to the condition $\epsilon(\omega) = 0$.

This analysis forms the basis for a classification of different families of Hahn echo sequences with different constraints imposed on the Euler angles of the excitation and refocussing pulse.

Before we proceed to consider these sequence families, we summarize the conditions for ideal Hahn echo sequences:

$$\beta_{\mathrm{ideal}}^{(1)}(\omega) = \frac{\pi}{2}, \tag{6.27}$$

$$\beta_{\mathrm{ideal}}^{(2)}(\omega) = \pi, \tag{6.28}$$

$$\epsilon_{\mathrm{ideal}}(\omega) = 0. \tag{6.29}$$

Conditions (6.27) and (6.28) maximize the terms $\sin\beta^{(1)}$ and $\sin^2\frac{\beta^{(2)}}{2}$ in Eq. (6.16), respectively. The general echo condition (6.29) requires that the difference of the non-linear terms $\alpha^{(1)nl}(\omega)$ and $\alpha'^{(2)nl}(\omega)$ vanishes, which guarantees that the exponential function in Eq. (6.16) has the same value of -1 (corresponding to an echo phase $\varphi_{\mathrm{echo}} =$

π) for all offsets if the duration t after the refocusing pulse is set to the offset-independent Hahn-Echo delay

$$\tau^{\text{echo}} = \tau^{(1,2)} + \delta, \tag{6.30}$$

c.f. Eqs. (6.24-6.26) and Eq. (6.29).

In the following, we also consider the *relative auxiliary delay*

$$\frac{\delta}{T^{tot}} = \frac{\delta}{T^{(1)} + T^{(2)}}, \tag{6.31}$$

i.e. the duration of δ relative to the total pulse duration T^{tot}, i.e. (6.31). It is important to note that in the absence of relaxation, diffusion and couplings, the shape and amplitude of the echo is independent of the delay $\tau^{(1,2)}$ between the excitation and the refocusing pulse due to the selected coherence-order pathway. This is a result of the fact that for

$$t' = t - \tau^{(1,2)},$$

c.f. (6.16),

$$s(\omega, t') = \sin\beta^{(1)} \sin^2 \frac{\beta^{(2)}}{2} e^{\mathrm{i}(\omega t' - \alpha^{(1)} + \alpha'^{(2)} - \pi)} \tag{6.32}$$

which is independent of the inter-pulse delay $\tau^{(1,2)}$ because during the delays $\tau^{(1,2)}$ before and after the refocusing pulse the phase factors acquired by $+1$ quantum and -1 quantum coherences cancel each other in these two time periods.[3] As this is the case for each individual offset frequency ω, also the total signal

$$\begin{aligned} s_{tot}(t') &= \int_\omega a(\omega)\ s(t', \omega)\mathrm{d}\omega \\ &= \sin\beta^{(1)}\ \sin^2 \frac{\beta^{(2)}}{2} e^{-\mathrm{i}(\alpha^{(1)} - \alpha'^{(2)} + \pi)} \\ &\qquad \int_\omega a(\omega) e^{\mathrm{i}(\omega(t')} \mathrm{d}\omega \end{aligned} \tag{6.33}$$

produced by the spins of all offsets with distribution $a(\omega)$ is independent of $\tau^{(1,2)}$. In the following we assume that the spin density $a(\omega)$ is constant in order to design pulse sequences that work for arbitrary resonance frequency distributions.

6.2.2 Derivation of transfer function

Figure 6.2 and transformation (6.12) illustrate the selected coherence transfer pathway.

In order to derive the complete transfer function $s(t, \omega)$ we first consider for simplicity the case where $\tau^{(1,2)} = 0$. The initial state is

$$\rho(0) = 2I_z,$$

which is transferred by the first pulse to

$$\rho_1 = 2U_1 I_z U_1^\dagger. \tag{6.34}$$

Note that all propagators U are offset-dependent, for simplicities sake we leave out this sublety in the following. In the zyz convention, the propagator U_1 of the excitation pulse $S^{(1)}$ can be decomposed into three successive Euler rotations:

$$U_1 = U_z^{\alpha^{(1)}} U_y^{\beta^{(1)}} U_z^{\gamma^{(1)}} \tag{6.35}$$

with $U_z^{\alpha^{(1)}} = \exp\{-i\alpha^{(1)} I_z\}$, $U_y^{\beta^{(1)}} = \exp\{-i\beta^{(1)} I_y\}$, and $U_z^{\gamma^{(1)}} = \exp\{-i\gamma^{(1)} I_z\}$, corresponding to a rotation around the z axis about $\gamma^{(1)}$, followed by a rotation around y about $\beta^{(1)}$, followed by a rotation around z about $\alpha^{(1)}$.

Inserting Eq. 6.35 in Eq. 6.34 and using the fact that the initial state $\rho(0)$ is proportional to I_z, which is invariant under the first rotation around z about $\gamma^{(1)}$, we find

$$\begin{aligned} \rho_1 &= 2\ U_z^{\alpha^{(1)}} U_y^{\beta^{(1)}} U_z^{\gamma^{(1)}} I_z\ U_z^{\gamma^{(1)}\dagger} U_y^{\beta^{(1)}\dagger} U_z^{\alpha^{(1)}\dagger} \\ &= 2\ U_z^{\alpha^{(1)}} U_y^{\beta^{(1)}} I_z\ U_y^{\beta^{(1)}\dagger} U_z^{\alpha^{(1)}\dagger} \end{aligned} \tag{6.36}$$

The second rotation around y about $\beta^{(1)}$ transforms I_{1z} to

$$\begin{aligned} U_y^{\beta^{(1)}} I_z\ U_y^{\beta^{(1)}\dagger} &= \cos\beta^{(1)} I_z + \sin\beta^{(1)} I_x \\ &= \cos\beta^{(1)} I_z + \sin\beta^{(1)} \frac{I^+ + I^-}{2}. \end{aligned} \tag{6.37}$$

Inserting Eq. (6.36) in Eq. (6.37) and applying the final rotation around z about $\alpha^{(1)}$ results in

$$\begin{aligned} \rho_1 &= 2\ U_z^{\alpha^{(1)}} \{\cos\beta^{(1)} I_z + \sin\beta^{(1)} \frac{I^+ + I^-}{2}\} U_z^{\alpha^{(1)}\dagger} \\ &= 2\cos\beta^{(1)} I_z + \sin\beta^{(1)} (e^{-i\alpha^{(1)}} I^+ + e^{i\alpha^{(1)}} I^-). \end{aligned}$$

Applying the +1 quantum filter by projecting ρ_1 onto the +1 quantum operator I^+ results in

$$\rho_1^{+1\mathrm{QF}} = f_1\ I^+$$

with the prefactor

$$f_1 = \sin\beta^{(1)} e^{-i\alpha^{(1)}}. \tag{6.38}$$

After the inter-pulse delay $\tau^{(1,2)}$, the density operator is given by

$$U_z^{(\omega\tau^{(1,2)})}\ \rho_1^{+1\mathrm{QF}}\ U_z^{(\omega\tau^{(1,2)})\dagger} = f_1\ e^{-i\omega\tau^{(1,2)}}\ I^+, \tag{6.39}$$

with

$$U_z^{(\omega\tau^{(1,2)})} = e^{-i\omega\tau^{(1,2)}I_z}.$$

The same approach could be applied to the second pulse $S^{(2)}$ as well. However, we prefer the (slightly shorter) direct computation via the rotation matrix.

The transfer function (6.13) can be expressed as

$$\begin{aligned} s(t,\omega) &= \left\langle I^- \middle| U_2 \left\langle I^+ \middle| U_1 I_z U_1^\dagger \right\rangle I^+ U_2^\dagger \right\rangle e^{i\omega t} \\ &= \underbrace{\left\langle I^+ \middle| U_1 I_z U_1^\dagger \right\rangle}_{f_1(\omega)} \underbrace{\left\langle I^- \middle| U_2 I^+ U_2^\dagger \right\rangle}_{f_2(\omega)} e^{i\omega t} \end{aligned} \tag{6.40}$$

(6.39) corresponds to expression $f_1(\omega)$ from (6.40).

$f_2(\omega)$ can be rewritten as

$$\begin{aligned} f_2(\omega) &= \left\langle I^- \middle| U_2 I^+ U_2^\dagger \right\rangle \\ &= \mathrm{Tr}\{I^{-\dagger} U_2 I^+ U_2^\dagger\} \\ &= \mathrm{Tr}\{I^+ U_2 I^+ U_2^\dagger\} \end{aligned} \tag{6.41}$$

In order to simplify notation, we introduce a few abbreviations:

$$\begin{aligned} c &= \cos\left(\frac{\beta}{2}\right) \\ s &= \sin\left(\frac{\beta}{2}\right) \\ p &= \frac{\alpha+\gamma}{2} \\ m &= \frac{\alpha-\gamma}{2}. \end{aligned} \tag{6.42}$$

The expression for the rotation matrix (Eq. 4.21) is given by

$$U = \begin{pmatrix} ce^{-ip} & -se^{-im} \\ se^{im} & ce^{ip} \end{pmatrix}. \tag{6.43}$$

The curly brace in (6.41) is split into two subsequent matrix multiplications:

$$
\begin{aligned}
I^+U_2 &= \begin{pmatrix} 0 & 1 \\ 0 & 0 \end{pmatrix} \begin{pmatrix} ce^{-ip} & -se^{-im} \\ se^{im} & ce^{ip} \end{pmatrix} \\
&= \begin{pmatrix} se^{im} & ce^{ip} \\ 0 & 0 \end{pmatrix}
\end{aligned} \tag{6.44}
$$

$$
\begin{aligned}
I^+U_2^\dagger &= \begin{pmatrix} 0 & 1 \\ 0 & 0 \end{pmatrix} \begin{pmatrix} ce^{ip} & se^{-im} \\ -se^{im} & ce^{-ip} \end{pmatrix} \\
&= \begin{pmatrix} -se^{im} & ce^{-ip} \\ 0 & 0 \end{pmatrix}
\end{aligned} \tag{6.45}
$$

We substitute the results from (6.44) and (6.45) in (6.41) and obtain

$$
\begin{aligned}
f_2(\omega) =& \mathrm{Tr}\left\{ \begin{pmatrix} se^{im} & ce^{ip} \\ 0 & 0 \end{pmatrix} \begin{pmatrix} -se^{im} & ce^{ip} \\ 0 & 0 \end{pmatrix} \right\} \\
=& -s^2e^{2im}
\end{aligned} \tag{6.46}
$$

We resubstitute with the left side of (6.42) and get

$$
f_2(\omega) = -\sin^2 \frac{\beta}{2} e^{\alpha^{(2)} - \gamma^{(2)}} \tag{6.47}
$$

The product of (6.47) and (6.38) equals the transfer function (6.15).

6.2.3 Pre-optimization method

The pre-optimization of cooperative seed sequences is an iterative process and schematically outlined in the following. It is based on the gradient of the PP quality factor Φ_{PP} for the excitation pulse $S^{(1)}$ of duration $T^{(1)}$ and the gradient of a UR quality factor Φ_{UR} for the refocusing pulse $S^{(2)}$ of duration $T^{(2)}$. In each iteration, these two gradients are calculated using the following steps, where steps 1-6 are repeated for all offsets that are considered in the chosen discretization of the desired bandwidth of the echo sequence.

1. Calculate the forward evolution of the initial density operator $\rho(0) = 2I_z$ under the excitation pulse $S^{(1)}$ yielding $\rho(t)$ for $0 \leq t \leq T^{(1)}$ and calculate the projection of $\rho(T^{(1)})$ onto I^+, i.e. apply a +1-quantum filter to $\rho(T^{(1)})$ to yield $\tilde{\rho}(T^{(1)}) = \langle I^+|\rho(T^{(1)})\rangle I^+$.

2. Calculate the forward evolution of the propagator $U^{(2)}(t)$ for the refocusing pulse $S^{(2)}$, starting with $U^{(2)}(T^{(1)}) = \mathbf{1}$ and yielding $U^{(2)}(t)$ for $T^{(1)} \leq t \leq T^{(1)} + T^{(2)}$. In the following, we use the short-hand notation $U^{(2)}_{tot} := U^{(2)}(T^{(1)} + T^{(2)})$ for the total propagator of the refocusing pulse $S^{(2)}$.

3. Determine the ideal rotation axis of the refocusing pulse $S^{(2)}$ based on the density operator $\rho(T^{(1)})$ (obtained in step 1) and the target density matrix ρ_{target}. In the case where the desired offset-independent auxiliary delay δ is zero, the target density matrix is simply given by $\rho_{\text{target}} = I^-$. For $\delta \neq 0$, the target operator is offset-dependent and is defined as $\rho_{\text{target}} = I^- \exp\{-\mathrm{i}\omega\delta\}$. It is straightforward to extract from $\tilde{\rho}(T^{(1)})$ and from ρ_{target} the orientations of the corresponding real magnetization vectors and the phases $\varphi(T^{(1)})$ and φ_{target}. Note that the phases $\varphi(T^{(1)})$ and φ_{target} are only defined up to integer multiples of 2π. This can result in discontinuities of the phases as a function of offset, which can be remedied by a standard phase unwrapping procedure, resulting in smooth functions $\varphi(T^{(1)})$ and φ_{target}. The offset-dependent azimuthal angle φ_{ref} of the rotation axis of the ideal 180° refocusing pulse that maps $\rho(T^{(1)})$ to ρ_{target} in an optimal way is given by $\varphi_{\text{ref}} = (\varphi(T^{(1)}) + \varphi_{\text{target}})/2$. This provides the target propagator $U_{\text{target}} = \exp\{-\mathrm{i}\pi(I_x \cos\varphi_{\text{ref}} + I_y \sin\varphi_{\text{ref}})\}$ for the refocusing pulse, which by construction varies smoothly as a function of offset and hence does not have any sudden changes of the global phase factor, which could cause the algorithm to be trapped in local maxima.

4. Set the co-propagator $\Lambda(T^{(1)} + T^{(2)}) = U_{\text{target}}$ and evolve it backward to yield $\Lambda(t)$ for $T^{(1)} \leq t \leq T^{(1)} + T^{(2)}$.[59,73]

5. The target density operator ρ_{target} is calculated backward under the action of the refocusing pulse $S^{(2)}$ yielding $\lambda(T^{(1)}) := \{U_{tot}^{(2)}\}^\dagger \; \rho_{\text{target}} \; U_{tot}^{(2)}$ and the co-state $\tilde{\lambda}(T^{(1)})$ is obtained by applying a +1-quantum filter to $\lambda(T^{(1)})$.

6. Calculate the backward evolution of the co-state $\tilde{\lambda}(T^{(1)})$ to yield $\tilde{\lambda}(t)$ for $0 \leq t \leq T^{(1)}$.

7. To improve the refocusing pulse $S^{(2)}$, we consider a universal rotation (UR) quality factor

$$\Phi_{UR} = \mathrm{Re}\langle U_{\text{target}} | U_{tot}^{(2)} \rangle$$

for this iteration. Note that Φ_{UR} is sensitive to the global phase of the propagator $U_{tot}^{(2)}$.[59] Based on the first-order gradient of Φ_{UR},[59] the following simple updating scheme is used for the refocusing pulse $S^{(2)}$:

$$u_x(t) \rightarrow u_x'(t) = u_x(t) - \epsilon \overline{\mathrm{Re}\langle \Lambda(t) | i I_x U^{(2)}(t) \rangle}$$

and

$$u_y(t) \rightarrow u_y'(t) = u_y(t) - \epsilon \overline{\mathrm{Re}\langle \Lambda(t) | i I_y U^{(2)}(t) \rangle}$$

for $T^{(1)} < t \leq T^{(1)} + T^{(2)}$, where the overscore indicates the average over all offsets ω of the desired bandwidth of the echo sequence and ϵ is a step size.

8. To improve the excitation pulse $S^{(1)}$, we consider a generalized point-to-point (PP) quality factor

$$\Phi_{\mathrm{PP}} = \mathrm{Re}\langle\tilde{\lambda}(T^{(1)})|\rho(T^{(1)})\rangle$$

for this iteration. Based on the first-order gradient of Φ_{PP},[59] the following simple updating scheme is used for the excitation pulse $S^{(1)}$:

$$u_x(t) \to u'_x(t) = u_x(t) - \epsilon' \, \overline{\mathrm{Re}\langle\tilde{\lambda}(t)|i[I_x, \rho(t)]\rangle}$$

and

$$u_y(t) \to u'_y(t) = u_y(t) - \epsilon' \, \overline{\mathrm{Re}\langle\tilde{\lambda}(t)|i[I_y, \rho(t)]\rangle}$$

for $0 \leq t \leq T^{(1)}$, where the overscore indicates the average over all offsets ω of the desired bandwidth of the echo sequence and ϵ' is a step size.

9. Optimize the step sizes in ϵ and ϵ' in steps 7 and 8 to maximize the actual global quality factor Φ defined in Eq. (4.30) in this iteration.

The optimization starts with a random pulse[59] (or a judiciously chosen pulse) and Steps 1-9 are repeated iteratively until a predefined stop criterion is reached, such as a desired quality factor, a chosen maximum number of iterations or a maximally allowed duration of the optimization.

This pre-optimization algorithm was implemented using the IPOPT package,[83] which requires a function that provides an expression for a gradient and a function that provides a figure of merit. In the pre-optimization, the gradients for the excitation and for the refocusing part of the echo sequence are obtained in steps 6 and 7, respectively. The quality factor Φ (c.f. Eq. (4.30) was calculated as the figure of merit for IPOPT.

Note that this approach should only be used as a pre-optimization of COOP echo sequences because the used gradients of Φ_{PP} for the excitation pulse $S^{(1)}$ and of Φ_{UR} for the refocusing pulse $S^{(2)}$ are not the actual gradients of the echo quality factor Φ to be optimized. Therefore, the pre-optimized sequences should be subject to a final optimization based on Φ (c.f. Eq. (4.30) and its gradient, c.f. Eq. (4.31). However, even without such a final optimization step, on average the results obtained by this pre-optimization algorithm are significantly better than the results obtained if the optimization is directly performed based on Φ and its gradient. Despite the fact that in the simple approach used here for the pre-optimization, where we effectively separate the gradients for $S^{(1)}$ and $S^{(2)}$, it is important to note that the outlined pre-optimization algorithm is cooperative and *not* equivalent to the individual optimization of a PP excitation pulse and of a UR refocusing pulse: The costate $\tilde{\lambda}(t)$ used in step 8 to calculate the gradient for the excitation pulse $S^{(1)}$ depends on the refocusing pulse $S^{(2)}$ (c.f. steps 5 and 6). Conversely, the costate $\Lambda(t)$ used in step 7 to calculated the gradient for the refocusing pulse $S^{(2)}$ also depends on the effect of the excitation pulse $S^{(1)}$ (c.f. steps 1, 3, and 4).

6.2.4 Families of Hahn echoes

In order to compare the performance of optimized COOP echo sequences with conventional approaches, it is helpful to define the following families of echo sequences. For all families of echo sequences considered below, the Euler angle $\beta^{(1)}(\omega)$ of the excitation pulse $S^{(1)}$ is assumed to approach the ideal value of $\pi/2$ and the Euler angle $\beta^{(2)}(\omega)$ of the refocusing pulse $S^{(2)}$ is assumed to approach the ideal value of π according to conditions (6.27-6.28). Furthermore, it is assumed that the general echo condition (6.29) is fulfilled. However, the different families of echo sequences impose different constraints on the Euler angles $\gamma^{(1)}(\omega)$, $\alpha^{(1)}(\omega)$ and $\alpha'^{(2)}(\omega)$ (c.f. Eq. 6.14) and the echo family with the largest number of degrees of freedom is expected to provide the best echo performance in the desired range of offset frequencies (c.f. Tab. 6.2).

Ideal echo sequence based on hard pulses

The idealized echo sequence

$$(\pi/2)_y \text{ - } \tau^{(1,2)} \text{ - } (\pi)_x \text{ - } \tau^{\text{echo}}$$

consists of infinitely strong delta pulses of negligible durations and $\tau^{\text{echo}} = \tau^{(1,2)}$. In this limiting case, the Euler angles are offset-independent and given by $\beta^{(1)}(\omega) = \pi/2$, $\beta^{(2)}(\omega) = \pi$ and $\gamma^{(1)}(\omega) = \alpha^{(1)}(\omega) = \alpha'^{(2)}(\omega) = 0$ (c.f. Fig. 6.4F and sequence F in Table 6.2).

Echo sequence based on rectangular pulses

The most widely used conventional echo experiments consist of rectangular pulses. It is well known that during a rectangular excitation pulse of duration $T^{(1)}$ offset evolution takes place during an effective duration of $2T^{(1)}/\pi$.[144] For example, for a pulse amplitude of 10 kHz and a corresponding duration $T_{90} = 25$ μs of the rectangular 90° pulse, this results in a non-zero auxiliary echo delay of $\delta = 2T_{90}/\pi = 15.9$ μs.

Echo sequence based on universal rotation (UR) pulses

A naive approach to realize the ideal echo sequence would be to implement both the excitation pulse and the refocusing pulse as a universal rotation (UR) pulse[73] with finite durations $T^{(1)}$ and $T^{(2)}$, respectively:

$$\text{UR}(\pi/2)_y \text{ - } \tau^{(1,2)} \text{ - } \text{UR}(\pi)_x \text{ - } \tau^{\text{echo}}.$$

The UR pulses approximate all the Euler angles of the ideal echo sequence based on hard pulses for a desired range of offset frequencies, i.e. $\gamma^{(1)}(\omega) = \alpha^{(1)}(\omega) = \alpha'^{(2)}(\omega) = 0$ and $\tau^{\text{echo}} = \tau^{(1,2)}$ (c.f. Fig. 6.4E and sequence E in Table 6.2).

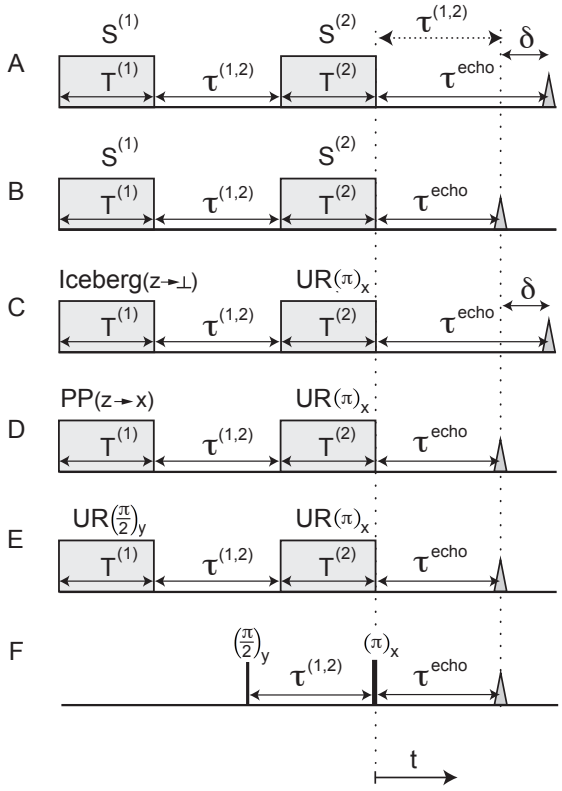

Figure 6.4: Pictorial representation of the different families of Hahn echo sequences discussed in the text. A, B: s^2 $COOP_\delta$ echo sequence based on cooperative excitation and refocusing pulses (denoted $S^{(1)}$ and $S^{(2)}$, respectively) with auxiliary delay $\delta \neq 0$ (A) and $\delta = 0$ (B). C-E: Echo sequences based on universal rotation $UR(\pi)_y$ [73] refocusing pulses. In sequence C, "Iceberg($z \rightarrow \perp$)" denotes a so-called ICEBERG excitation pulse [8] which transforms initial z-magnetization to transverse magnetization with a linear phase as a function of offset. In sequence D, "PP($z \rightarrow x$)" represents a point-to-point (PP) [62] excitation pulse that transforms initial z-magnetization to x-magnetization (i.e. transverse magnetization with an offset-independent phase of 0°). In sequence E, $S^{(1)}$ is a UR $(\pi/2)_y$ pulse. Sequence F depicts the ideal Hahn echo sequence consisting of $(\pi/2)_y$ and $(\pi)_y$ hard pulses of negligible duration. The delay between the end of the excitation pulse and the beginning of the refocusing pulse is denoted $\tau^{(1,2)}$. Sequences (A)-(F) are drawn such that the ends of the refocusing pulses are aligned, as indicated by the first vertical dotted line, which marks the origin of the evolution time t after the last pulse. The second vertical dotted line is shifted relative to the first vertical dotted line by $\tau^{(1,2)}$ to guide the eye. The echo has its maximum amplitude at $t = \tau^{echo} = \tau^{(1,2)} + \delta$ with $\delta \neq 0$ for sequences A and C.

Table 6.2: Echo delay τ^{echo} and degrees of freedom of the Euler angles characterizing the excitation pulse $S^{(1)}$ and the refocusing pulse $S^{(2)}$ for different Hahn echo sequence families

	echo sequence family	τ^{echo}	$\gamma^{(1)}$	$\alpha^{(1)}$	$\alpha'^{(2)}$
A	s^2-COOP$_\delta$: $S^{(1)}$ - $\tau^{(1,2)}$ - $S^{(2)}$ - τ^{echo}	$\tau^{(1,2)} + \tau_\alpha^{(1)} + \tau_\alpha'^{(2)}$	•	$\bullet^a$	$\bullet^a$
B	s^2-COOP$_0$: $S^{(1)}$ - $\tau^{(1,2)}$ - $S^{(2)}$ - τ^{echo}	$\tau^{(1,2)}$	•	•	$\alpha^{(1)}$
C	Iceberg($z \to \perp$) - $\tau^{(1,2)}$ - UR$(\pi)_x$ - τ^{echo}	$\tau^{(1,2)} + \tau_\alpha^{(1)}$	•	$\bullet^b$	0
D	PP($z \to x$) - $\tau^{(1,2)}$ - UR$(\pi)_x$ - τ^{echo}	$\tau^{(1,2)}$	•	0	0
E	UR$(\pi/2)_y$ - $\tau^{(1,2)}$ - UR$(\pi)_x$ - τ^{echo}	$\tau^{(1,2)}$	0	0	0
F	$(\pi/2)_y$ - $\tau^{(1,2)}$ - $(\pi)_x$ - τ^{echo}	$\tau^{(1,2)}$	0	0	0

$S^{(1)}$	excitation pulse,
$\tau^{(1,2)}$	delay between the end of the excitation pulse and beginning of the refocusing pulse
$S^{(2)}$	refocusing pulse,
τ^{echo}	delay between the end of the refocusing pulse and the echo signal, c.f. Fig. 6.4
s^2-COOP$_\delta$	represents single-scan cooperative Hahn echo sequences with $\tau^{echo} = \tau^{(1,2)} + \delta$, where $\delta = \tau_\alpha'^{(2)} - \tau_{\alpha'}^{(1)}$ for sequence A (c.f. Eq. 6.24) and $\delta = 0$ for sequence B (c.f. Eq. 6.26) and 6.31, respectively.

The effective delays $\tau_\alpha^{(1)}$, $\tau_\gamma^{(2)}$, and $\tau_\alpha^{(2)}$ are defined as $\tau_\alpha^{(k)} = \alpha^{(k)\text{lin}}/\omega = R_\alpha^{(k)} T^{(k)}$ and $\tau_\gamma^{(k)} = \gamma^{(k)\text{lin}}/\omega = R_\gamma^{(k)} T^{(k)}$ for $k \in \{1,\ 2\}$, c.f. Eq. (6.22, 6.23).
The ideal Euler angles $\beta^{(k)}$ for the Hahn echo sequences considered here (where the delay $\tau^{(1,2)}$ between the pulses can be arbitrarily varied) are $\beta^{(1)} = \pi/2$ and $\beta^{(2)} = \pi$. Note that for an Euler angle $\beta = \pi$ only the difference $\gamma - \alpha$
is defined, i.e. the individual Euler angles γ and α are arbitrary.[148] Therefore, in the last column of the table only
the difference angle $\alpha'^{(2)} = \alpha^{(2)} - \gamma^{(2)}$ (c.f. Fig. 6.4 C and Eq. 6.14) is considered for the refocusing pulse (assuming $\beta^{(2)} \approx \pi$).

- • the corresponding parameters are not fixed, i.e. they constitute important degrees of freedom in pulse optimizations.
- $\bullet^a$ For sequence A, the corresponding parameters are arbitrary, but their nonlinear components are related through the condition $\alpha^{(1)\text{nl}} + (\gamma^{(2)\text{nl}} - \alpha^{(2)\text{nl}}) \stackrel{!}{=} 0$, c.f. Eq. 6.18.
- $\bullet^b$ For sequence C, the nonlinear part of the Euler angle $\alpha^{(1)}$ vanishes,i.e. $\alpha^{(1)\text{nl}} \stackrel{!}{=} 0$ (c.f. Eq. 6.18).
- 0 the corresponding parameter should have a fixed value of zero.

For sequence B, the difference angle $\alpha'^{(2)} = \alpha^{(2)} - \gamma^{(2)}$ must be identical to $\alpha^{(1)}$.
Case F corresponds to the case of ideal $(\pi/2)_y$ and $(\pi)_x$ hard pulses of negligible duration.

Echo sequence based on point-to-point (PP) excitation and UR refocusing pulses without auxiliary delay δ

As discussed above, the Euler angle $\gamma^{(1)}(\omega)$ is irrelevant for the Hahn echo sequence starting with initial z-magnetization (c.f. Fig. 6.3B). Hence, the excitation pulse can be implemented by a point-to-point (PP) pulse[62] with arbitrary $\gamma^{(1)}(\omega)$ that is designed to bring initial z-magnetization to the x axis for a desired range of offset frequencies:

$$\mathrm{PP}(z \rightarrow x) \text{ - } \tau^{(1,2)} \text{ - } \mathrm{UR}(\pi)_x \text{ - } \tau^{\mathrm{echo}}.$$

The remaining conditions $\alpha^{(1)}(\omega) = \alpha'^{(2)}(\omega) = 0$ imply both $\delta = 0$ (c.f. Eqs. 6.22, 6.23 and 6.25) and $\epsilon(\omega) = 0$ (c.f. Eq. 6.26) and hence $\tau^{\mathrm{echo}} = \tau^{(1,2)}$ (c.f. Eq. 6.24) as in the ideal echo sequence, (c.f. Fig. 6.4D and sequence D in Table 6.2).

Echo sequence based on Iceberg excitation and UR refocusing pulses with auxiliary delay $\delta \neq 0$

The condition $\alpha^{(1)}(\omega) = 0$ can be relaxed by using PP excitation pulses that are not restricted to create only x-magnetization (i.e. transverse magnetization with an offset-independent initial phase of zero). Instead, so-called Iceberg pulses[8] can be used that transform initial z-magnetization to transverse magnetization with a non-zero but *linear* phase dependence as a function of offset:

$$\mathrm{Iceberg}(z \rightarrow \perp) \text{ - } \tau^{(1,2)} \text{ - } \mathrm{UR}(\pi)_x \text{ - } \tau^{\mathrm{echo}}.$$

In this family of Hahn echo sequences, the condition $\alpha^{(1)}(\omega) = 0$ is relaxed to the condition $\alpha^{(1)\mathrm{nl}}(\omega) = 0$, i.e. only the non-linear term of the Euler angle $\alpha^{(1)}(\omega)$ has to vanish. The use of a UR refocusing pulse still requires $\alpha'^{(2)}(\omega) = 0$. The general echo condition $\epsilon(\omega) = 0$ (Eq. 6.13) still needs to be fulfilled but according to Eq. (6.22) the non-zero linear term $\alpha^{(1)\mathrm{lin}}(\omega)$ implies a non-zero effective delay $\tau_\alpha^{(1)}$ and hence a non-zero auxiliary delay $\delta \neq 0$ (c.f. Eq. 6.25). Therefore, according to Eq. (6.24), the echo delay $\tau^{\mathrm{echo}} = \tau^{(1,2)} + \delta$ is not identical to the inter-pulse delay $\tau^{(12)}$ (see Fig. 6.4C and sequence C in Table 6.2).

Note that for offsets that are small compared to the rf amplitude, the commonly used standard echo sequence based on *rectangular* excitation and refocusing pulses is an example of this class of Hahn echo sequences, because a rectangular 180° pulse approximates a UR pulse and a rectangular 90° pulse creates transverse magnetization with an approximately *linear* phase dependence that is given by $2T_{90}\omega/\pi$, c.f. section 6.2.4.[144]

$\mathbf{s^2}$ $\mathbf{COOP_0}$ echo sequence based on cooperative excitation and refocusing pulses without auxiliary delay ($\delta = 0$)

The conditions for the angle $\alpha^{(1)}(\omega)$ and the difference angle $\alpha'^{(2)}(\omega)$ can be further relaxed if the excitation and refocusing pulses are concurrently optimized such that individual pulse errors can be mutually cancelled. The family of cooperative echo sequences

with a vanishing auxiliary delay $\delta = 0$ (corresponding to $\tau^{\text{echo}} = \tau^{(1,2)}$) is denoted s^2 $COOP_0$ (c.f. Fig. 6.4B and sequence B in Table 6.2). Based on Eq. (6.19), only the condition

$$\alpha^{(1)}(\omega) - \alpha'^{(2)}(\omega) \stackrel{!}{=} 0. \tag{6.48}$$

has to be fulfilled. Hence, the linear or non-linear components of the individual Euler angles are not restricted as long as they mutually cancel, i.e. if

$$\alpha'^{(2)\text{lin}}(\omega) \stackrel{!}{=} \alpha^{(1)\text{lin}}(\omega) \tag{6.49}$$

and

$$\alpha'^{(2)\text{nl}}(\omega) \stackrel{!}{=} \alpha^{(1)\text{nl}}(\omega). \tag{6.50}$$

Broadband s^2 $COOP_0$ echo sequences can be optimized based on the filter-based global quality factor Φ described in section 4.4.3. Alternatively, it is possible to directly optimize for conditions (6.27, 6.28 and 6.48).

s^2 $COOP_\delta$ echo sequence based on cooperative excitation and refocusing pulses with auxiliary delay $\delta \neq 0$

In general, it is not necessary to require $\tau^{\text{echo}} = \tau^{(1,2)}$. In this case, condition (6.49) for the linear terms $\alpha^{(1)\text{lin}}(\omega)$ and $\alpha'^{(2)\text{lin}}(\omega)$ can also be dropped. This finally leaves us only with condition (6.50), which requires the sum of the non-linear terms $\alpha'^{(2)\text{nl}}(\omega)$ and $\alpha^{(1)\text{nl}}(\omega)$ to be zero. The echo delay is given by $\tau^{\text{echo}} = \tau^{(1,2)} + \delta$ with the auxiliary delay $\delta = -\tau_\alpha^{(1)} + \tau_{\alpha'}^{(2)}$, c.f. Fig. 6.4 A and sequence A in Table 6.2. Broadband s^2 $COOP_\delta$ echo sequences can also be optimized based on the filter-based global quality factor Φ described in section 4.4.3. However, in this case the propagator $U^{(2)}$ for the refocusing pulse $S^{(2)}$ is replaced by the $U'^{(2)} = \exp\{-i\omega\delta I_z\}U^{(2)}$ which represents the overall propagator of $S^{(2)}$ followed by the auxiliary delay δ. Alternatively, it is also possible to directly optimize the conditions (6.27 - 6.29) for the Euler angles.

6.2.5 Effective evolution time representation of Hahn echo sequences

The *offset-dependent* evolution periods $\tau_\phi^{(k)}(\omega)$ introduced here can be regarded as a generalization of *offset-independent* evolution periods that were introduced to approximate the effect of a pulse for a limited range of offsets by a first constant delay, an ideal pulse, and a second constant delay.[149,150]

A number of different (but equivalent) graphical representations of these offset-dependent effective evolution periods $\tau_\phi^{(k)}(\omega)$ are possible. In the following, we focus on four specific representations, that are helpful in a graphical and intuitive analysis of Hahn echo sequences, see Figs. 6.6 and 6.5.

Each individual (composite or shaped) pulse is represented by a black rectangle (c.f. Fig. 6.6). The upper and lower edges of each rectangle correspond to the limits of the

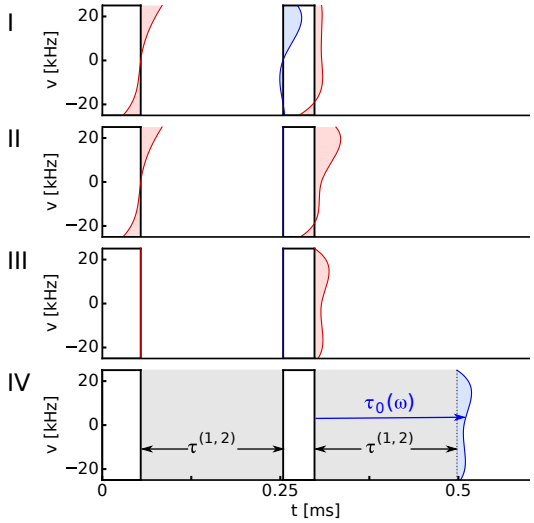

Figure 6.5: Graphical representation of the effective evolution periods for a Hahn Echo sequence. Panels I to IV show plot types introduced in section 6.2.5.

considered frequency range. Left and right edges mark the beginning and the end of the RF pulse. Note that positive values of effective evolution periods $\tau_\phi^{(k)}(\omega)$ are plotted from the corresponding edge of the pulse towards the pulse center, whereas negative effective evolution periods are plotted in the opposite direction (c.f. Fig. 6.6). Hence, positive values of $\tau_\gamma^{(k)}(\omega)$ are plotted towards the right (relative to the leading edge of pulse k) and negative values of $\tau_\gamma^{(k)}(\omega)$ are plotted towards the left. Conversely, positive values of $\tau_\alpha^{(k)}(\omega)$ are plotted towards the left (relative to the trailing edge of pulse k) and negative values of $\tau_\alpha^{(k)}(\omega)$ are plotted towards the right. Blue and red curves correspond to $\tau_\gamma^{(k)}$ and $\tau_\alpha^{(k)}$ respectively. Here and in the following figures, we use the convention that for blue (red) curves the positive time axis points to the right (left). Fig. 6.5 shows a schematic representation of an echo sequence (with crusher gradients or EXORCYCLE) consisting of two pulses. Here, $\tau_\gamma^{(1)}$ is not shown because the initial state I_z is invariant under z rotations. Based on the Euler angles $\alpha^{(1)}$, $\gamma^{(2)}$, $\alpha^{(2)}$ and the derived angles $\alpha'^{(2)}$ (Eq. 6.14 and Fig. 6.3 C) and $\alpha''^{(2)}$ (Eq. 6.52 and Fig. 6.3 D), effective evolution periods $\tau_\alpha^{(1)}$, $\tau_\gamma^{(2)}$, $\tau_\alpha^{(2)}$, $\tau_\alpha'^{(2)}$, and $\tau_\alpha''^{(2)}$ are defined below and are used in the following graphical representations of echo sequences:

Type I

Type I plots separately depict $\tau_\alpha^{(1)}(\omega)$ at the end of the excitation pulse, $\tau_\gamma^{(2)}(\omega)$ at the beginning of the refocusing pulse and $\tau_\alpha^{(2)}(\omega)$ at the end of the refocusing pulse.

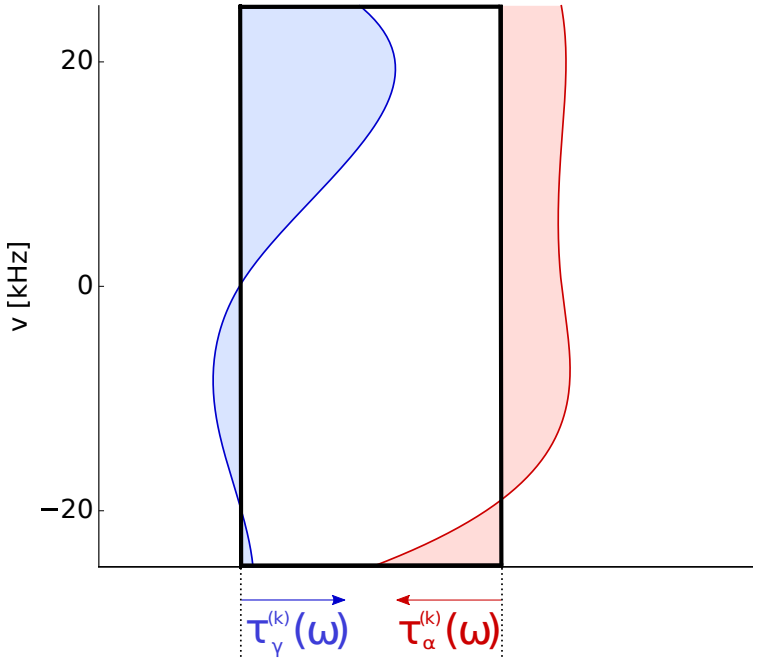

Figure 6.6: Representation of the plotting direction of effective evolution times for a single pulse (black rectangle). τ_α is plotted toward the left with respect to the end of a pulse, τ_γ is plotted to the right with respect to the leading edge. Here and in the following figures, we use the convention that for blue (red) curves the positive time axis points to the right (left).

Type II

We define the effective evolution periods $\tau_\alpha'^{(1)}$, $\tau_\gamma'^{(2)}$, and $\tau_\alpha'^{(2)}$ as

$$\begin{aligned}\tau_\alpha'^{(1)} &= \tau_\alpha^{(1)} \\ \tau_\gamma'^{(2)} &= 0 \\ \tau_\alpha'^{(2)} &= \tau_\alpha^{(2)} - \tau_\gamma^{(2)}.\end{aligned}$$

In essence, compared to type I, for each offset the period $\tau_\gamma^{(2)}$ is moved from the leading edge of the refocusing pulse to the trailing edge and merged (with inverted sign) with $\tau_\alpha^{(2)}$ to yield $\tau_\alpha'^{(2)}$. Note that the echo condition Eq. (6.48) and Eqs. (6.27- 6.29) imply the condition

$$\tau_\alpha'^{(1)}(\omega) \stackrel{!}{=} \tau_\alpha'^{(2)}(\omega) + \delta \tag{6.51}$$

for all offsets ω in the desired bandwidth of the COOP echo sequence.

Type III

In the type III representation also the period $\tau_\alpha'^{(1)} = \tau_\alpha^{(1)}$ is moved from the trailing edge of the excitation pulse to the trailing edge of the refocusing pulse and merged (with inverted sign) with $\tau_\alpha'^{(2)}$ to yield $\tau_\alpha''^{(2)}$:

$$\begin{aligned}\tau_\alpha''^{(1)} &= 0\\ \tau_\gamma''^{(2)} &= 0\\ \tau_\alpha''^{(2)} &= \tau_\alpha'^{(2)} - \tau_\alpha^{(1)}.\end{aligned}$$

Correspondingly, the Euler angle $\alpha''^{(2)}$ is defined as

$$\begin{aligned}\alpha''^{(2)} &= \alpha'^{(2)} - \alpha^{(1)}\\ &= \alpha^{(2)} - (\alpha^{(1)} + \gamma^{(2)}),\end{aligned} \tag{6.52}$$

c.f. Fig. 6.3 D. This is possible because the effects of $\tau_\alpha^{(1)}$ and $\tau^{(1,2)}$ commute and hence, $\tau_\alpha^{(1)}$ can be moved from the trailing edge of the excitation pulse to the leading edge of the refocusing pulse and finally merged (with inverted sign) with $\tau_\alpha'^{(2)}$ at the trailing edge of the refocusing pulse to yield $\tau_\alpha''^{(2)}$.

Type IV

Finally, in the type IV representation, we visualize the overall offset-dependent delay

$$\tau_0(\omega) = \tau^{(1,2)} - \tau_\alpha''^{(2)}(\omega) \tag{6.53}$$

after the end of the refocusing pulse, for which all transverse magnetization vectors have the identical phase

$$\phi_0 = \alpha_0^{(2)} - (\alpha_0^{(1)} + \gamma_0^{(2)}) + \pi, \tag{6.54}$$

which can be absorbed in the receiver phase $\varphi_{\mathrm{rec}} = \phi_0$ of the echo experiment. Note that $\phi_n(\omega) = \phi_0(\omega) + n2\pi$ is equivalent, resulting in multiple equivalent phase fronts at

$$\tau_n(\omega) = \tau_0(\omega) + \frac{n2\pi}{\omega}. \tag{6.55}$$

Eq. (6.53) is best rationalized by first considering the effect of an ideal echo sequence with $\tau_\alpha''^{(2)}(\omega) = 0$ for all offsets. In this case, the transverse magnetization vectors of all offset frequencies would have the same phase at $t = \tau^{(1,2)}$ after the end of the refocusing pulse. If $\tau_\alpha''^{(2)}(\omega) > 0$, the effective evolution period $\tau_0(\omega)$ needs to be shorter than $\tau^{(1,2)}$ because part of the necessary evolution for refocusing effectively takes place during the refocusing pulse. If $\tau_\alpha''^{(2)}(\omega) < 0$, the effective evolution period $\tau_0(\omega)$ needs

to be longer than $\tau^{(1,2)}$. In the following, we refer to the function $\tau_0(\omega)$ as the *phase front*. If this phase front is a vertical line in type IV representation, i.e. if $\tau_0(\omega)$ is offset-independent, the signal components coherently add up for all offset frequencies, resulting in a maximum echo signal. Note that a given deviation Δ of the phase front from a vertical line has no effect on the magnetization phase for the on-resonance case ($\omega = 0$), whereas the resulting phase error $\varphi_\Delta = \omega\Delta$ increases linearly with increasing offset ω.

Although the display types III and IV clearly illustrate the overall phase front, display type II is also very helpful to see how well the offset-dependent variations of the effective evolution periods $\tau_\alpha^{(1)}$ and $\tau_\alpha^{\prime(2)}$ associated with the excitation and inversion pulses match (up to an offset-independent auxiliary delay δ), c.f. Eq. (6.51).

6.2.6 Application to coupled spin systems

Here we describe the application of of s^2 COOP Hahn echo sequences to systems with couplings. The specific contributions to the Hamiltonian $\mathcal{H}$ originally introduced in section 4.1.3.2 are briefly reviewed in the context of their application and efficient extensions of the procedures for pulse optimization laid out in section 4.4.3 are presented.

Hitherto we treated ensembles of uncoupled spins. These ensembles are composed of spins with different resonance frequencies what did not experience magnetic fields generated by other spins in any form. In actual spin systems, these interactions occur in different forms and strengths. In liquid state NMR, the two most common interactions are weak and strong coupling due to Fermi contact interaction.[2,3] However, these are usually in the order of a few Hz, i.e. evolution occurs on a timescale of tens or hundreds of milliseconds and their evolution during the pulse can usually be ignored. In solid state NMR or in EPR, dipolar (or hyperfine) coupling interactions occur; these are strong enough that their contributions to the spin Hamiltonion $\mathcal{H}$ have to be considered.

We confine ourselves to two-spin 1/2 systems here, which consis of either heteronuclear spins or an electron and a nuclear spin. Only one of the nuclear or the electron spin is exposed to irradiation. In the following, we distinguish three cases:

1. the coupling hamiltonian contains only secular terms I_zS_z. For NMR, this corresponds to the weak coupling case
2. the coupling hamiltonian contains secular (I_zS_Z) and pseudo-secular terms (I_xS_z or I_yS_z)
3. the coupling hamiltonian contains secular and pseudo-secular terms (case 2) and the resonance frequency of the I-spin is non-zero

In case 1 the coupling Hamiltonian $\mathcal{H}_{\text{coupl}}$ is simplified to

$$\mathcal{H}_{\text{coupl}} = 2\pi J \cdot I_{1z}I_{2z} = J \cdot I_zS_z \tag{6.56}$$

This description is accurate when the difference in resonance frequences ω^{res} significantly exceeds the strength of the coupling constant J.

Case 2 is relevant to EPR applications with Hyperfine interactions, where the isotropic parts can be neglected.

In case 2 $\mathcal{H}_{\text{coupl}}$ has secular contributions $\mathcal{H}_{\text{secular}}$, which correspond to a sum of the weak coupling hamiltonian (Eq. 6.56) and pseudo-secular terms

$$\mathcal{H}_{\text{pseudosecular}} = 2\pi J^{x}_{\text{pseudosecular}} I_x S_z + 2\pi J^{y}_{\text{pseudosecular}} I_y S_z. \tag{6.57}$$

The overall coupling hamiltonian is given by

$$\mathcal{H}_{\text{coupling}} = 2\pi J \cdot I_z S_z + 2\pi J^{x}_{\text{pseudosecular}} I_x S_z + 2\pi J^{y}_{\text{pseudosecular}} I_y S_z. \tag{6.58}$$

Case 3 corresponds to case 2 with additional chemical shift evolution on the I-spin, which is relevant in case the magnitude of the hyperfine interaction between nucleus and electron spin does not exceed the resonance frequency of the nucleus vastly. The coupling Hamiltonian corresponds to the coupling Hamiltonian in (Eq. 6.58). However, in the overall Hamiltonian, the offset term has to be considered for both the I and the S spin.

In section 4.1.3 we briefly reviewed treatment of the dynamics of a spin system:

- controls are described by S_x and S_y
- offset evolution is expressed as S_z
- The initial state is given by $S_z(+I_z)$
- The target state corresponds to S^+ for Hahn echoes
- the propagator U is given by $U = \exp\{-i\mathcal{H}t\}$

However, the cases considered here can be treated in a simpler fashion. For case 1, the Hamiltonian can be rewritten as

$$\begin{aligned}
\mathcal{H} &= \begin{pmatrix} \mathcal{H}^{2x2}_{\text{uncoupled}} & 0 \\ 0 & \mathcal{H}^{2x2}_{\text{uncoupled}} \end{pmatrix} + \mathcal{H}_{\text{coupl}} \\
&= \begin{pmatrix} \mathcal{H}^{2x2}_{\text{uncoupled}} + \pi J S^{2x2}_z & 0 \\ 0 & \mathcal{H}^{2x2}_{\text{uncoupled}} - \pi J S^{2x2}_z \end{pmatrix} \\
&= \begin{pmatrix} \mathcal{H}^{2x2}_{\text{rf/mw}} + (\omega_z + \pi J) S^{2x2}_z & 0 \\ 0 & \mathcal{H}^{2x2}_{\text{rf/mw}} + (\omega_z - \pi J) S^{2x2}_z \end{pmatrix}.
\end{aligned} \tag{6.59}$$

The corresponding propagator U_{coupl} can be expressed as

$$U_{\text{coupl}}(\omega) = \begin{pmatrix} U(\omega + \pi J)^{2x2} & 0 \\ 0 & U(\omega - \pi J)^{2x2} \end{pmatrix} \tag{6.60}$$

A set of broadband controls $u_i(t)$ is required that covers uncoupled spins with resonance frequencies $\omega + 2\pi J$ and $\omega - 2\pi J$ simultaneously. That sequence carries out

the same transformation for coupled spins with a coupling constant J at a resonance frequency ω.

Therefore, in case 1, it is not necessary to double the matrix size (and thus computational costs by a factor 8). If the strength of the coupling is large enough that it has to be considered in the optimization procedure, it is sufficient to increase the bandwidth from $\Delta\omega$ to $\Delta\omega+2\pi J$. In case that pseudosecular terms cannot be neglected (case 2), we show in section 7.1.9 that Hahn echo sequences that are applicable in the weak coupling regime tolerate pseudosecular terms in the Hamiltonian as well.

6.3 $\frac{\pi}{2} - \pi - \frac{\pi}{2}$ sequences

6.3.1 Euler angle analysis of $\frac{\pi}{2} - \pi - \frac{\pi}{2}$ sequences

In section 6.2.1, a detailed analysis of Hahn echo sequences in terms of Euler angles was conducted. A similar approach is chosen for $\frac{\pi}{2} - \pi - \frac{\pi}{2}$ sequences, which correspond to Hahn echo sequences followed by a $\frac{\pi}{2}$ pulse. The ideal transfer pathways are identical to Hahn echoes complemented by a third pulse.

The third pulse, henceforth also referred to $S^{(3)}$ pulse, has a flip angle of 90° and a duration $T^{(3)}$. The total pulse duration T^{tot} is given as

$$T^{tot} = T^{(1)} + T^{(2)} + T^{(3)}. \tag{6.61}$$

At the end of the $S^{(3)}$ pulse, a Zero Quantum Filter (ZQF) is appended (c.f. Fig. 6.7). Experimentally, this is implemented by gradients or by combining the EXORCYCLE with a CYCLOPS phasecycle.

The delay between the end of the second pulse $S^{(2)}$ and the third pulse $S^{(3)}$ is referred to as $\tau^{(2,3)}$. In section 6.2.1 we introduced a transfer function by representing the transformation of each individual pulse $S^{(k)}$ by its corresponding Euler angles γ_z, β_y and α_z. Here we use a similar approach (c.f. Fig. 6.8). The modified transfer is shown in representation (6.62).

$$\begin{array}{lllllll} 2I_z & \xrightarrow{\gamma_z^{(1)}} & \xrightarrow{\beta_y^{(1)}} & \xrightarrow{\alpha_z^{(1)}} & \xrightarrow{\mathbf{+1QF}} & \xrightarrow{(\omega\tau^{(1,2)})_z} & \\ & \xrightarrow{\gamma_z^{(2)}} & \xrightarrow{\beta_y^{(2)}} & \xrightarrow{\alpha_z^{(2)}} & \xrightarrow{\mathbf{-1QF}} & \xrightarrow{(\omega\tau^{(2,3)})_z} & \\ & \xrightarrow{\gamma_z^{(3)}} & \xrightarrow{\beta_y^{(3)}} & \xrightarrow{\alpha_z^{(3)}} & \xrightarrow{\mathbf{0QF}} & sI_z & \end{array} \tag{6.62}$$

The corresponding transfer function s_{3P} is given by

$$s_{3P}(\omega) = -\sin\beta^{(3)} e^{\mathrm{i}\gamma^{(3)}} s_{\text{Hahn echo}}(\tau^{(2,3)})(\omega) \tag{6.63}$$

Note that the transfer function is time independent. The right-hand side of (6.15) can be inserted to eliminate $s_{\text{Hahn echo}}$ from (6.63):

Table 6.3: CYCLOPS phase cycle employed in the $\frac{\pi}{2} - \pi - \frac{\pi}{2}$ experiment and joint phase cycle

step	phase of $S^{(3)}$ [deg]	receiverphase [deg]
1	0	0
2	90	90
3	180	180
4	270	270

step	phase of $S^{(2)}$ [deg]	phase of $S^{(3)}$ [deg]	receiverphase [deg]
1	0	0	0
2	90	0	180
3	180	0	0
4	270	0	180
5	0	90	90
6	90	90	270
7	180	90	0
8	270	90	270
9	0	180	180
10	90	180	0
11	180	180	180
12	270	180	0
13	0	270	270
14	90	270	90
15	180	270	270
16	270	270	90

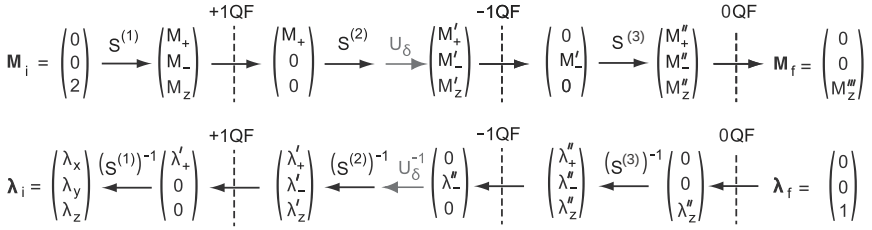

Figure 6.7: Schematic representation of the forward evolution of the magnetization vector M and the backward evolution of the co-state vector λ on which the GRAPE algorithm is based[7,59] for the case of a vanishing inter-pulse delays $\tau^{(1,2)}$ and $\tau^{(2,3)}$. Here, the components of the vectors are the expectation values $\langle I^+\rangle$, $\langle I^-\rangle$, and $\langle I_z\rangle$.[147] $S^{(1)}$, $S^{(2)}$ and $S^{(3)}$ represent the propagators of the three pulses to be optimized and $U_\delta = \exp(-\mathrm{i}\delta I_z)$ corresponds to the propagator of the auxiliary delay δ. (A dark grey font was used for the propagator U_δ to indicated that this step can be omitted in the optimization of the COOP$_0$ echo sequences of Fig. 1B. The dashed lines labeled "+1QF", "−1QF" and "0QF" represent +1, −1 and 0 quantum filters, respectively.

$$s_{3P} = \sin\beta^{(1)} \sin^2 \frac{\beta^{(2)}}{2} \sin\beta^{(3)} e^{-\mathrm{i}(\omega(\tau^{(1,2)}-\tau^{(2,3)})+\alpha^{(1)}-\alpha'^{(2)}+\gamma^{(3)}}, \tag{6.64}$$

In contrast to Hahn echoes, the transfer function presented for the $\frac{\pi}{2}-\pi-\frac{\pi}{2}$ experiment does not correspond to a directly observable signal in NMR. An additional pulse is required to transform 0-quantum coherence into detectable +1-quantum coherence.

When filters are used, it is possible to employ the same transformations for Euler angles as for Hahn echoes (c.f. Fig. 6.8). 0-quantum coherence is invariant under z-rotations. Therefore the final rotation about $\gamma_z^{(3)}$ can be ignored. This is indicated schematically in Fig. 6.8 A by a darker box for $\alpha_z^{(3)}$.

Using coherence transfer pathway selection, it is possible to condense $\alpha^{(2)}$ and $\gamma^{(2)}$ into a single angle. Consecutive rotations about the z-axis are cumulative and can be expressed as a single rotation (c.f. Fig. 6.8B–E). Transformations here are similar to Hahn echoes (c.f. section 6.2.1). Note that in step D the Euler angle $\alpha'^{(2)}$ was supplated with $\alpha''^{(2)}$ to unite $\alpha'^{(2)}$ and $\gamma^{(3)}$:

$$\begin{aligned} \alpha''^{(2)}(\omega) &= \alpha'^{(2)}(\omega) + \gamma^{(3)}(\omega) \\ \gamma'^{(3)}(\omega) &= 0. \end{aligned} \tag{6.65}$$

In accordance with the derivation for Hahn echoes, a total transfer function is given by integrating over the individual signals at each offset (6.17).

It is maximized if the signals add up constructively, i.e.

$$\omega(\tau^{(1,2)} - \tau^{(2,3)}) + \alpha^{(1)} - \alpha''^{(2)}(\omega) \stackrel{!}{=} \text{const} = 0 \tag{6.66}$$

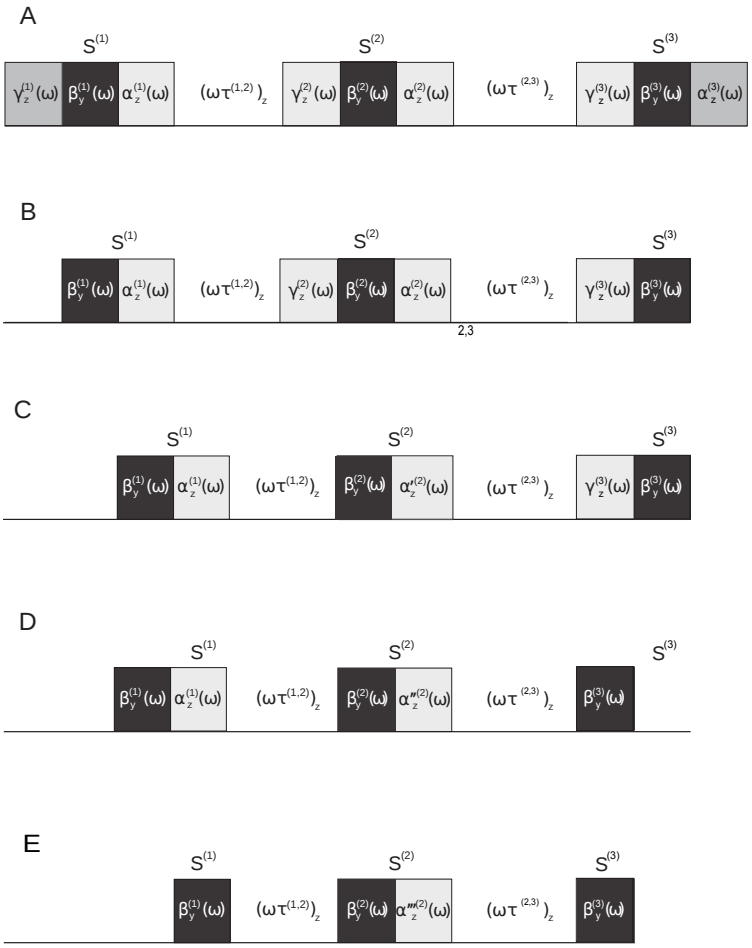

Figure 6.8: Characterization of general $\frac{\pi}{2}-\pi-\frac{\pi}{2}$ sequences based on the offset-dependent Euler angles of the three pulses $S^{(1)}$, $S^{(2)}$ and $S^{(3)}$ and the offset-dependent z rotations during the delays $\tau^{(1,2)}$ and $\tau^{(1,2)}$. To guide the eye, the Euler rotations $\beta_y^{(1)}$, $\beta_y^{(2)}$ and $\beta_y^{(3)}$ are represented by black rectangles. (A) The first Euler rotation $\gamma_z^{(1)}$ (indicated by a dark grey rectangle) has no effect on initial z magnetization and has been dropped in the simplified sequence of rotations shown in (B). This sequence can be further simplified by replacing the Euler angles $\gamma^{(2)}$ and $\alpha^{(2)}$ by the Euler angles $\alpha'^{(2)} = \alpha^{(2)} - \gamma^{(2)}$ and $\gamma'^{(2)} = 0$ (not shown), resulting in (C). Sequences (B) and (C) are equivalent in the presence of the +1QF before and a -1QF filter after $S^{(2)}$ (or if $\beta^{(2)} = \pi$). In the presence of the ± 1 quantum filters (or for $\beta^{(2)} = \pi$), sequence (C) can be transformed to the equivalent sequence (D) by replacing the Euler angles $\alpha^{(1)}$ and $\alpha'^{(2)}$ by $\alpha''^{(1)} = 0$ (not shown) and $\alpha''^{(2)} = \alpha'^{(2)} - \alpha^{(1)}$. Finally, Sequence (D) can be collapsed into sequence (E) by replacing the Euler angles $\gamma^{(3)}$ and $\alpha''^{(2)}$ by $\alpha'''^{(2)} = \alpha''^{(2)} + \gamma^{(3)}$.

Similar to Hahn echoes, the rotations can be expressed as offset-dependent effective evolution times, which can be split up into a linear and a non-linear part. For the $\frac{\pi}{2} - \pi - \frac{\pi}{2}$ sequence, similar to (6.24), we can write:

$$\tau^{(2,3)} = \tau^{(1,2)} + \delta \tag{6.67}$$

with the offset-independent auxiliary delay

$$\delta = \tau_\alpha^{(1)\mathrm{lin}} - \tau_\alpha''^{(2)\mathrm{lin}} \tag{6.68}$$

and the offset-dependent delay

$$\epsilon(\omega) = \frac{\alpha^{(1)\mathrm{nl}}(\omega) - \alpha''^{(2)\mathrm{nl}}(\omega)}{\omega}. \tag{6.69}$$

The conditions for ideal $\frac{\pi}{2} - \pi - \frac{\pi}{2}$ sequences can be summarized as :

$$\beta_{\mathrm{ideal}}^{(1)}(\omega) = \frac{\pi}{2}, \tag{6.70}$$

$$\beta_{\mathrm{ideal}}^{(2)}(\omega) = \pi, \tag{6.71}$$

$$\beta_{\mathrm{ideal}}^{(2)}(\omega) = \frac{\pi}{2}, \tag{6.72}$$

$$\epsilon_{\mathrm{ideal}}(\omega) = 0. \tag{6.73}$$

6.3.2 Derivation of transfer function

As outline in section 6.3.1, the transfer during the first two pulses of the $\frac{\pi}{2} - \pi - \frac{\pi}{2}$ sequence is equivalent to the transfer during a Hahn echo sequence. Therefore, the derivation is confined to the transfer carried out by the remaining pulse.

The state after the second pulse $S^{(2)}$ after the -1-quantum coherence filter is

$$\rho(T^{(1)} + T^{(2)}) = s_{\text{Hahn echo}}(\tau^{(2,3)})I^- \tag{6.74}$$

which is transformed by the third pulse to

$$\rho(T^{tot}) = s_{\text{Hahn echo}}(\tau^{(2,3)})U_3 I^- U_3^\dagger \tag{6.75}$$

The propagator of the third pulse can be decomposed into three successive Euler rotations:

$$U_3 = U_z^{\alpha^{(3)}} U_y^{\beta^{(3)}} U_z^{\gamma^{(3)}} \tag{6.76}$$

As outlined in section 6.3.1, in the presence of a 0-quantum filter after the third pulse, the rotation about $\alpha^{(3)}$ can be neglected. In addition, $s_{\text{Hahn echo}}$ is a prefactor and for simplicity left out in the following, where states are annotated with an asterisk.

$$\rho(T^{tot})^* = U_y^{\beta^{(3)}} U_z^{\gamma^{(3)}} I^- U_z^{\gamma^{(3)}\dagger} U_y^{\beta^{(3)}\dagger} \tag{6.77}$$

(6.77) can be rewritten as

$$\rho(T^{tot})^* = U_y^{\beta^{(3)}} e^{\mathrm{i}\gamma^{(3)}} I^- U_y^{\beta^{(3)}\dagger} \tag{6.78}$$

When I^- is expressed in a cartesian basis, we find

$$\begin{aligned} \rho(T^{tot})^* &= U_y^{\beta^{(3)}} e^{\mathrm{i}\gamma^{(3)}} (I_x - \mathrm{i}I_y) U_y^{\beta^{(3)}\dagger} \\ &= \cos\beta^{(3)} I_x - e^{i\gamma^{(3)}} (\sin\beta^{(3)} I_z - \mathrm{i}I_y). \end{aligned} \tag{6.79}$$

In the presence of a 0-quantum coherence filter, only the I_z term survives. Thus we find

$$\begin{aligned} \rho(T^{tot}) &= -\sin\beta^{(3)} I_z s_{\text{Hahn echo}}(\tau^{(2,3)}) \\ &= e^{-\mathrm{i}\pi} s_{\text{Hahn echo}}(\tau^{(2,3)}) \sin\beta^{(3)} I_z \\ &= f_3 \cdot s_{\text{Hahn echo}} \cdot I_z \end{aligned} \tag{6.80}$$

We insert the right-hand side of (6.13 and obtain the transfer function (6.64).

6.3.3 Pre-optimization strategy

The pre-optimization of cooperative seed sequences is an iterative process and schematically outlined in the following. It is based on the gradient of the PP quality factor Φ_{PP} for the first pulse $S^{(1)}$ of duration $T^{(1)}$ and the third pulse $S^{(3)}$ of duration $T^{(3)}$ and the gradient of a UR quality factor Φ_{UR} for the second pulse $S^{(2)}$ of duration $T^{(3)}$. In each iteration, these two gradients are calculated using the following steps, where steps 1-6 are repeated for all offsets that are considered in the chosen discretization of the desired bandwidth of the echo sequence.

1. Calculate the forward evolution of the initial density operator $\rho(0) = 2I_z$ under the excitation pulse $S^{(1)}$ yielding $\rho(t)$ for $0 \leq t \leq T^{(1)}$ and calculate the projection of $\rho(T^{(1)})$ onto I^+, i.e. apply a +1QF to $\rho(T^{(1)})$ to yield $\tilde{\rho}(T^{(1)}) = \langle I^+|\rho(T^{(1)})\rangle I^+$. Compute the effective propagator during the first pulse $U_{\text{tot}}^{(1)} = \mathcal{T}\prod_t U(t)$ with $0 \leq t \leq T^{(1)}$, where $\mathcal{T}$ denotes the Dyson time ordering operator. In case of pulses with an auxiliary delay $\delta \neq 0$, the final propagation $U_f^{(1)}$ of the first pulse $S^{(1)}$ is modified by free evolution about $-\delta$, i.e. $U_f^{(1)} \to e^{\mathrm{i}\delta\omega I_z} U_f^{(1)}$.

2. Calculate the forward evolution of the propagator $U^{(2)}(t)$ for the refocusing pulse $S^{(2)}$, starting with $U^{(2)}(T^{(1)}) = \mathbf{1}$ and yielding $U^{(2)}(t)$ for $T^{(1)} \leq t \leq T^{(1)} + T^{(2)}$. In the following, we use the short-hand notation $U_{\text{tot}}^{(2)} := U^{(2)}(T^{(1)} + T^{(2)})$ for the total propagator of the refocusing pulse $S^{(2)}$.

3. Calculate the state $\tilde{\rho}(T^{(1)} + T^{(2)})$ after the second pulse $S^{(2)}$ using the total propagator of the second pulse $U_{\text{tot}}^{(2)}$ as $\tilde{\rho}(T^{(1)} + T^{(2)}) = U_{\text{tot}}^{(2)} \tilde{\rho}(T^{(1)}) U_{\text{tot}}^{(2)\dagger}$ and apply a

-1-quantum filter to $\tilde{\rho}(T^{(1)} + T^{(2)})$ to yield $\tilde{\tilde{\rho}}(T^{(1)} + T^{(2)})$. Compute the forward evolution of of the density operator $\tilde{\tilde{\rho}}(T^{(1)} + T^{(2)})$ under the third pulse $S^{(3)}$ yielding $\tilde{\tilde{\rho}}(t)$ for $T^{(2)} < t \leq T^{(3)}$. Compute the effective propagator during the first pulse $U_{\text{tot}}^{(3)} = \mathcal{T} \prod_t U(t)$ with $T^{(1)} \leq t \leq T^{(3)}$.

4. Determine the ideal rotation axis of the refocusing pulse $S^{(2)}$ based on the Euler angle $\alpha^{(1)}$ of the effective propagator $U_{\text{tot}}^{(1)}$ of the first pulse $S^{(1)}$ and the Euler angle $\gamma^{(3)}$ of the effective propagator of the third pulse $S^{(3)}$. We outlined a procedure to obtain Euler angles from propagators in section 6.1.1. The Euler angle $\alpha^{(1)}$ corresponds to the phase of transverse magnetization acquired after the first pulse $S^{(1)}$, $\pi - \gamma^{(3)}$ corresponds to the required phase of transverse magnetization before the third pulse in order to maximize transfer to I_z. The ideal azimuth angle φ of the respective in-plane π pulse $S^{(2)}$ is given by $(\pi - \gamma^{(3)} - \alpha^{(1)})/2$. Discontinuities of the phases as a function of offset are remedied by a standard phase unwrapping procedure about π of the azimuthal angle φ. This provides the target propagator $U_{\text{target}} = \exp\{-\mathrm{i}\pi(I_x \cos\varphi_{\text{ref}} + I_y \sin\varphi_{\text{ref}})\}$ for the refocusing pulse, which by construction varies smoothly as a function of offset and hence does not have any sudden changes of the global phase factor, which could cause the algorithm to be trapped in local maxima.

5. Set the costate $\lambda(T^{(1)} + T^{(2)} + T^{(3)})$ to I_z and evolve it backwards to yield $\lambda(t)$ for $T^{(2)} \leq t \leq T^{(3)}$ and apply the -1-quantum coherence filter to yield $\tilde{\lambda}(T^{(1)} + T^{(2)})$

6. Set the co-propagator $\Lambda(T^{(1)} + T^{(2)}) = U_{\text{target}}^{(2)}$ and evolve it backwards to yield $\Lambda(t)$ for $T^{(1)} < t < T^{(2)}$.

7. The costate $\tilde{\lambda}(T^{(1)} + T^{(2)})$ is propagated backwards about $U_{\text{tot}}^{(2)}$ to yield $\tilde{\lambda}(T^{(1)})$. The +1-quantum coherence filter is applied to obtain $\tilde{\tilde{\lambda}}(T^{(1)})$. If $\delta \neq 0$, ensure that the backward propagation at $T^{(1)}$ is preceded by a free backward evolution about δ, i.e. the propagator at $U^{\dagger}T^{(1)}$ at $T^{(1)}$ is adapted: $U^{\dagger}(T^{(1)}) \rightarrow U^{\dagger}(T^{(1)})e^{-\mathrm{i}\omega\delta I_z}$. Compute the backward evolution of $\tilde{\tilde{\lambda}}(t)$ for $0 < t < T^{(1)}$

8. To improve the refocusing pulse $S^{(2)}$, we consider a universal rotation (UR) quality factor

$$\Phi_{\text{UR}}^{(2)} = \text{Re}\langle U_{\text{target}}^{(2)} | U_{\text{tot}}^{(2)} \rangle$$

for this iteration. Note that Φ_{UR} is sensitive to the global phase of the propagator $U_{tot}^{(2)}$.[59] Based on the first-order gradient of Φ_{UR},[59] the following simple updating scheme is used for the refocusing pulse $S^{(2)}$:

$$u_x(t) \rightarrow u_x'(t) = u_x(t) - \epsilon\overline{\text{Re}\langle\Lambda(t)|iI_xU^{(2)}(t)\rangle}$$

and

$$u_y(t) \rightarrow u_y'(t) = u_y(t) - \epsilon\overline{\text{Re}\langle\Lambda(t)|iI_yU^{(2)}(t)\rangle}$$

for $T^{(1)} < t \leq T^{(1)} + T^{(2)}$, where the overscore indicates the average over all offsets ω of the desired bandwidth of the echo sequence and ϵ is a step size.

9. To improve the pulses $S^{(1)}$ and $S^{(3)}$, we consider a generalized point-to-point (PP) quality factor

$$\Phi_{\mathrm{PP}}^{(3)} = \mathrm{Re}\langle\tilde{\lambda}(T^{(1)} + T^{(2)} + T^{(3)})|\tilde{\tilde{\rho}}(T^{(1)} + T^{(2)} + T^{(3)})\rangle$$

and

$$\Phi_{\mathrm{PP}}(1) = \mathrm{Re}\langle\tilde{\tilde{\lambda}}(T^{(1)})|\tilde{\rho}(T^{(1)})\rangle$$

for this iteration. Based on the first-order gradient of Φ_{PP},[59] the following simple updating scheme is used for the $S^{(3)}$ pulse for $T^{(2)} \leq t \leq T^{(3)}$

$$u_x(t) \to u_x'(t) = u_x(t) - \epsilon' \overline{\mathrm{Re}\langle\tilde{\lambda}(t)|i[I_x, \tilde{\tilde{\rho}}(t)]\rangle}$$
$$u_y(t) \to u_y'(t) = u_x(t) - \epsilon' \overline{\mathrm{Re}\langle\tilde{\lambda}(t)|i[I_y, \tilde{\tilde{\rho}}(t)]\rangle}$$

and the $S^{(1)}$ pulse for $0 \leq t \leq T^{(1)}$ and

$$u_x(t) \to u_x'(t) = u_x(t) - \epsilon' \overline{\mathrm{Re}\langle\tilde{\tilde{\lambda}}(t)|i[I_x, \tilde{\rho}(t)]\rangle}$$
$$u_y(t) \to u_y'(t) = u_x(t) - \epsilon' \overline{\mathrm{Re}\langle\tilde{\tilde{\lambda}}(t)|i[I_y, \tilde{\rho}(t)]\rangle},$$

where the overscore indicates the average over all offsets ω of the desired bandwidth of the echo sequence and ϵ' is a step size.

10. Optimize the step sizes in ϵ and ϵ' in steps 8 and 9 to maximize the actual global quality factor Φ defined in Eq. (4.30) in this iteration.

A simplified scheme is schown in figure 6.9.

6.3.4 Families of $\frac{\pi}{2} - \pi - \frac{\pi}{2}$ sequences

In order to compare the performance of optimized COOP $\frac{\pi}{2} - \pi - \frac{\pi}{2}$ sequences with conventional approaches, it is helpful to define the following families of echo sequences. For all families of echo sequences considered below, the Euler angle $\beta^{(1)}(\omega)$ of the first pulse $S^{(1)}$ is assumed to approach the ideal value of $\pi/2$, the Euler angle $\beta^{(2)}(\omega)$ of the second pulse $S^{(2)}$ is assumed to approach the ideal value of π and the Euler angle $\beta^{(3)}$ of the third pulse $S^{(3)}$ is assumed to approach the ideal value of $\pi/2$ according to conditions (6.70-6.72). Furthermore, it is assumed that the general condition (6.73) is fulfilled. However, the different families of $\frac{\pi}{2} - \pi - \frac{\pi}{2}$ sequences impose different constraints for the Euler angles $\gamma^{(1)}(\omega)$, $\alpha^{(1)}(\omega)$, $\alpha'^{(2)}$, $\gamma^{(3)}(\omega)$ and $\alpha^{(3)}(\omega)$ (c.f. Eq. 6.14) and the echo family with the largest number of degrees of freedom is expected to

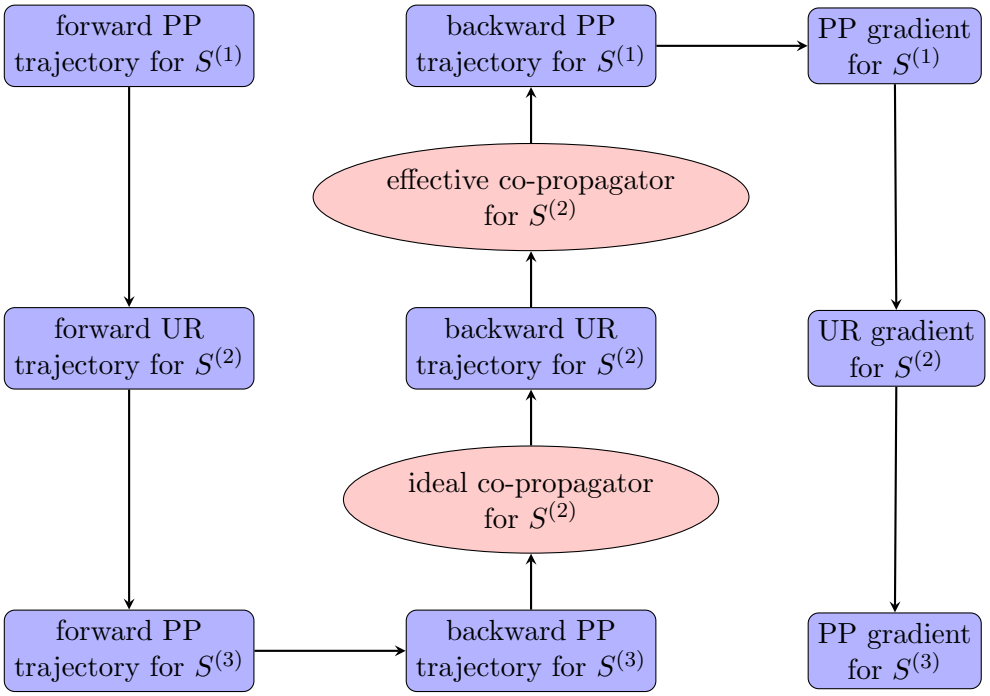

Figure 6.9: Here the computation steps during the pre-optimization procedure are shown in a simplified scheme for the pre-optimization of $\frac{\pi}{2} - \pi - \frac{\pi}{2}$ sequences.

provide the best echo performance in the desired range of offset frequencies (c.f. Table 6.4).

Ideal $\frac{\pi}{2} - \pi - \frac{\pi}{2}$ sequence based on hard pulses

The idealized echo sequence

$$(\pi/2)_y \text{ - } \tau^{(1,2)} \text{ - } (\pi)_y \text{ - } \tau^{(2,3)} \text{ - } (\pi/2)_y$$

consists of infinitely strong δ pulses of negligible durations and $\tau^{(2,3)} = \tau^{(1,2)}$. In this limiting case, the Euler angles are offset-independent and given by $\beta^{(1)}(\omega) = \pi/2$, $\beta^{(2)}(\omega) = \pi$, $\beta^{(3)}(\omega) = \pi/2$, $\gamma^{(1)}(\omega) = \alpha^{(1)}(\omega) = \alpha'^{(2)}(\omega) = \gamma^{(3)}(\omega) = \alpha^{(3)}(\omega) = 0$ (c.f. Fig. 6.10G and sequence G in Table 6.4).

$\frac{\pi}{2} - \pi - \frac{\pi}{2}$ sequence based on rectangular pulses

The most widely used conventional $\frac{\pi}{2} - \pi - \frac{\pi}{2}$ experiments consist of rectangular pulses. In case of $\frac{\pi}{2} - \pi - \frac{\pi}{2}$ sequences, the effective evolution periods of $2T_{\pi/2}/\pi$ cancel each other, the auxiliary delay is 0.

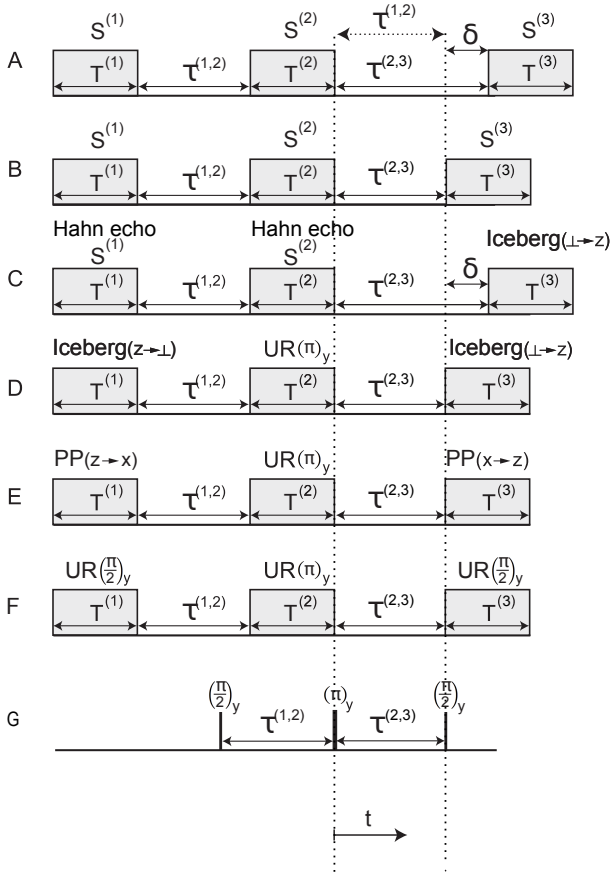

Figure 6.10: Pictorial representation of the different families of $\frac{\pi}{2}-\pi-\frac{\pi}{2}$ sequences discussed in the text. A, B: s^2 COOP$_\delta$ $\frac{\pi}{2}-\pi-\frac{\pi}{2}$ sequence based on cooperative $\pi/2$ and π pulses (denoted $S^{(1)}$, $S^{(2)}$ and $S^{(3)}$, respectively) with auxiliary delay $\delta \neq 0$ (A) and $\delta = 0$ (B). C: s^2 COOP Hahn echo sequence combined with a time reversed ICEBERG pulse whose phase is shifted by π. The original ICEBERG pulse transforms initial z-magnetization into transverse magnetization with a linear phase. A time-reversed and phase-shifted ICEBERG pulse transforms initial transverse magnetization with a linear phase into z-magnetization. D-E: $\frac{\pi}{2}-\pi-\frac{\pi}{2}$ sequences comprised of individually optimized pulses. In sequence E, ICEBERG pulses are combined with a BURBOP π pulse and a time-reversed and phase-shifted ICEBERG pulse. In sequence F, the first pulse $S^{(1)}$ corresponds to an excitation point-to-point pulse, that transforms initial z-magnetization to x-magnetization. The third pulse is a time-reversed and phase-shifted PP pulse. F: here two $\pi/2$ BURBOP pulses are combined with a π BURBOP pulse G corresponding to the ideal $\frac{\pi}{2}-\pi-\frac{\pi}{2}$ sequence consisting of hard pulses with negligible pulse duration. The delay between the end of the $S^{(1)}$ and the $S^{(2)}$ pulse is denoted $\tau^{(1,2)}$, the delay between the end of the $S^{(2)}$ and the $S^{(3)}$ pulse is referred to by $\tau^{(2,3)}$. All sequences are drawn such that the ends of the $S^{(2)}$ pulses are aligned, as indicated by the first vertical dotted line. The second vertical dotted line is shifted relative to the first vertical dotted line by $\tau^{(2,3)}$ to guide the eye. For ideal sequences the signal is maximized if $\tau^{(1,2)} = \tau^{(2,3)}$.

Table 6.4: Ideal $\tau^{(2,3)}$ and degrees of freedom of the Euler angles for different families of $\frac{\pi}{2} - \pi - \frac{\pi}{2}$ sequences

	$\frac{\pi}{2} - \pi - \frac{\pi}{2}$ family	$\tau^{(2,3)}$	$\gamma^{(1)}$	$\alpha^{(1)}$	$\alpha'^{(2)}$	$\gamma^{(3)}$	$\alpha^{(3)}$
A	$S^{(1)}$–$S^{(2)}$–$S^{(3)}$ ($\delta \neq 0$)	$\tau^{(1,2)} + \delta$	•	$\bullet^a$	$\bullet^a$	$\bullet^a$	•
B	$S^{(1)}$–$S^{(2)}$–$S^{(3)}$ ($\delta = 0$)	$\tau^{(1,2)}$	•	•	$\alpha^{(1)} - \gamma^{(3)}$	•	•
C	$S^{(1)}_{\text{Hahn echo}}$ – $S^{(2)}_{\text{Hahn echo}}$ – ICEBERG	$\delta_{\text{Hahn echo}} - \delta_{\text{ICEBERG}}$	•	$\bullet^a$	$\bullet^a$	$\bullet^b$	•
D	ICEBERG – BURBUP – ICEBERG	$\tau^{(1,2)}$	•	$\bullet^b$	0	$-\alpha^{(1)}$	•
E	BEBOP – BURBOP – BEBOP	$\tau^{(1,2)}$	•	0	0	0	•
F	BURBOP – BURBOP – BURBOP	$\tau^{(1,2)}$	0	0	0	0	0
G	$(\pi/2)_y$ - $(\pi)_y$ - $(\pi/2)_y$	$\tau^{(1,2)}$	0	0	0	0	0

$S^{(i)}_{\text{sequence}}$	ith s^2 COOP pulse. In case s^2 COOP pulses from experiments other than $\frac{\pi}{2} - \pi - \frac{\pi}{2}$ experiments are used, the subscript indicates the experiment that was used to build the threepulse sequence
$\tau^{(1,2)}$	delay between the first pulse $S^{(1)}$ and the second pulse$S^{(2)}$
$\tau^{(2,3)}$	delay between the second pulse $S^{(2)}$ and the third pulse $S^{(3)}$
•	the angle is not fixed, i.e. it constitutes a degree of freedom
$\bullet^a$	the angle itself is not fixed, however a linear combination of all angles in a row marked as $\bullet^a$ is fixed
$\bullet^b$	the nonlinear contributions to the angle have to be 0
0	the angle has a fixed value 0

$\frac{\pi}{2} - \pi - \frac{\pi}{2}$ sequence based on universal rotation pulses

A naive approach to realize the ideal echo sequence would be to implement both the excitation pulse and the refocusing pulse as a universal rotation (UR) pulse [73] with finite durations $T^{(1)}$, $T^{(2)}$ and $T^{(3)}$, respectively:

$$\text{UR}(\pi/2)_y \text{ - } \tau^{(1,2)} \text{ - UR}(\pi)_y \text{ - } \tau^{(2,3)} \text{ - UR}(\pi/2)_y.$$

The UR pulses approximate all the Euler angles of the ideal echo sequence based on hard pulses for a desired range of offset frequencies, i.e. $\gamma^{(1)}(\omega) = \alpha^{(1)}(\omega) = \alpha'^{(2)}(\omega) = \gamma^{(3)}(\omega) = \alpha^{(3)}(\omega) = 0$ and $\tau^{(2,3)} = \tau^{(1,2)}$ (c.f. Fig. 6.10 F and sequence F in Table 6.4).

$\frac{\pi}{2} - \pi - \frac{\pi}{2}$ sequences based on point-to-point (PP) excitation and UR refocusing pulses without auxiliary delay δ

As discussed above, the Euler angles $\gamma^{(1)}(\omega)$ and $\alpha^{(3)}$ are irrelevant for the $\frac{\pi}{2} - \pi - \frac{\pi}{2}$ echo sequence starting with initial and final z magnetization (c.f. Fig. 6.8 B). Hence, the excitation pulse can be implemented by point-to-point (PP) pulses [62] with arbitrary $\gamma^{(1)}(\omega)$ and $\alpha^{(3)}(\omega)$ that is designed to bring initial z-magnetization to the x-axis for a desired range of offset frequencies and:

$$\text{PP}(z \rightarrow x) \text{ - } \tau^{(1,2)} \text{ - UR}(\pi)_x \text{ - } \tau^{(2,3)} \text{ - PP}(x \rightarrow z).$$

The remaining conditions $\alpha^{(1)}(\omega) = \alpha'^{(2)}(\omega) = 0$ imply both $\delta = 0$ (c.f. Eqs. 6.22, 6.23 and 6.25) and $\epsilon(\omega) = 0$ (c.f. Eq. 6.67) and hence $\tau^{(2,3)} = \tau^{(1,2)}$ (c.f. Eq. 6.69) as in the ideal echo sequence, (c.f. Fig. 6.10 E and sequence E in Table 6.4).

$\frac{\pi}{2} - \pi - \frac{\pi}{2}$ sequence based on Iceberg excitation and UR refocusing pulses

The conditions $\alpha^{(1)}(\omega) = 0$ and $\gamma^{(3)} = 0$ can be relaxed by using ICEBERG pulses [8] (and time-reversed and phase-shifted ICEBERG pulses) that transform initial z magnetization to transverse magnetization with a *linear* phase dependence as a function of offset:

$$\text{Iceberg}(z \rightarrow \perp) \text{ - } \tau^{(1,2)} \text{ - } \text{UR}(\pi)_x \text{ - } \tau^{(2,3)} \text{ - } \text{Iceberg}(\perp \rightarrow z)$$

In this family of $\frac{\pi}{2} - \pi - \frac{\pi}{2}$ sequences, the conditions $\alpha^{(1)}(\omega) = 0$ and $\gamma^{(3)}(\omega) = 0$ are relaxed to the condition $\alpha^{(1)\text{nl}}(\omega) = \gamma^{(3)\text{nl}} = 0$, i.e. only the non-linear term of the Euler angles $\alpha^{(1)}(\omega)$ and $\gamma^{(3)}(\omega)$ have to vanish. The use of a UR refocusing pulse still requires $\alpha'^{(2)}(\omega) = 0$. The general condition $\epsilon(\omega) = 0$ (Eq. 6.73) still needs to be fulfilled. In analogy to Eq. (6.22) the non-zero linear term $\alpha^{(1)\text{lin}}(\omega)$ implies a non-zero auxiliary delay of the first pulse $S^{(1)}$ of $\tau_\alpha^{(1)}$ and which, after refocusing and time- and phase inversion is completely cancelled by by $\gamma^{(3)}$ (c.f. Eq. 6.68). Therefore, according to Eq. (6.67) the second interpulse delay $\tau^{(2,3)} = \tau^{(1,2)}$ identical to the interpulse delay $\tau^{(12)}$ (see Fig. 6.4 D and sequence D in Table 6.2).

$\frac{\pi}{2} - \pi - \frac{\pi}{2}$ sequences based on s^2 COOP Hahn Echo sequences and ICEBERG pulses

The conditions for the angle $\alpha^{(1)}(\omega)$ and the difference angle $\alpha'^{(2)}(\omega)$ can be further relaxed if the first pulse $S^{(1)}$ and second pulse $S^{(2)}$ are concurrently optimized such that individual pulse errors can be mutually cancelled. Here, for the second delay $\tau^{(2,3)}$ we find that $\tau^{(2,3)} = \tau^{(1,2)} + \delta_{\text{Hahn echo}} - \delta_{\text{ICEBERG}}$, i.e. $\tau^{(2,3)} = \tau^{(1,2)}$ *only* if the effective evolution period introduced by the Hahn echo cancels the effective evolution period introduced by the ICEBERG pulse. The DOFs in ICEBERG pulses were discussed in section 6.3.4 and the ones of cooperative echoes were outlined in section 6.2.4 and 6.2.4. The DOFs in $\frac{\pi}{2} - \pi - \frac{\pi}{2}$ sequence comprised of a s^2 COOP Hahn echo sequence and a time-reversed and phase-shifted ICEBERG pulse equal the joint DOFs of both sequences.

$\frac{\pi}{2} - \pi - \frac{\pi}{2}$ sequences based on cooperative pulses with equally long interpulse delays $\tau^{(1,2)}$ and $\tau^{(2,3)}$

Mutual cancellation of errors in s^2 COOP sequences was introduced in section 6.2.4 and employed in $\frac{\pi}{2} - \pi - \frac{\pi}{2}$ sequences that contain a cooperative Hahn echo. However, it is possible to incorporate further degrees of freedom by optimizing a $\frac{\pi}{2} - \pi - \frac{\pi}{2}$ sequence of cooperative pulses, where phase errors of *all three* pulses compensate each other. In this section we reqire equally long interpulse delays, i.e. $\tau^{(2,3)} = \tau^{(1,2)}$.

Based on (6.65), only the condition

$$\alpha'^{(2)}(\omega) + \gamma^{(3)}(\omega) - \alpha^{(1)}(\omega) \stackrel{!}{=} 0 \tag{6.81}$$

has to be fulfilled. The nonlinear contributions to the respective Euler angles can be non-zero as long as they mutually cancel. (c.f. Fig 6.10 B and table 6.4 B).

$\frac{\pi}{2} - \pi - \frac{\pi}{2}$ sequences based on cooperative pulses with $\tau^{(1,2)} \neq \tau^{(2,3)}$

In general, it is not necessary to require $\tau^{(2,3)} = \tau^{(1,2)}$. Therefore we obtain

$$\alpha'^{(2)}(\omega) + \gamma^{(3)}(\omega) - \alpha^{(1)}(\omega) \stackrel{!}{=} \omega(\tau^{(2,3)} - \tau^{(1,2)}) \tag{6.82}$$

which requires the sum of the non-linear terms $\alpha'^{(2)\mathrm{nl}}(\omega)$, $-\alpha^{(1)\mathrm{nl}}(\omega)$ and γ^3 to be zero. The echo delay is given by $\tau^{(2,3)} = \tau^{(1,2)} + \delta$ with the auxiliary delay $\delta = -\tau_\alpha^{(1)} + \tau_{\alpha'}^{(2)} + \tau_\gamma^{(3)}$, c.f. Fig. 6.10 A and sequence A in Table 6.4. Broadband s^2 COOP$_\delta$ $\frac{\pi}{2} - \pi - \frac{\pi}{2}$ sequences can also be optimized based on the filter-based global quality factor Φ in 4.30. However, in this case the propagator $U^{(2)}$ for the refocusing pulse $S^{(2)}$ is replaced by the $U'^{(2)} = \exp\{-i\omega\delta I_z\}U^{(2)}$ which represents the overall propagator of $S^{(2)}$ followed by the auxiliary delay δ. Alternatively, it is also possible to directly optimize the conditions (6.70 - 6.73) for the Euler angles.

6.3.5 Effective evolution time representation of $\frac{\pi}{2} - \pi - \frac{\pi}{2}$ sequences

In section 6.2.5 we introduced graphical representation of offset-dependent effective evolution periods for Hahn echo sequences. Here we introduce similar representations for $\frac{\pi}{2} - \pi - \frac{\pi}{2}$ sequences.

Fig. 6.11 shows a schematic representation of an $\frac{\pi}{2} - \pi - \frac{\pi}{2}$ (with gradient or phasecycle coherence transfer pathway selection) sequence consisting of three pulses. Here, $\tau_\gamma^{(1)}$ and $\tau_\alpha^{(3)}$ are not shown because the initial and final state I_z are invariant under z rotations. Based on the Euler angles $\alpha^{(1)}$, $\gamma^{(2)}$, $\alpha^{(2)}$, $\gamma^{(3)}$ and the derived angles $\alpha'^{(2)}$, $\alpha''^{(2)}$ $\alpha'''^{(2)}$ and (Eq. 6.65 and Fig. 6.8 C) and $\alpha''^{(2)}$ (Eq. 6.83 and Fig. 6.8 D), effective evolution periods $\tau_\alpha^{(1)}$, $\tau_\gamma^{(2)}$, $\tau_\alpha^{(2)}$, $\tau_\alpha'^{(2)}$, $\tau_\alpha''^{(2)}$ and $\tau_\alpha'''^{(2)}$ are defined below and are used in the following graphical representations of echo sequences:

Type I

Type I plots separately depict $\tau_\alpha^{(1)}(\omega)$ at the end of the excitation pulse, $\tau_\gamma^{(2)}(\omega)$ at the beginning of the refocusing pulse, $\tau_\alpha^{(2)}(\omega)$ at the end of the refocusing pulse and $\tau_\gamma^{(3)}(\omega)$ at the beginning of the third pulse.

Type II

We define the effective evolution periods $\tau_\alpha'^{(1)}$, $\tau_\gamma'^{(2)}$, $\tau_\alpha'^{(2)}$ and $\tau_\gamma'^{(3)}$ as

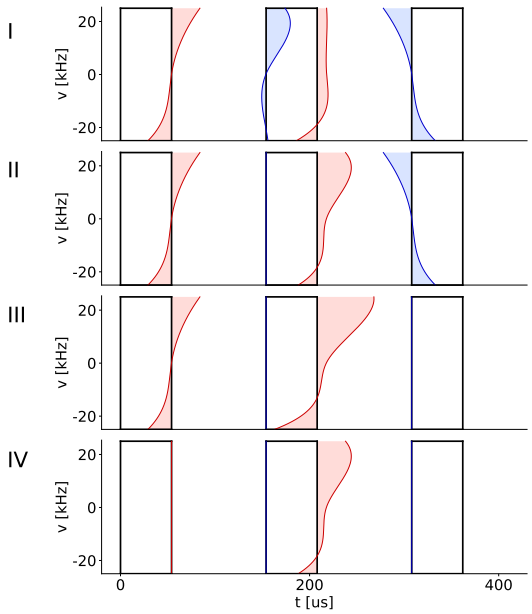

Figure 6.11: Graphical representation of the effective evolution periods for a Hahn Echo sequence. Panels I to IV show plot types introduced in section 6.3.5.

$$\begin{aligned}
\tau_\alpha'^{(1)} &= \tau_\alpha^{(1)} \\
\tau_\gamma'^{(2)} &= 0 \\
\tau_\alpha'^{(2)} &= \tau_\alpha^{(2)} - \tau_\gamma^{(2)} \\
\tau_\gamma'^{(3)} &= \tau_\gamma^{(3)}.
\end{aligned}$$

In essence, compared to type I, for each offset the period $\tau_\gamma^{(2)}$ is moved from the leading edge of the refocusing pulse to the trailing edge and merged (with inverted sign) with $\tau_\alpha^{(2)}$ to yield $\tau_\alpha'^{(2)}$.

Type III

In the third representation also the period $\tau_\gamma'^{(3)} = \tau_\gamma^{(3)}$ is moved from the leading edge of the third pulse to the trailing edge of the refocusing pulse and merged with $\tau_\alpha'^{(2)}$ to yield $\tau_\alpha''^{(2)}$:

$$\begin{aligned}
\tau_\alpha^{\prime\prime(1)} &= \tau_\alpha^{\prime(1)} \\
\tau_\gamma^{\prime\prime(2)} &= 0 \\
\tau_\alpha^{\prime\prime(2)} &= \tau_\alpha^{\prime(2)} + \tau_\gamma^{(3)} \\
\tau_\gamma^{\prime\prime(3)} &= 0.
\end{aligned}$$

Correspondingly, the Euler angle $\alpha^{\prime\prime(2)}$ is defined as

$$\begin{aligned}
\alpha^{\prime\prime(2)} &= \alpha^{\prime(2)} + \gamma^{(3)} \\
&= \alpha^{(2)} + \gamma^{(3)} - \gamma^{(2)},
\end{aligned} \tag{6.83}$$

c.f. Fig. 6.8 D. This is possible because the effects of $\tau_\alpha^{(2)}$ and $\tau^{(2,3)}$ commute and hence, $\tau_\gamma^{(3)}$ can be moved from the leading edge of the third pulse to the end of the refocusing pulse and finally merged (with inverted sign) with $\tau_\alpha^{\prime(2)}$ at the trailing edge of the refocusing pulse to yield $\tau_\alpha^{\prime\prime(2)}$.

Type IV

In the type IV representation the period $\tau_\alpha^{\prime\prime(1)} = \tau_\alpha^{(1)}$ is moved from the trailing edge of the excitation pulse to the trailing edge of the refocusing pulse and merged (with inverted sign) with $\tau_\alpha^{\prime\prime(2)}$ to yield $\tau_\alpha^{\prime\prime\prime(2)}$:

$$\begin{aligned}
\tau_\alpha^{\prime\prime\prime(1)} &= 0 \\
\tau_\gamma^{\prime\prime\prime(2)} &= 0 \\
\tau_\alpha^{\prime\prime\prime(2)} &= \tau_\alpha^{\prime\prime(2)} - \tau_\alpha^{(1)} \\
\tau_\gamma^{\prime\prime\prime(3)} &= 0.
\end{aligned}$$

Correspondingly, the Euler angle $\alpha^{\prime\prime\prime(2)}$ is defined as

$$\begin{aligned}
\alpha^{\prime\prime\prime(2)} &= \alpha^{\prime\prime(2)} - \alpha^{(1)} \\
&= \alpha^{(2)} + \gamma^{(3)} - (\alpha^{(1)} + \gamma^{(2)}),
\end{aligned} \tag{6.84}$$

In order to maximize the signal, we require that

$$\tau^{(2,3)} = \tau^{(1,2)} - \delta = \tau^{(1,2)} - \tau_\alpha^{\prime\prime\prime(2)}$$

If $\tau_\alpha^{\prime\prime\prime(2)}$ is a vertical line in type IV representation, i.e. if is offset-independent, the signal components coherently add up for all offset frequencies, resulting in a maximum signal.

Although the display type IV clearly illustrates the effective delay δ, display type III is also very helpful to see how well the offset-dependent variations of the effective evolution periods $\tau_\alpha^{(1)}$ and $\tau_\alpha^{\prime\prime(2)}$ associated with the excitation and inversion pulses match (up to an offset-independent auxiliary delay δ), c.f. Eq. (6.67).

6.3.6 Selective s^2 COOP sequences

Hitherto we describe general procedures for optimizing rf (or mw) controls to steer spin systems from a given initial state to a target state. For application in MRI [108,149] and for specific EPR systems [151] band-selective pulses are required.

An extensive review of all the techniques employed to generate selective pulses is beyond the scope of this work. [152] Here we present a method that is used in conjunction wit optimum control, which was introduced by Conolly in 1986 [153] and later expanded by Janich et al. [108]

In the original approach by Connolly, the effect of the pulse was examined for a specific offset range; a desired response D was defined which was set to y for the excited offsets ω and z for the remaining offsets. However. the thusly obtained pulses exhibited no selectivity beyond the scope the pulses were optimized for, i.e. when leaving the optimized offset range $\Delta\omega$, the behaviour of the pulse was undefined.

Fermi's golden rule and linear response theory can be applied here: Fermi's golden rule is the result of first order time-dependent perturbation theory and is most accurate when the perturbation is small, i.e. the states of a system change little during interaction with an external field. The equations governing the dynamics of a spin system, i.e. Bloch equations and the Liouville-von Neumann equation are highly non-linear and the response of a spin system to an rf field is only linear for small tip angles.

Outside the selected range and neighbouring transition regions, the flip angle of a band-selective pulse is 0 and linear response theory and Fermi's golden rule are applicable. The desired frequency response of the system for the spins that are not to be excited is 0.

Therefore we apply a passband filter to the controls before computing fidelities and matching of optimization constraints as well as to the gradient after it was obtained by the algorithm laid out in section 4.4.3.

Note that the discrete Fourier transform which was employed in this procedure corresponds to a linear transformation of the controls. In theory it should be possible to obtain the transformation matrix and introduce additional constraint functions λ.

6.3.7 Compensation of transient effects

The pulses optimized here were (partly) designed with application in EPR in mind. Pulsed EPR spectroscopy occurs on a timescale three orders of magnitude smaller

than nuclear magnetic resonance which makes the response time of the resonator non-negligible compared to the duration of a single timeslice. In 2012, Spindler et al.[86] suggested an algorithm that considers these transient effects, assuming the frequency response (from which the impulse response can be computed) is known. We were unable to perform successfull pulse sequence optimization with their algorithm due to weak frequency deconvolution artefacts and adapted the algorithm by Hincks et al. outlined in section 4.4.7 for multipulse sequences.[87] Here, a distortion operator is computed for each individual pulse and separately applied to the corresponding controls and gradients.

7 Results

7.1 Hahn echoes

7.1.1 Nomenclature

In this study, thousands of COOP echo sequences with different total duration, relative durations of excitation and refocusing pulses and relative auxiliary delays were systematically optimized. In order to be able to refer to some specific pulse sequences that are discussed in more detail in the following, a short-hand nomenclature is defined. We use the acronym COBBLE (COoperative Broad-Band amplitude-Limited Echo) for optimized COOP echo pulses considered here. As a superscript, the total pulse duration T_{tot} is indicated in units of μs and the auxiliary delay δ is indicated in units of μs as a subscript. Furthermore, a prime indicates that the pulse sequence was optimized without the pre-optimization approach discussed in section 7.1.2. For example, the sequence COBBLE_{50}^{500} corresponds to a COOP echo sequence of duration $T_{tot} = 500$ μs and $\delta = 50$ μs that was optimized including the pre-optimization approach, whereas the sequence $\text{COBBLE}'^{500}_{50}$ was optimized without pre-optimization.

7.1.2 Optimization strategies

In section 4.4.3, we discussed the optimization of the overall figure of merit Φ, c.f. Eq. (4.30), representing the echo amplitude created by spins in the considered offset range if a crusher gradient or an EXORCYCLE coherence selection phase cycle are applied. However, if pulses are optimized directly based on the gradient of Φ (c.f. Eq. 4.31), the optimization algorithm frequently is trapped in local maxima. In Fig. 7.1 A, this is illustrated by a histogram of the achieved figures of merit Φ for 200 random initial sequences, which were optimized for a maximum number of 3000 iterations. In this example, the excitation pulse had a duration of 300 μs, the refocusing pulse had a duration of 300 μs and and the auxiliary delay was $\delta = 0$, c.f. Eq. (6.25).

If pulses are not optimized based on the gradient of Φ but using only the pre-optimization algorithm described in section 6.2.3, the distribution of the resulting figures of merit is much more narrow and skewed towards high values of Φ as shown in Fig. 7.1 B for the same number of 3000 iterations (and a similar computation time). In contrast to the direct optimization based on the gradient of Φ, the global phase factor of the propagator of the refocusing pulse is taken into account in the pre-optimization. As shown previously, this strongly reduces the probability to get trapped in local maxima in the optimization of propagators.[73,108]

Fig. 7.1 C shows the distribution of obtained Φ values if the initial sequences are pre-optimized for 1500 iterations and if the resulting pulse sequences are then further

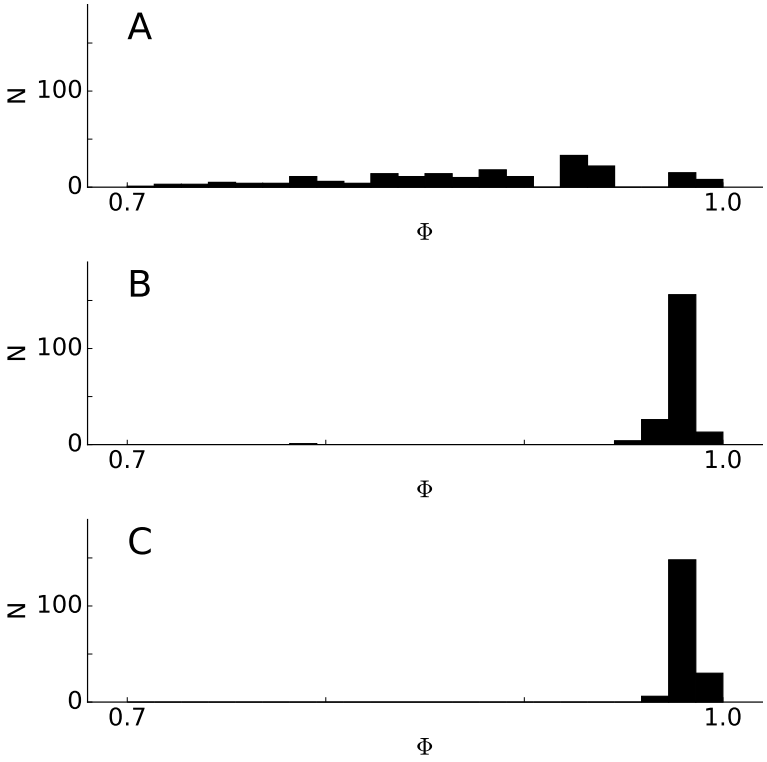

Figure 7.1: Histograms of the achieved figure of merits Φ for 200 optimized echo sequences starting with random excitation and refocusing pulses with durations $T^{(1)} = T^{(2)} = 300$ μs using (A) direct optimization of echo sequences based on the gradient of Φ for 3000 iterations, (B) pre-optimization of echo sequences as described in section 6.2.3 for 3000 iterations, and (C) two-step approach based on pre-optimization for 1500 iterations followed by optimizations using the gradient of Φ for 1500 iterations. N is the number of echo sequences found in each bin.

optimized based on the gradient of Φ (c.f. Eq. 4.31) for 1500 iterations. This two-step approach results in excellent convergence of the algorithm and in a sharp distribution close to the maximum found quality factor of 0.99.

7.1.3 Magnetization at echo time

In section 6.2.1 we introduced a general definition of the transfer function for s^2 COOP Hahn echo sequences. This transfer function corresponds to an averaged x-magnetization during an echo experiment using EXORCYCLE coherence transfer selection or crusher gradients.

Figure 7.2 depicts x- and y-components of the magnetization vector for a COBBLE_{60}^{600} sequence that was optimized for an offset range of ± 25 kHz with and without an additional delay of 1 ms.

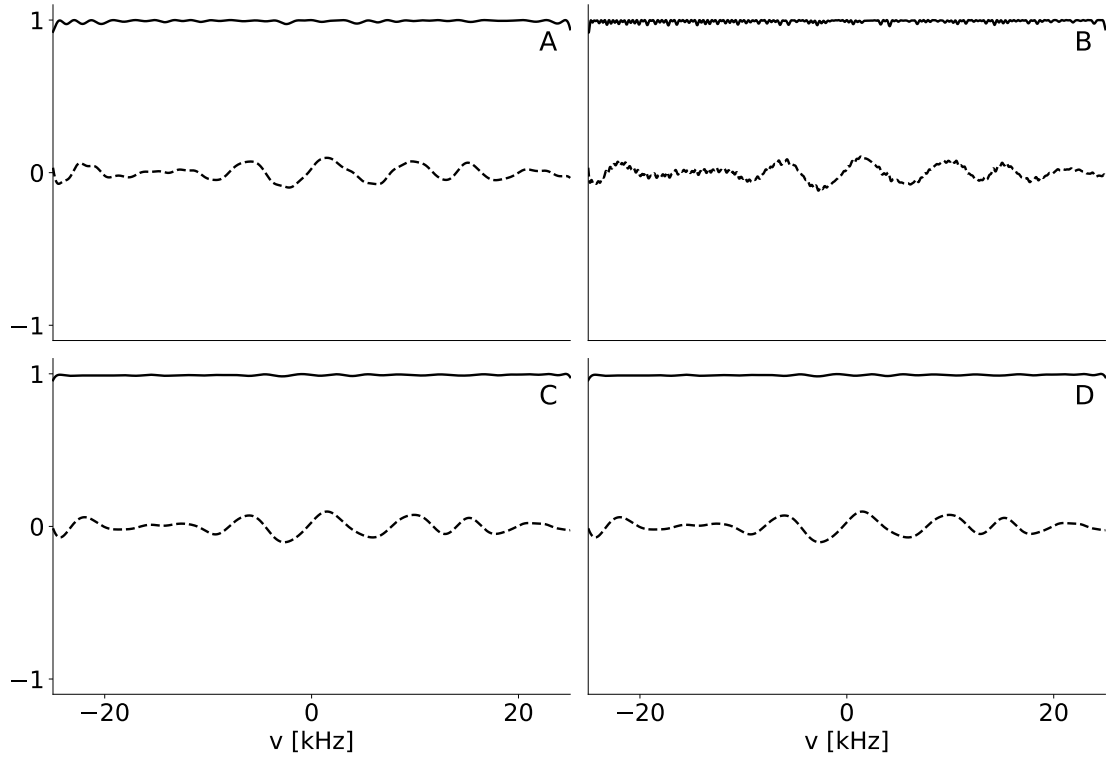

Figure 7.2: Here the offset-dependent x-component (solid curve) and y-component (dashed curve) of magnetization of a COBBLE$_{60}^{600}$ sequence are depicted at echo time for the optimized range of ±25 kHz. Simulation was carried out with an interpulse delay $\tau^{(1,2)} = 0$ (A and C) and $\tau^{(1,2)} = 1$ ms (B and D), with (C and D) and without (A and B) an EXORCYCLE.

Figure 7.2 A and C show simulations without an additional delay $\tau^{(1,2)} = 0$ and B and D with an additonal delay $\tau^{(1,2)} = 1$ ms.

In section 6.2.1 we showed that in the presence of EXORCYCLE coherence transfer selection or crusher gradients the echo amplitude and phase is independent from the delay. This is reflected in Figs. 7.2 C and D which are indiscernible.

Figs. 7.2 A and B demonstrate that even without explicit coherence transfer pathway selection, given sufficiently high transfer efficiencies Φ, the optimized transfer pathway is the predominant one and other transfer pathways, though present, can be neglected.

7.1.4 Quality factor landscapes

In conventional Hahn echo sequences based on rectangular pulses with equal rf amplitude, the pulse duration of the 180° refocusing pulse is twice as long as the duration of the 90° excitation pulse. However, for broadband COOP echo sequences, the optimal relative durations of excitation and refocusing pulses are a priori unknown. Similarly, the optimal relative auxiliary delay δ/T^{tot} is a priori unknown. In order to determine

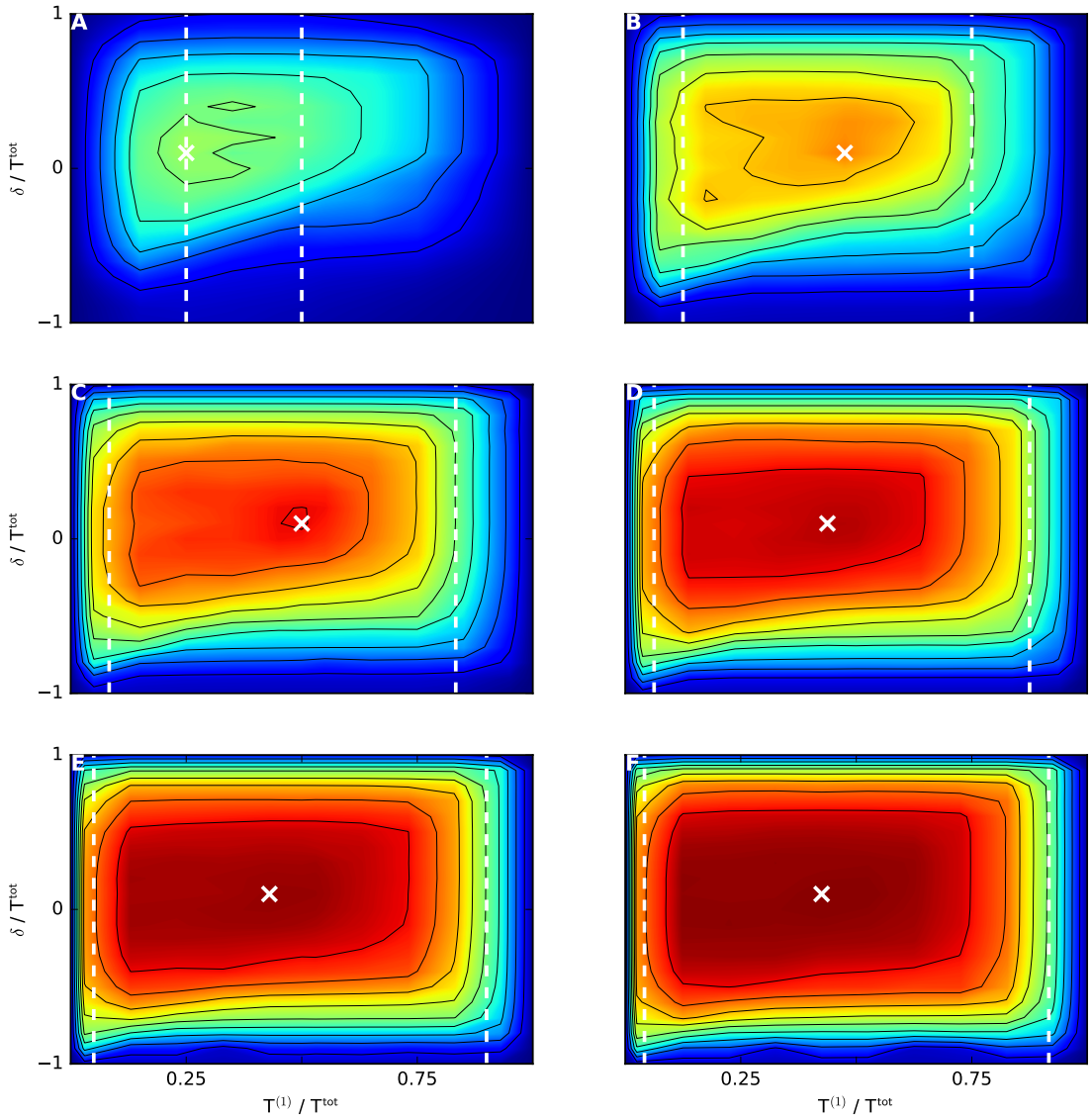

Figure 7.3: For total pulse durations $T^{tot} = T^{(1)} + T^{(2)}$ of (A) 100 μs, (B) 200 μs, (C) 300 μs, (D) 400 μs, (E) 500 μs, (F) 600 μs, the quality factor Φ is shown as a function of $T^{(1)}/T^{tot}$ (x axis) and of the relative auxiliary delay δ/T^{tot}. A white cross indicates the location of the best quality factor for each T^{tot} (c.f. table 7.1). Contour lines are plotted at Φ levels between 0 and 1 with increments of 0.1. The left white dashed curve indicates the duration of a rectangular $\pi/2$ pulse with the same amplitude, the right white dashed curve corresponds to the duration of a rectangular π pulse.

Table 7.1: Durations $T^{(1)}$ of the excitation pulse and T^{tot} of the refocusing pulse for COBBLE sequences optimized for specific total durations $T^{tot} = T^{(1)} + T^{(2)}$. The table also summarizes the relative durations $T^{(1)}/T^{(2)}$, the relative duration of the auxiliary delay δ/T^{tot} and the achieved figure of merit Φ.

$T^{tot}[\mu s]$	$T^{(1)}[\mu s]$	$T^{(2)}[\mu s]$	$T^{(1)}/T^{tot}$	δ/T^{tot}	Φ
100	25	75	0.25	0.1	0.55
200	95	105	0.48	0.1	0.78
300	150	150	0.50	0.1	0.91
400	175	225	0.43	0.1	0.96
500	215	285	0.43	0.1	0.98
600	255	345	0.43	0.1	0.99

the best values of relative pulse durations $T^{(1)}/T^{tot}$ and $T^{(2)}/T^{tot}$ and of the optimal relative auxiliary delay, a large number of pulse optimizations for a set of total pulse durations 100 μs $\leq T^{tot} \leq$ 600 μs, a range of relative pulse durations $0 \leq T^{(1)}/T^{tot} \leq 1$ (corresponding to $0 \leq T^{(2)}/T^{tot} = 1 - T^{(1)}/T^{tot} \leq 1$) and of relative auxiliary delays $-1 \leq \delta/T^{tot} \leq 1$ were carried out.

In Fig. 7.3, plots of the figure of merit Φ are shown as a function of $T^{(1)}/T^{tot}$ and δ/T^{tot} for Hahn echoes with a total duration $T^{tot} = 100, 200, 300, 400, 500$ and 600 μs. The optimal combination of $T^{(1)}/T^{tot}$ and δ/T^{tot} is indicated by a cross. Table 7.1 summarizes the best values for all considered pulse durations.

It is interesting to note that except for the shortest considered total pulse duration $T^{tot} = 100$ μs, the best COBBLE performance is found for $T^{(1)}/T^{tot} \approx 0.43$, i.e. the duration $T^{(2)}$ of the refocusing pulse is only about 30% longer than the duration $T^{(1)}$ of the excitation pulse, in contrast to echo sequences based on rectangular pulses.

Note that the concurrent optimization of COBBLE sequences can only mutually cancel offset-dependent phase errors (given by the Euler angles $\alpha^{(1)}(\nu)$, $\gamma^{(2)}(\nu)$, and $\alpha^{(2)}(\nu)$) of the excitation and refocusing pulses, whereas errors in the Euler angles $\beta^{(1)}(\nu)$ and $\beta^{(2)}(\nu)$ cannot be corrected. For excitation pulses shorter than the duration of a rectangular 90° pulse, it is impossible even for on-resonance spins to reach an Euler angle $\beta^{(1)}$ of $\pi/2$, resulting in a sharp drop of Φ for $T^{(1)} < 1/(4\nu_{\mathrm{rf}}^{\max}) = 25$ μs. Furthermore, short excitation pulses are able to bring a large portion of the magnetization vectors to the transverse plane (corresponding to $\beta^{(1)}(\nu) \approx \pi/2$), albeit with in general nonlinear phase as a function of offset (at least for offsets that are large compared to the rf amplitude).[86] However, the non-linear offset-dependent phase of the excited magnetization vectors can be compensated by concurrently optimized refocusing pulses of sufficiently long duration.

Conversely, for refocusing pulses shorter than the duration of a rectangular 180° pulse, even for on-resonance spins it is impossible to reach an Euler angle $\beta^{(2)}$ of π, resulting in a sharp drop of Φ for $T^{(2)} < 1/(2\nu_{\mathrm{rf}}^{\max}) = 50$ μs. Furthermore, the offset-dependent

transfer function s (c.f. Eqs. 6.15-6.17) is only linearly dependent on $\sin(\beta^{(1)})$, whereas it depends quadratically on $\sin(\beta^{(2)}/2)$, i.e. a given error of $\beta^{(2)}$ results in a larger reduction of the figure of merit compared to the same relative error of $\beta^{(1)}$. Overall, these properties qualitatively explain the observed asymmetry with respect to $T^{(1)}$ and $T^{(2)}$ in Fig. 7.3. The pulse shapes are discussed further in section 7.1.10.

The white dashed lines in Fig. 7.3 correspond to the durations of rectangular $\pi/2$ and π with an rf amplitude corresponding to the limit of 10 kHz in the optimization. They reflect the minimum duration τ_{min} required to achieve a flip angle $\beta^{(1)} = \pi/2$ and $\beta^{(2)} = \pi$. At these boundaries a sharp drop of the fidelity is noticable. At approx. $2\tau_{\text{min}}$, Fig. 7.3 shows the beginning of a plateau, where the quality factor landscape is flat. Within this region, there is little difference between the optimized sequences with respect to application in experiments.

Furthermore, note that slightly better performing pulses are found for positive values for δ/T^{tot}. These findings are in agreement with systematic studies of pulses that generate a linear phase slope:

- excitation pulses could be replaced with ICEBERG pulses,[8] optimization of ICEBERG pulses is strongly skewed towards negative values $\delta/\tau_{\text{ICEBERG}}$.
- the refocusing pulse could be supplanted by a double-ICEBERG pulse,[75] an $\alpha'(\omega) = 0 \cdot \omega$ proved to be the best conditions.

In conclusion, the best performing COBBLE sequences were found for $\delta = 0.1$ and $T^{(2)} = 1.33 \cdot T^{(1)}$ with $T^{(1)} \geq 50$ μs and $T^{(2)} \geq 100$ μs.

7.1.5 Analysis of echo pulses in terms of effective evolution periods

In Figs. 7.4 and 7.5, plots of the effective evolution periods introduced in section 6.2.5 are shown. In each of these figures, panel I depicts a pulse sequence using plot type I, where the effective evolution time $\tau_\alpha^{(1)}$ is shown at the trailing edge of the excitation pulse and $\tau_\gamma^{(2)}$ and $\tau_\alpha^{(2)}$ are shown at the leading and trailing edges of the refocusing pulse, respectively. Panel II corresponds to plot type II, where $\tau_\alpha^{(1)}$ is unchanged,$\tau_\gamma^{\prime(2)}$ vanishes and $\tau_\alpha^{\prime(2)}$ is shown at the trailing edge of the refocusing pulse. Panel III corresponds to plot type III, where all effective evolution information is condensed into $\tau_\alpha^{\prime\prime(2)}$ at the trailing edge of the refocusing pulse.

Panel IV corresponds to plot type IV, which shows the principal phase front of $\tau_0(\omega)$ for a non vanishing interpulse delay $\tau^{(1,2)} = 200$ μs (c.f. section 6.3.5).

Fig. 7.4 shows a sequence of rectangular pulses for a total duration of 75 μs with $T^{(1)} = 25$ μs and $T^{(2)} = 50$ μs (A) and a COBBLE_{10}^{100} sequence with a $T^{(1)} = 25$ μs and a $T^{(2)} = 75$ μs (B) as well as the best combination of optimized ICEBERG[8] and BURBOP[73] pulses (c.f. section 6.2.4) that was found for a total duration $T^{tot} = 500$ μs and an auxiliary delay $\delta = 56$ μs (C), where the duration of the ICEBERG pulse is $T^{(1)} = 80$ μs and the duration of the BURBOP pulse is $T^{(2)} = 420$ μs. Fig. 7.4 D shows the best $\text{COBBLE}_{100}^{\prime 500}$ sequence with individual durations of the excitation and refocusing pulses of $T^{(1)} = 250$ μs and $T^{(2)} = 250$ μs.

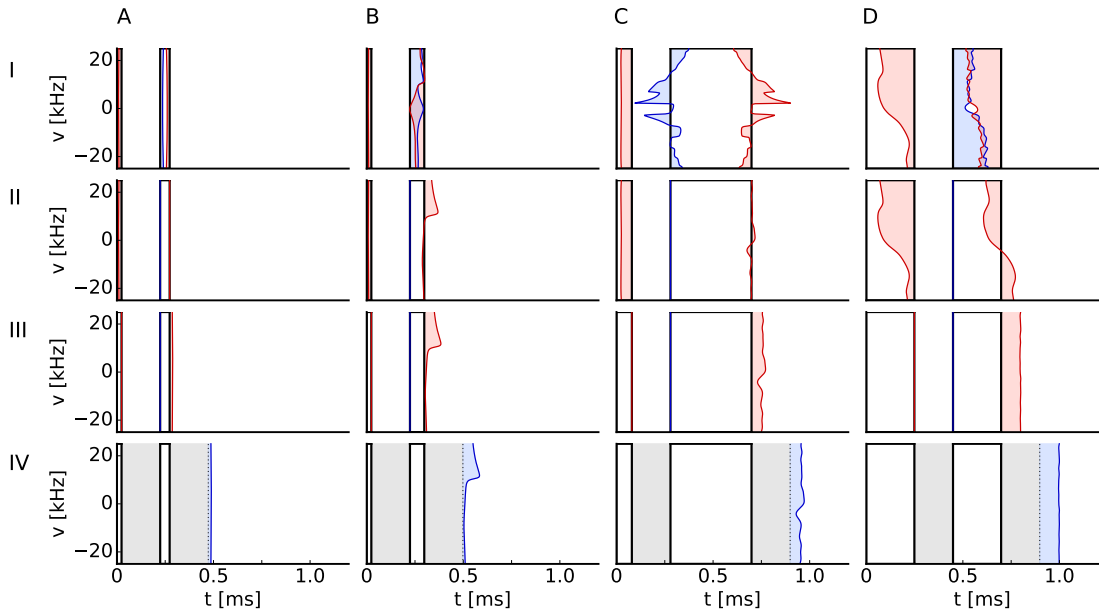

Figure 7.4: Graphical representation of the effective evolution periods for a Hahn Echo sequence composed of rectangular pulses with a total duration T^{tot} of 75 μs (A), a COBBLE$_{10}^{100}$ sequence (B), a Hahn echo sequence with an ICEBERG pulse and BURBOP pulse with a total duration T^{tot} = 500 μs (C) and a COBBLE$_{100}^{500}$ sequence (D). Panels I to IV correspond to the plot types introduced in section 6.2.5.

Table 7.2: Parameters of the WURST pulses studied in Figs. 1-4.

pulse	$T[\mu s]$	B1 [kHz]	n	k
Hahn echo ($T^{tot} = 500\mu s$) $S^{(1)}$	333	3.8	$2.89 \cdot 10^1$	$1.35 \cdot 10^9$
Hahn echo ($T^{tot} = 500\mu s$) $S^{(2)}$	166	10	$1.26 \cdot 10^5$	$2.56 \cdot 10^9$
Hahn echo ($T^{tot} = 1000\mu s$) $S^{(1)}$	666	3.0	$3.81 \cdot 10^1$	$8.18 \cdot 10^8$
Hahn echo ($T^{tot} = 1000\mu s$) $S^{(2)}$	333	10	$1.53 \cdot 10^1$	$1.55 \cdot 10^9$

Fig. 7.5 shows effective evolution periods of optimized echo sequences with vanishing auxiliary delay ($\delta = 0$) and of WURST pulses optimized according to the Böhlen-Bodenhausen scheme (parameters are listen in Table 7.2). Fig. 7.5 A corresponds to the best combination of individually optimized BEBOP [62] and BURBOP [73] pulses (c.f. section 6.2.4) that was found for a total duration T^{tot} = 500 μs with $T^{(1)}$ = 177.5 μs and $T^{(2)}$ = 330 μs. Fig. 7.5 B corresponds to the best COBBLE$_0^{500}$ sequence with ($T^{(1)}$ = 250 μs and $T^{(2)}$ = 250 μs).

Fig. 7.5 (C) corresponds to an Echo experiment with WURST pulses according to the Böhlen-Bodenhausen scheme with a total pulse duration T^{tot} = 500 μs, (D) to one with a total pulse duration T^{tot} = 1000 μs.

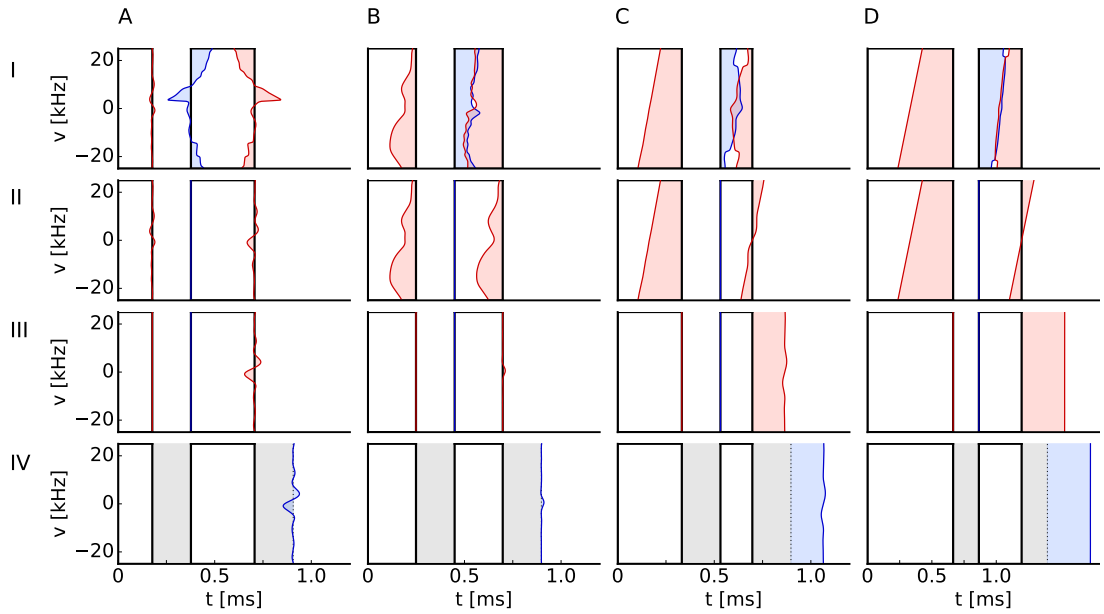

Figure 7.5: Graphical representation of the effective evolution periods for a Hahn echo sequence comprised of a BEBOP excitation and a BURBOP refocusing pulse with a total pulse duration $T^{tot} = 500$ μs (A), a COBBLE$'^{500}_0$ sequence (B), and Böhlen-Bodenhause chirp echo sequences with a total pulse duration $T^{tot} = 500$ μs (C) and $T^{tot} = 1000$ μs (D). Panels I to IV correspond to the plot types introduced in section 6.2.5.

Note the good match of the effective evolution periods $\tau_\alpha^{(1)}$ and $\tau_\alpha^{\prime(2)}$ of the excitation and refocusing pulses in the COBBLE sequences shown in panel II of Figs. 7.4 D and 7.5 B (c.f. condition 6.51), resulting in an overall phase front (c.f. panels III and IV of Figs. 7.4 D and 7.4B) that is approximately offset independent, as desired.

7.1.6 Performance of different Hahn echo families

Here we compare the performance of the optimized COBBLE sequences with an echo sequence based on rectangular pulses and with conventional families of echo sequences discussed in sections 6.2.4-6.2.4.

In order to compare the performance of COBBLE sequences with the performance of echo sequences consisting of combinations of

(A) individually optimized UR($\pi/2$) excitation and UR(π) refocusing pulses (c.f. section 6.2.4)

(B) individually optimized PP($z \rightarrow x$) excitation and UR(π) refocusing pulses (c.f. section 6.2.4),

(C) individually optimized ICEBERG($z \rightarrow \perp$) excitation and UR(π) refocusing pulses (c.f. section 6.2.4),

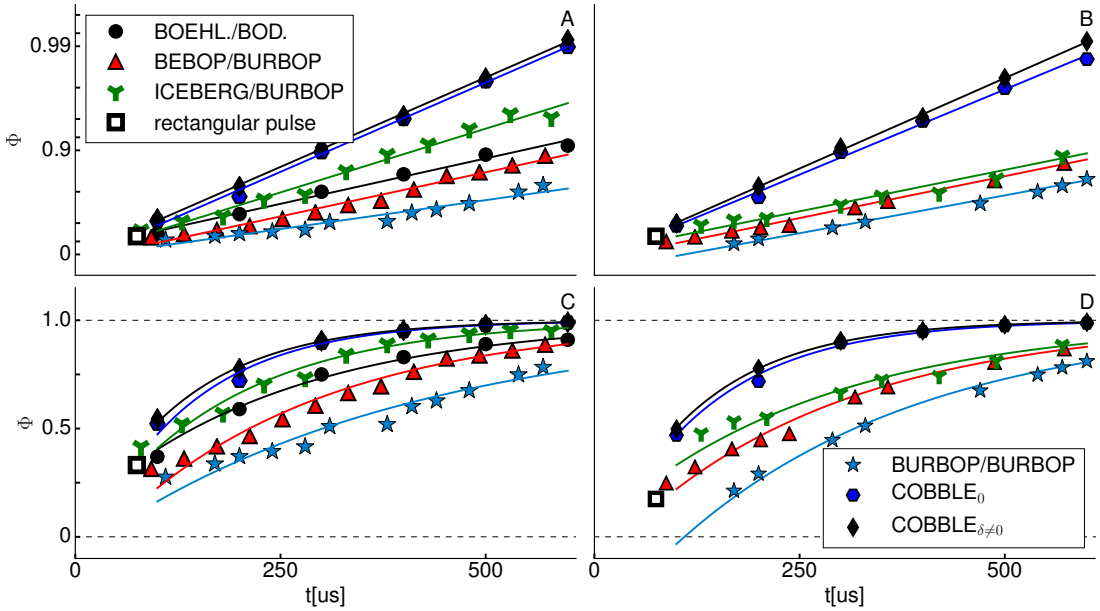

Figure 7.6: Maximum quality factor Φ plotted on a logarithmic (A) and linear (C) scale as a function of the total pulse duration T^{tot} for the optimal relative duration $T^{(1)}/T^{tot}$. The maximum quality factor for Hahn echo sequences with equal durations of the excitation and the refocusing pulse, i.e. $T^{(1)} = T^{(2)}$ is shown on a logarithmic (B) and linear scale (D).

we determined the best combinations of individually optimized pulses with durations $T^{(1)}$ and $T^{(2)}$ for the considered total pulse durations T^{tot}. The COBBLE sequences employed here were optimized with the pre-optimization algorithm discussed in section 6.2.3 and correspond to those discussed in section 7.1.10.

Fig. 7.6 shows so-called TOP (time-optimal pulse) curves,[59,154] which represent the best performance (in terms of the global quality factor Φ, c.f. Eq. 4.30) of each family of pulses as a function of total pulse duration T^{tot}. For a given total pulse duration, the combination of ICEBERG excitation and BURBOP refocusing pulses are the best echo sequences based on individually optimized pulse, as expected based on the number of degrees of freedom (c.f. Table 6.2). However, a significant further performance gain is found for the COBBLE sequences for a given total pulse duration. Conversely, the same echo performance can be achieved with shorter COBBLE pulses. For example, Fig. 7.6 shows that a figure of merit of 0.9 can be achieved by a COBBLE sequence with a duration of about 280 μs, whereas the best sequence consisting of individually optimized pulses is 40% longer. Furthermore, a more detailed analysis reveals that in contrast to COOP echo sequences, where the excitation and inversion pulses have comparable durations, the best sequences consisting of ICEBERG and BURBOP pulses have very short excitation pulses but very long refocusing pulses (c.f. Fig. 7.7). In applications, where long refocusing pulses are undesired (e.g. if coupling evolution during refocusing pulses is to be minimized), the performance gain of COBBLE pulses is even larger.

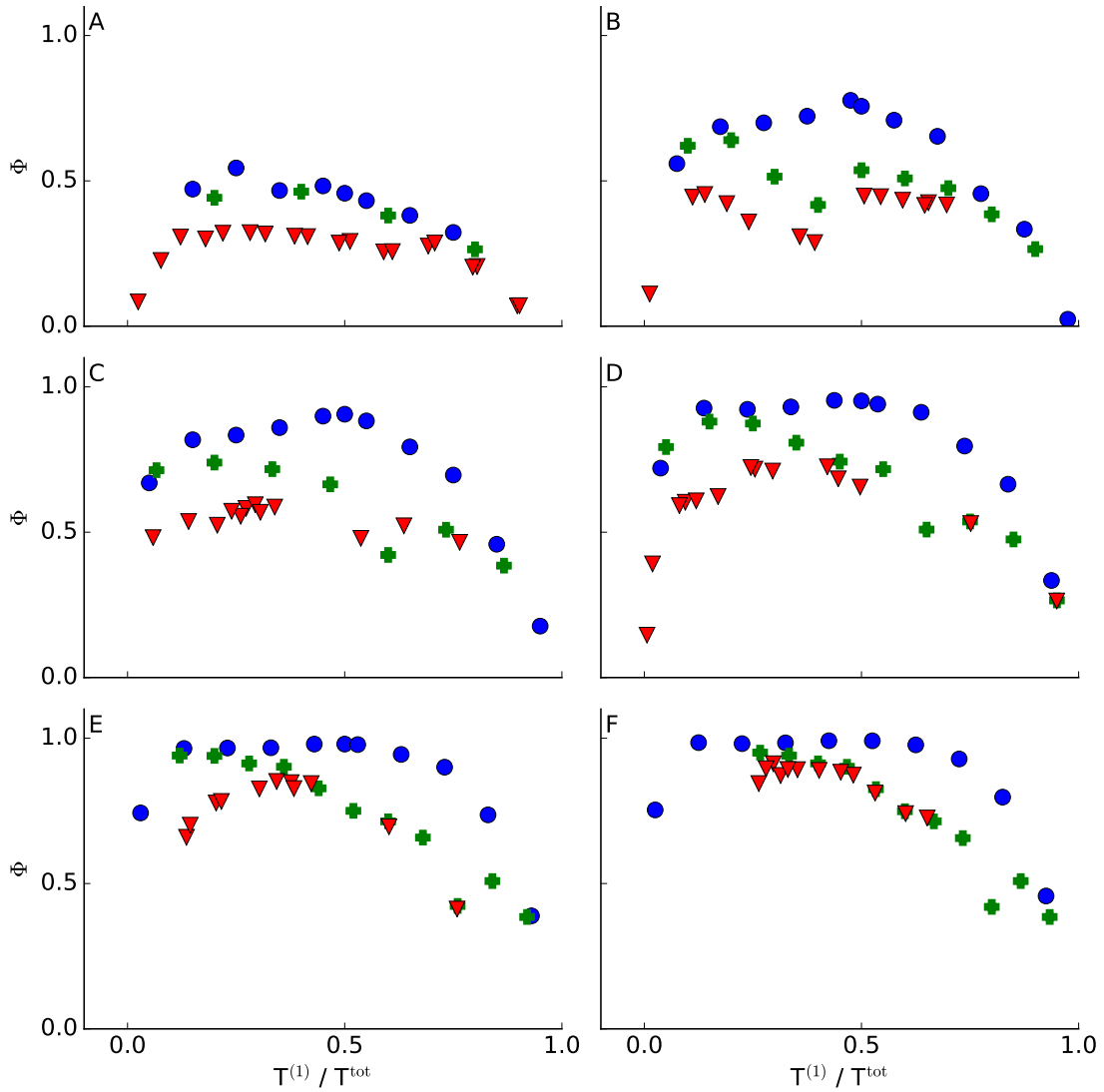

Figure 7.7: For total pulse durations $T^{tot} = T^{(1)} + T^{(2)}$ of (A) 100 μs, (B) 200 μs, (C) 300 μs, (D) 400 μs, (E) 500 μs, (F) 600 μs, the optimal quality factor Φ is shown as a function of $T^{(1)}/T^{tot}$ for arbitrary δ.● represent s2-COOP pulses, ▼ individually optimized excitation pulses with $\delta = 0$ (BEBOP) combined with individually optimized refocusing pulses (BURBOP), and ✚ individually optimized excitation pulses with $\delta \neq 0$ (ICEBERG) combined with individually optimized refocusing pulses (BURBOP).

This is illustrated in Fig 7.6, which shows TOP curves as a function of T^{tot} for echoes comprised of excitation and refocusing pulses of the same duration ($T^{(1)} \approx T^{(2)}$). In this case, a figure of merit of 0.9 can be achieved by a COBBLE sequence with a total duration of about 300 μs, whereas the best sequence consisting of individually optimized pulses is more than twice as long.

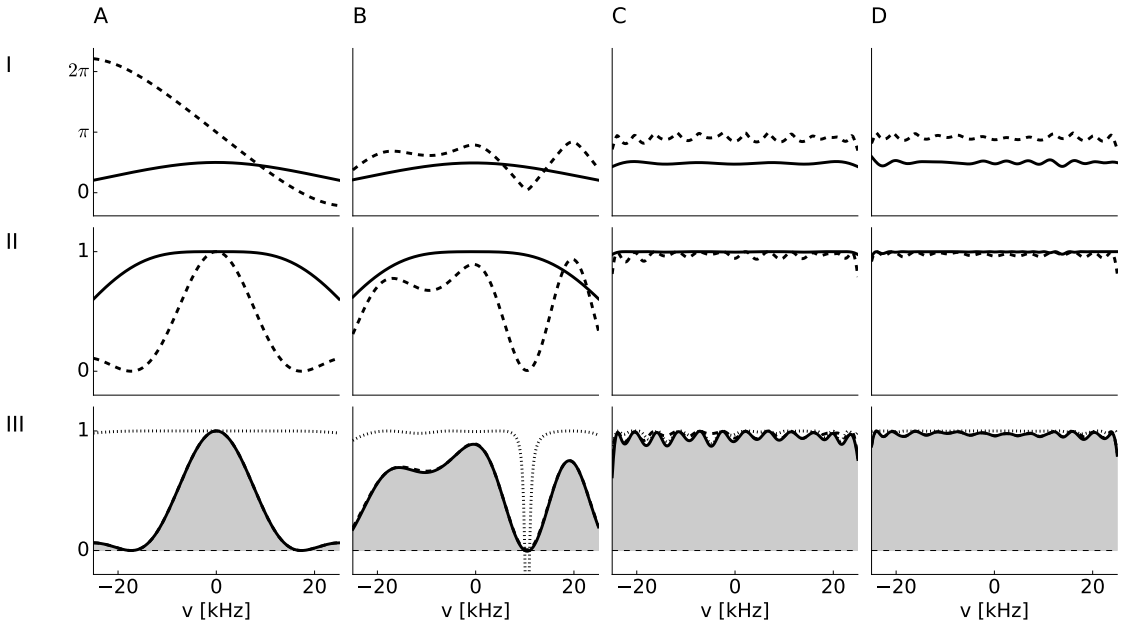

Figure 7.8: The figure shows the individual contributions to the offset-dependent local quality factor $\phi(\delta, \omega)$ (A) for a standard Hahn echo sequence composed of rectangular pulses with a total duration of 75 μs, (B) for the only slightly longer COBBLE$_{10}^{100}$ sequence shown in figure 7.21 A, (C) for an Echo sequence consisting of an individually optimized ICEBERG and BURBOP pulse with a total duration of 500 μs and (D) for an Echo sequence consisting of a COBBLE$_{100}^{500}$ sequence. In panel I, the offset-dependent flip angles $\beta^{(1)}$ for $S^{(1)}$ (solid curve) and $\beta^{(2)}$ for $S^{(2)}$ (dashed curve) are displayed. In panel II, the absolute value $|f_1| = |\sin\ \beta^{(1)}|$ (solid curve) of the transfer efficiency f_1 (c.f. Eq. 6.38) of the excitation pulse $S^{(1)}$ and the absolute value $|f_2| = |\sin^2(\beta^{(2)}/2)|$ (dashed curve) of the transfer efficiency f_2 (c.f. Eq. 6.41) of the refocusing pulse $S^{(2)}$ are shown. In panel III, the absolute value of the overall transfer efficiency $|f_1 \cdot f_2|$ (dashed line), the phase fidelity $\cos\varphi$ (dotted line) and the offset-dependent local quality factor $\phi(\delta, \omega)$ defined in Eq. (7.2) are plotted.

Figs. 7.8 and 7.9 show the individual terms contributing to the offset-dependent local quality factor $\phi(\omega)$ for echo sequences of interest. In each of these figures, the top panel depicts the offset-dependent Euler angles $\beta^{(1)}(\omega)$ (solid curve) and $\beta^{(2)}(\omega)$ (dashed curve) of the excitation and refocusing pulses, respectively. The middle panel shows the

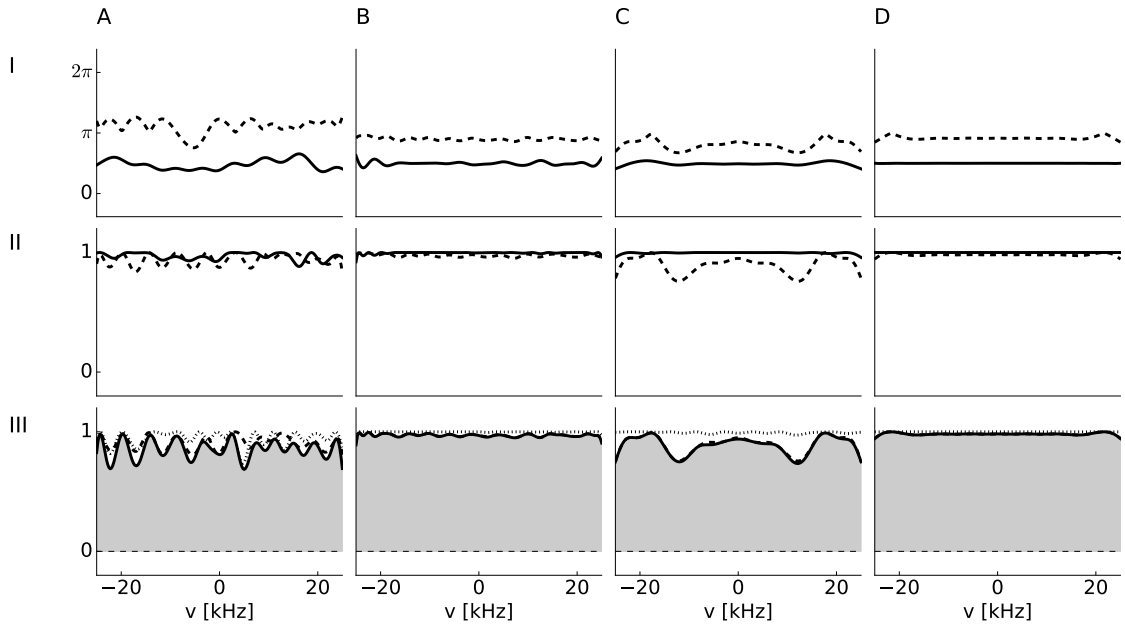

Figure 7.9: The figure shows the individual contributions to the offset-dependent local quality factor $\phi(\delta, \omega)$ (A) for an Echo sequence composed of an individually optimized BEBOP and an individually optimized BURBOP pulse, (B) for COBBLE$_0'^{500}$ sequence, (C) an Echo sequence consisting of frequency chirped pulses optimized according to the Böhlen-Bodenhausen scheme with a total duration $T^{tot} = 500$ μs and (D) an Echo sequence consituted by chirp pulses optimized according to the Böhlen-Bodenhause scheme with a total duration $T^{tot} = 1000$ μs. In panel I, the offset-dependent flip angles $\beta^{(1)}$ for $S^{(1)}$ (solid curve) and $\beta^{(2)}$ for $S^{(2)}$ (dashed curve) are displayed. In panel II, the absolute value $|f_1| = |\sin\ \beta^{(1)}|$ (solid curve) of the transfer efficiency f_1 (c.f. Eq. 6.38) of the excitation pulse $S^{(1)}$ and the absolute value $|f_2| = |\sin^2(\beta^{(2)}/2)|$ (dashed curve) of the transfer efficiency f_2 (c.f. Eq. 6.41) of the refocusing pulse $S^{(2)}$ are shown. In panel III, the absolute value of the overall transfer efficiency $|f_1 \cdot f_2|$ (dashed line), the phase fidelity $\cos\varphi$ (dotted line) and the offset-dependent local quality factor $\phi(\delta, \omega)$ defined in Eq. (7.2) are plotted.

absolute values $|f_1(\omega)| = \sin\beta^{(1)}$ (solid curve) and $|f_2(\omega)| = \sin^2(\beta^{(2)}/2)$ (dashed curve) of the partial quality factors defined in Eqs. (6.38) and (6.41). The bottom panel shows the product $|f_1(\omega)| \cdot |f_2(\omega)|$ (dashed curve), which according to Eq. (6.13) is identical to $|s(t', \omega)|$. The dotted curve represents the term $\cos\varphi(\omega)$

$$\varphi(\omega) = \omega\delta - \alpha^{(1)}(\omega) + \alpha'^{(2)}(\omega) - \pi, \tag{7.1}$$

which is the offset dependent phase of the transfer function at the auxiliary delay δ. The solid curve shows the resulting offset-dependent local quality factor, which according

Table 7.3: Global quality factors Φ of different families of optimized pulses with a total duration $T^{tot} \approx 500$ μs and of a standard echo sequence consisting of rectangular pulses with a total duration T^{tot} of 75 μs. For comparison, chirp pulses used in Böhlen-Bodenhausen-type experiments with total durations $T^{tot} = 500$ μs and $T^{tot} = 1000$ μs were added as well.

echo sequence	T^{tot} [μs]	Φ
rectangular	75	0.331
BURBOP/BURBOP	520	0.725
BEBOP/BURBOP	507.5	0.855
ICEBERG/BURBOP	500	0.944
chirp (Böhlen-Bodenhausen)	499	0.887
chirp (Böhlen-Bodenhausen)	999	0.981
COBBLE'^{500}_{0}	500	0.969
$\text{COBBLE}'^{500}_{100}$	500	0.970
COBBLE^{500}_{0}	500	0.978
COBBLE^{500}_{50}	500	0.979

to Eq. (7.2) is given by

$$\begin{aligned} \phi(\omega) &= \text{Re}\{\ |s(t',\omega)|\ \exp(i\varphi(\omega))\ \} \\ &= |s(t',\omega)|\ \cos(\varphi(\omega)). \end{aligned} \tag{7.2}$$

The corresponding total quality factors Φ are listed in Table 7.3. Fig. 7.8 A shows the offset-dependent quality factor and its individual contributions for the standard echo sequence based on rectangular pulses. Note that the grey area in Fig. 7.8 III represents the global quality factor Φ.

During a rectangular echo, spins experience a non-zero auxiliary echo delay of $\delta = 2T^{(1)}/\pi = 15.9$ μs for small offsets, whereas for the rectangular 180° pulse the auxiliary delay approaches the value of the ideal refocusing pulse.

Fig. 7.8 B corresponds to the COBBLE^{100}_{10} sequence shown in Fig. 7.21 A. Closer inspection reveals (c.f. Fig. 7.10) that the phase front of the COBBLE^{100}_{10} sequence switches at an offset of ≈10 kHz from the branch $n = 1$ to the branch $n = 0$ (c.f. Eq. 6.55). At this point, $\beta^{(2)}(\omega)$, the phase fidelity and the overall fidelity $\phi(\omega)$ degrade.

Fig. 7.8 C shows the performance of the best combination of individually optimized ICEBERG[8] and BURBOP[73] pulses (c.f. section 6.2.4) that was found for a total duration of 500 μs and an auxiliary delay $\delta = 56$ μs, where the duration of the ICEBERG pulse is $T^{(1)} = 80$ μs and the duration of the BURBOP pulse is $T^{(2)} = 420$ μs. Fig. 7.8 D shows the performance of the $\text{COBBLE}'^{500}_{100}$ echo sequence with individual durations of the excitation and refocusing pulses of $T^{(1)} = T^{(2)} = 250$ μs.

Fig. 7.9 shows the offset-dependent quality factor and its individual contributions for echo sequences with a total pulse duration of 500 μs and vanishing auxiliary delay ($\delta = 0$). Fig. 7.9 A corresponds to the best combination of individually optimized

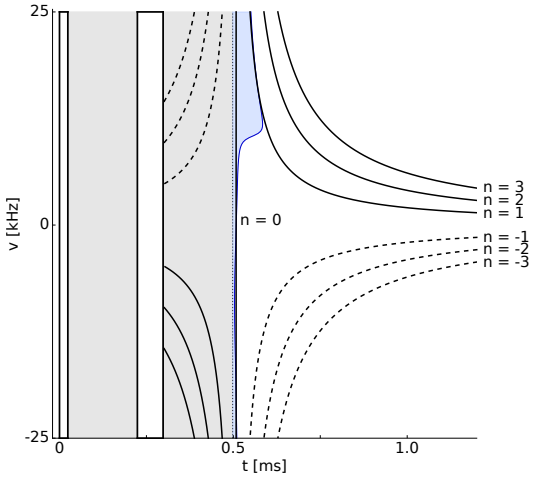

Figure 7.10: Typ IV (c.f. section 2.2) graphical representation of the effective evolution periods for a COBBLE$_{10}^{100}$ sequence. The solid black lines correspond to different branches τ_n (c.f. Eq. 6.55) with $n \in \{0, 1, 2, 3\}$. The dashed black lines correspond to τ_n with $n \in \{-1, -2, -3\}$.

BEBOP [62] and BURBOP [73] pulses (c.f. section 6.2.4) with $T^{(1)} = 177.5$ μs and $T^{(2)} = 330$ μs. Fig. 7.9 B corresponds to the best COBBLE$_0'^{500}$ sequence with $T^{(1)} = 250$ μs and $T^{(2)} = 250$ μs.

Here we also provide corresponding figures for combinations of frequency swept echo sequences based on the Böhlen-Bodenhausen scheme with total durations of 500 μs (C) and 1000 μs (D).

The conventional echo sequence based on simple rectangular 90° and 180° pulses has a relatively low total figure of merit of only $\Phi = 0.33$. The analysis of the corresponding offset-dependent quality factor $\phi(\omega)$ and of its contributions presented in Fig. 7.8 B shows that the main reason for the poor performance is the limited bandwidth of the refocusing pulse, for which the full width at half maximum of $|f_2(\omega)| = \sin^2(\beta^{(2)}/2)$ is only about 16 kHz and hence only covers a small fraction of the desired bandwidth of 50 kHz.

As discussed above, for the COBBLE$_{10}^{100}$ sequence shown in Fig. 7.21 A the excitation pulse closely approaches a rectangular 90° pulse. Nevertheless, compared to the conventional echo sequence, where both pulses are rectangular, the overall figure of merit is increased by about 65% to $\Phi = 0.54$ when replacing the rectangular refocusing pulse of duration $T^{(2)} = 50$ μs by a phase-modulated pulse with duration $T^{(2)} = 75$ μs. As shown in Fig. 7.8 A, this gain is due to the fact that $\beta^{(2)}(\nu)$ is closer to the ideal value of π over the optimized range of offsets. It is also interesting to note that even in the range 12 kHz $< \nu <$ 25 kHz, the term $\cos\varphi(\nu)$ (dotted curve in the third panel) closely approaches 1, although the blue curve in panel IV of Fig. 7.5 and 7.10 (representing the auxiliary delay τ_0 in which the phase is identical for all offsets) shows large deviations from the time δ where the maximum of the echo is found. This is a result of the fact that a constant

auxiliary delay $\tau_\alpha''^{(2)}$ (and hence constant τ_0) is a sufficient but not a necessary condition to achieve a constant signal phase over a given range of offsets. This is also the case if $\tau_\alpha''^{(2)}(\nu)$ has the form $\delta + n/\nu$, where n is an arbitary integer. As shown in Fig. 7.10, in the range -25 kHz$< \nu < 10$ kHz, the function $\tau_\alpha''^{(2)}(\nu) \approx \delta$ (corresponding to the regular case with $n = 0$), whereas in the range 12 kHz $< \nu <$ 25 kHz, $\tau_\alpha''^{(2)}(\nu) \approx \delta + 1/\nu$ (corresponding to the case $n = 1$). For offsets in the transition region between different values of n, condition (6.13) cannot be fulfilled, resulting in a reduced quality factor.

The COBBLE$'^{500}_{100}$ sequence has an excellent global quality factor of $\Phi = 0.97$ (c.f. Fig. 7.8 D) and only a 0.05% reduced quality factor for $\delta = 0$ μs. This quality factor is significantly larger than the quality factor for the optimal ICEBERG-BURBOP ($\Phi = 0.94$) and BEBOP-BURBOP ($\Phi = 0.86$) combinations for $T^{tot} = 500$ μs. For the same total pulse duration, optimized combinations of frequency-chirped pulses achieve a quality factor of $\Phi = 0.89$ and for $T^{tot} = 1$ ms a quality factor of $\Phi = 0.98$ is achieved, c.f. Fig. 7.9 C and D.

7.1.7 Experimental results

Optimized pulse sequences were tested on a Bruker Avance spectrometer with SGU units for rf control and linearized amplifiers. A sample of 0.1% H_2O in D_2O, doped with $CuSO_4$, was placed in a Shigemi limited volume tube, mitigating effects of B_1-inhomogeneities. The maximum rf amplitude (10 kHz) of the optimized pulses was calibrated using a shaped rectangular pulse of the same rf amplitude. The offset frequency of the water signal was changed from scan to scan by stepping the irradiation frequency of the pulses. An EXORCYCLE was applied to detect only single quantum coherence for which the sign of the coherence order was inverted by the refocusing pulse.

Figure 7.11 depicts simulated (A) and measured (A′) spectra of rectangular pulses with $T^{(1)} = 25$ μs and $T^{(2)} = 50$ μs, an individually optimized ICEBERG pulse (B and B′ respectively) with a duration $T^{(1)}$ of 80 μs and $\delta = 56$ μs, combined with a BURBOP puls with $T^{(2)} = 420$ μs as well as a COBBLE$'^{500}_{100}$ echo (C and C′ respectively) with $T^{(1)} = T^{(2)} = 250$ μs. Figure 7.12 shows simulated and measured spectra of Hahn echoes consisting of an individually optimized BEBOP pulse (A and A′) with $T^{(1)} = 177.5$ μs and a BURBOP pulse with $T^{(2)} = 330$ μs as well as a COBBLE$'^{500}_{0}$ sequence (C and C′) with $T^{(1)} = T^{(2)} = 250$ μs. A reasonable match is found between measured and simulated spectra. An almost uniform excitation over the considered frequency range was achieved by the COOP pulses. Although the improvement of the global quality factor (corresponding to the maximum echo amplitude) from $\Phi = 0.86$ for the BEBOP-BURBOP sequence to $\Phi = 0.97$ for the COOP echo sequence is relatively small, this results in sigificantly reduced offset-dependent phase errors.

Figure 7.13 B shows experimentally measured echo traces. These were obtained by performing Hahn echo experiments in the presence of a constant B_0 field gradient which created an inhomogeneously broadened linewidth $>$ 50 kHz. The gradient was only switched off during the relaxation delay between different scans. In each experiment 256 scans were acquired and a reasonable match between simulated (fig.7.13 A) and

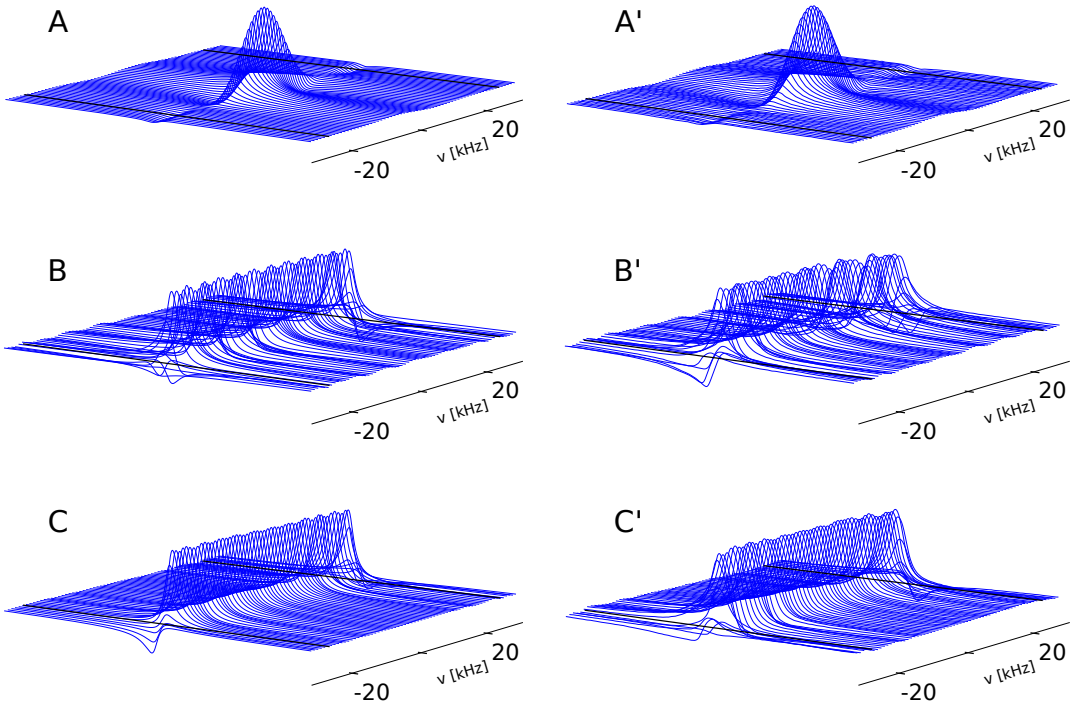

Figure 7.11: Simulated and measured spectra (primed) of a Hahn Echo experiment with an auxiliary delay $\delta \neq 0$ using rectangular (A and A′), individually optimized ICEBERG and BURBOP (B and B′) pulses and a COBBLE$'^{500}_{100}$ sequence (C and C′). Each panel shows stacked plots of 1D spectra, where the irradiation frequency is varied in equidistant steps between −30 kHz and 30 kHz. The total pulse duration T^{tot} for the shaped pulses is 500 μs. The limits of the optimized offset range of ±25 kHz are depicted by black lines.

experimental positions, amplitudes, and shapes of the echoes was found.

7.1.8 B_1 inhomogeneities

The COOP echo sequences discussed in 7.1.6 were optimized without explicitly taking rf inhomogeneity effects into account. Figs. 7.14 to 7.15 show the effect of both offset and and a scaling of the rf amplitude. The simulations were performed for an offset range of ±35 kHz and the white dashed lines indicate the offset range of ±25 kHz for which the sequences were optimized. A scaling of the B_1 amplitude between 70% and 130% relative to the nominal amplitude B_1^{nom} of 10 kHz was considered. The color of each point indicates the phase of the magnetization at the time of the echo and the brightness of each point reflects the magnitude of the magnetization.

Figure 7.14 shows the performance of Hahn echo sequences with an auxiliary delay $\delta \neq 0$. Subfigure A depicts the performance of a Hahn echo experiment based on rect-

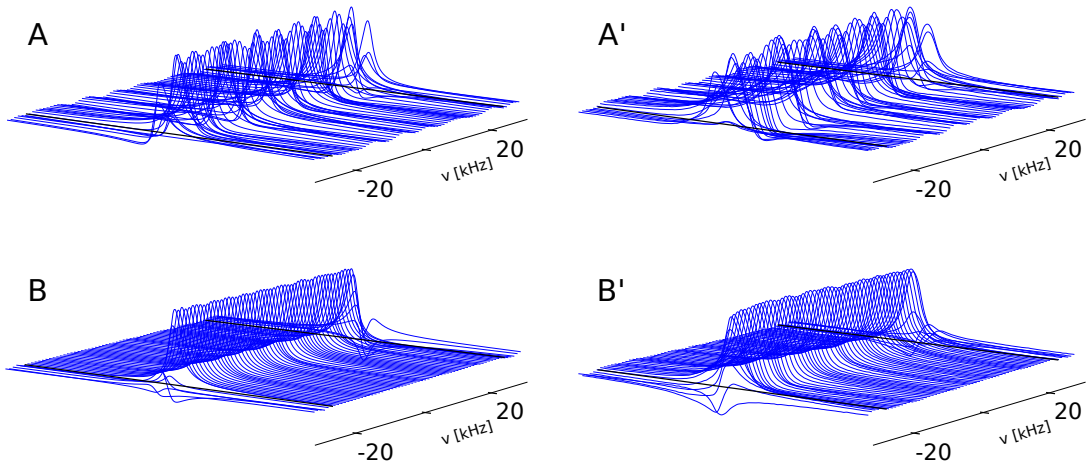

Figure 7.12: Simulated and measured (primed) spectra of a Hahn Echo experiment with with an auxiliary delay $\delta = 0$, using individually optimized BEBOP and BURBOP (A and A′) pulses and a COBBLE$_0^{\prime 500}$ sequence (B and B′). Each panel shows stacked plots of 1D spectra, where the irradiation frequency is varied in equidistant steps between −30 kHz and 30 kHz. The total pulse duration T^{tot} for the shaped pulses is 500 μs. The limits of the optimized offset range of ±25 kHz are depicted by black lines.

angular pulses. We observe a limited FWHM (full width at half maximum) bandwidth of 16 kHz. Varying B_1 scaling has little impact on phase alignment and bandwidth. Subfigure B depicts the performance of the cooperatively optimized COBBLE$_{10}^{100}$ sequence with a bandwidth of ±25 kHz which is only 33% longer than the rectangular Hahn echo with a total duration $T^{tot} = 75$ μs. The phase at echo time is independent of B_1, but the pulse covers a larger bandwidth than the rectangular pulse. For small B_1 fields, the achievable amplitude decreases stronger compared to a rectangular pulse. Figure C shows simulations for a Hahn echo sequence comprised of an ICEBERG pulse with $T^{(1)} = 80$ μs, a BURBOP refocusing pulse with a duration of 420 μs and an auxiliary $\delta = 56$ μs. Some phase distortions occur in the optimized region, which is in agreement with our findings in section 7.1.7. The sequence tolerates stronger rf fields it was optimized for, but not weaker ones.

Figure D shows data for a COBBLE$_{100}^{\prime 500}$ sequence. The sequence tolerates stronger B_1 fields than the ones it was optimized for, but not substantially weaker ones. In agreement with our findings in section 7.1.7, it shows less phase dispersion in the optimized range compared to the individually optimized sequence analyzed in figure 7.14 B I.

Figure 7.15 shows the performance of Hahn echo sequences with an auxiliary delay $\delta = 0$ and chirped pulses. Subfigure A depicts the performance of a Hahn echo which consists of an individually optimized BEBOP excitation and BURBOP refocusing pulse with a total duration $T^{tot} = 507.5$ μs. In agreement with our findings in 7.1.7 the sequence shows some phase distortions in the optimized range. In addition, rf scaling

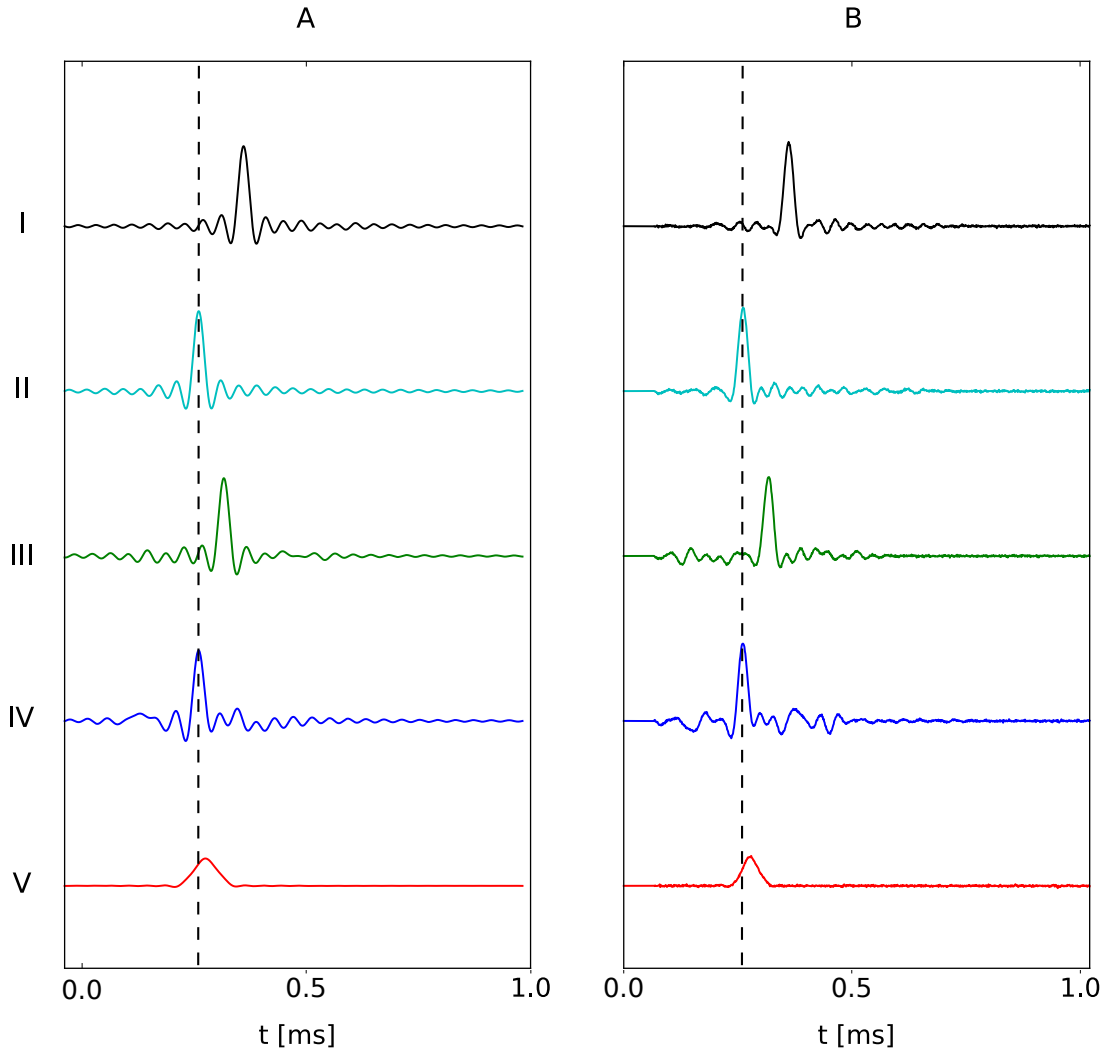

Figure 7.13: Simulated (A) and measured (B) echo envelopes of a COBBLE$_0'^{500}$ (I) and a COBBLE$_0'^{500}$ sequence (II), an individually optimized ICEBERG pulse combined with an individually optimized BURBOP pulse (III), an individually optimized BEBOP pulse combined with an individually optimized BURBOP pulse (IV) and a rectangular pulse (V).

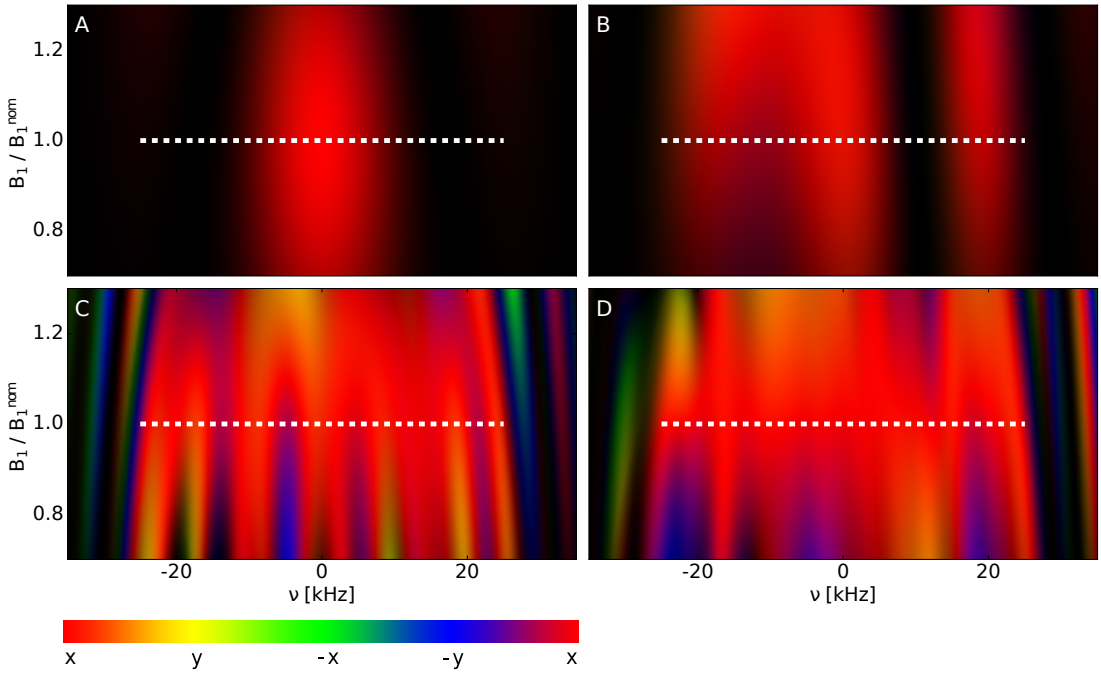

Figure 7.14: Amplitude (brightness) and phase (the color map is shown at the bottom) of a Hahn echo as a function of offset and B_1 scaling for a sequence of rectangular pulses (A), a COBBLE$_{10}^{100}$ sequence (B), individually optimized ICEBERG and BURBOP pulses with a total duration $T^{tot} = 500$ μs and an internal evolution $\delta = 54$ μs (C), and a COBBLE$_{100}^{\prime 500}$ sequence (D). The pulses were only optimized to be robust with respect to offsets. The optimized region is depicted as a dashed white line.

creates further phase errors. In comparison, subfigure B depicts the performance of a COBBLE$_0^{\prime 500}$ sequence. In agreement with our findings in section 7.1.7, the sequence shows little to no phase dispersion over the optimized range. Figure 7.15 shows the performance of WURST pulses optimized according to the Böhlen-Bodenhausen scheme [49] with a total duration $T^{tot} = 500$ μs (C) and $T^{tot} = 1000$ μs (D). They are broadband, but do not tolerate strong B_1 inhomogeneities, which is in agreement with our findings in figure 7.15 C and D. Cano et al. suggested a three-pulse chirp sequence that is both broadband and B_1 robust, however, a third pulse has to be introduced which prolongs the sequence and partly offsets the gains obtained by using robust pulses.

Figs. 7.14 C and 7.15 B indicate that COBBLE sequences are robust to variations of the rf amplitude in the range of about $\pm 10\%$. For applications in which a larger robustness with respect to rf scaling is required, it is possible to explicitly include this robustness in the optimization as described in. [59,155] Based on results for individually optimized pulses, [62,73,108,155] it is expected that the same total figure of merit can be achieved for pulses with increased robustness with respect to rf scaling if the pulse duration is increased.

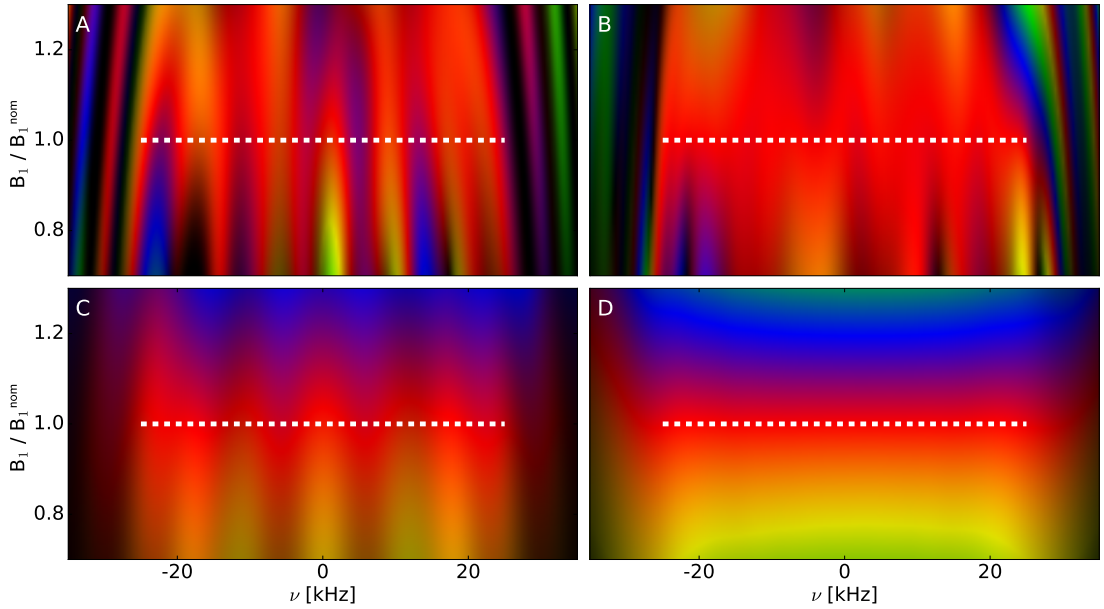

Figure 7.15: Amplitude (brightness) and phase (see color map in Fig. 7.14) of a Hahn echo as a function of offset and B_1 scaling for a sequence of individually optimized BEBOP and BURBOP pulses with a total duration $T^{tot} = 507.5$ μs (A), a COBBLE$_0^{500}$ sequence (B), individually optimized ICEBERG and BURBOP pulses with a total duration $T^{tot} = 500$ μs and an internal evolution $\delta = 54$ μs (C) and sequences of WURST pulses optimized according to the Böhlen-Bodenhausen scheme[38] with a total duration $T^{tot} = 500$ μs (C) and 1000 μs (D). The pulses were only optimized to be robust with respect to offsets. The optimized region is depicted as a dashed white line.

We optimized COBBLE pulse sequences with the same durations of the excitation pulse $T^{(1)}$ and of the refocusing pulse $T^{(2)}$ and the same auxiliary delay δ that proved optimal without considering B_1 inhomogeneity, this time taking into account $\pm 7.5\%$ and $\pm 20\%$ field inhomogeneity. Results are depicted in figure 7.16. As expected, when B_1 inhomogeneity is considered in the optimization procedure, T^{tot} has to be increased to achieve the same fidelity compared to optimizations that do not account for B_1 inhomogeneity.

In figure 7.17, we compare pulse sequences with different levels of B_1 inhomogeneity compensation. As previously established, if sequences of the same total pulse duration T^{tot} were chosen, fidelities would vary. In order to demonstrate B_1 compensation, we choose pulse sequences with the same overall fidelity. A depicts a COBBLE$_{40}^{400}$ echo without B_1 compensation. B depicts the effect of a COBBLE$_{60}^{600}$ echo with a B_1 compensation of 40% B_1. The B_1 robust sequence achieves a near uniform phase and amplitude within the considered frequency and B_1 range.

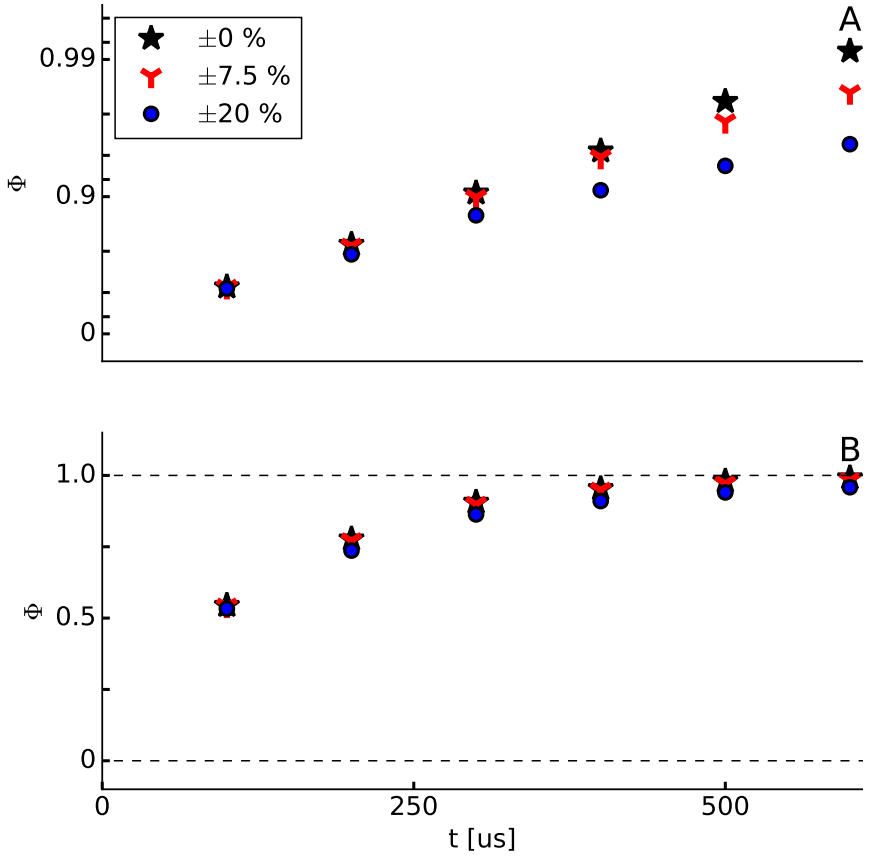

Figure 7.16: TOP (time-optimal pulse) curves for cooperative pulses in the absence and presence of B_1 inhomogeneities. We assumed an equal weighting of B_1 scaling factors within the optimized range. The same data are shown for a logarithmic (top panel) and a linear (bottom pannel) scale of the figure of merit Φ.

7.1.9 Couplings

In section 6.2.6 we presented a treatment of spin systems in the presence of couplings and distinguished between weak or Ising coupling, couplings including pseudosecular terms and possibly off-resonant I spins.

A COBBLE$_0^{\prime 800}$ sequence was optimized and a weak coupling contribution of 30 kHz included into the Hamiltonian (henceforth we call this sequence COBBLE-2S$_0^{\prime 800}$). The performance of this sequence was compared to a COBBLE$_0^{\prime 800}$ that was not tuned to be robust towards Ising coupling. Results are depicted in Fig. 7.18.

Fig. 7.18 A shows the x-component of the magnetization vector after a Hahn echo experiment using an EXORCYCLE in the absence of Ising coupling using the COBBLE$_0^{\prime 800}$ sequence and 7.18 B using the COBBLE-2S$_0^{\prime 800}$ sequence. In both cases we observe that magnetization is approximately aligned along the x-axis. However, the overall figure of

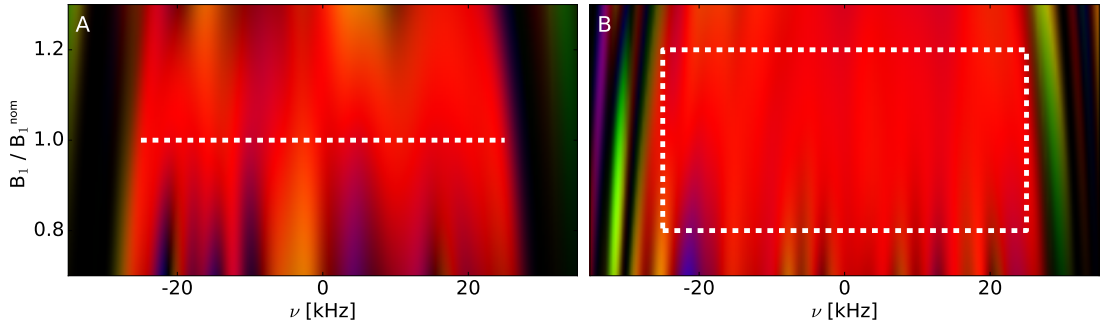

Figure 7.17: Amplitude (brightness) and phase (see color map in Fig. 7.14) of a Hahn echo as a function of offset and B_1 scaling for a COBBLE$_{40}^{400}$ sequence (A) and a COBBLE$_{60}^{600}$ sequence (B). The pulses were optimized to be robust with respect to offsets (A and B) and ±20% field inhomogeneity (B only). The optimized region is marked by a dashed white line.

merit $\Phi = 0.99$ of the COBBLE$_0'^{800}$ sequence exceeds the one of the COBBLE-2S$_0'^{800}$ sequence ($\Phi = 0.97$). The larger figure of merit corresponds to a more uniform phase distribution and a larger echo amplitude.

Fig. 7.18 C depicts the x-component of the magnetization vector after a Hahn echo experiment using an EXORCYCLE in the presence of 30 kHz Ising coupling using the COBBLE$_0'^{800}$ sequence and 7.18 D using the COBBLE-2S$_0'^{800}$ sequence. Here the COBBLE$_0'^{800}$ sequence generates a linear phase distribution in the offset range minus the coupling constant, i.e. in a range of 20 kHz with a total figure of merit $\Phi = 0.74$. The COBBLE-2S$'_{800}$0 sequence on the other hand generates approximately uniform magnetization with a total figure of merit $\Phi = 0.97$.

In Fig. 7.19 x-magnetization after a Hahn echo experiment with an EXORCYCLE in the absence of Ising coupling is shown for an offset range ±65 kHz. The COBBLE-2S$_0'^{800}$ sequences employed here were optimized for an offset range of ±25 kHz in the presence of (A) 0 kHz, (B) 30 kHz and (C) 60 kHz Ising coupling.

The sequences achieve near uniform phase distributions and echo amplitudes close to the maximum in an offset range of $J/2 \pm 25$ kHz and $-J/2 \pm 25$ kHz, i.e. in case (A) at ±25 kHz, for (B) at ±40 kHz and for (C) between −55 and −5 kHz and between 5 and 55 kHz. For the offset range between -5 and 5 kHz, the target state is undefined. Correspondingly, magnetization is not aligned along the x-axis here.

Fig. 7.20 displays the overall figure of merit Φ over an offset range of ±25 kHz for a COBBLE-2S$_0'^{800}$ sequence optimzed for 30 kHz weak coupling as a function of secular (x-axis) and pseudosecular (y-axis) coupling contributions with an I-spin offset of 0 kHz (A), 100 Hz off-resonant (B), 1 kHz off-resonant (C) and 10 kHz. In case of an on-resonant I-spin, sequences that compensate Ising coupling tolerate pseudo-secular contributions in the Hamiltonian as well.

In section 6.2.6 an expression for the coupling hamiltonian was introduced (Eq. 6.58)

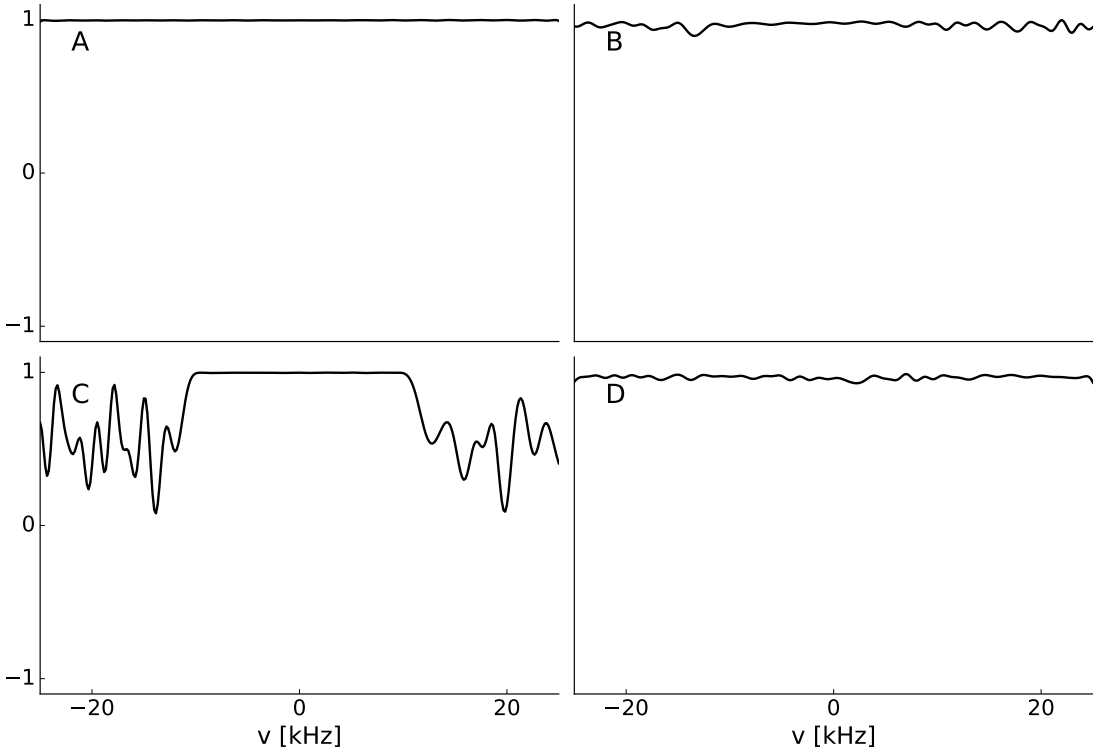

Figure 7.18: Here simulations of x-magnetization are depicted for an offset range ± 25 kHz after a Hahn echo experiment using an EXORCYCLE. (A) and (B) correspond to dynamics without coupling, (C) and (D) to dynamics which include a 30 kHz Ising coupling constant. The COBBLE$_0'^{800}$ sequence used in case (A) and (C) was not explicitly optimized to tolerate couplings, the COBBLE$_0'^{800}$ sequence employed in (B) and (D) was optimized including 30 kHz Ising coupling.

$$\mathcal{H}_{\text{coupling}} = 2\pi J \cdot I_z S_z + 2\pi J^x_{\text{pseudosecular}} I_x S_z + 2\pi J^y_{\text{pseudosecular}} I_y S_z.$$

which can be simplified to

$$\mathcal{H}_{\text{coupling}} = 2\pi J \cdot I_z S_z + 2\pi J'^x_{\text{pseudosecular}} I_x S_z \tag{7.3}$$

in a proper rotating frame of reference. COBBLE-2S sequences tolerate average coupling J_{av} of

$$J_{\text{av}} = \sqrt{J^2 + (J^x_{\text{pseudosecular}})^2}. \tag{7.4}$$

We suggest that in the case of Ising coupling, i.e. in case the coupling contribution is described by the operator $I_z S_z$, including couplings into the optimization procedure is equivalent to increasing the adopted offset range by the coupling constant, assuming a

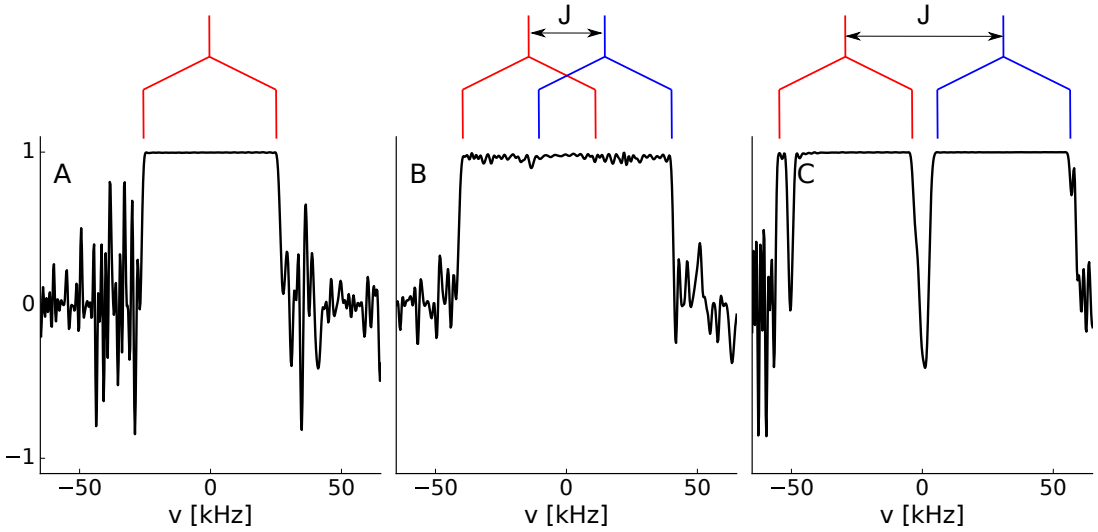

Figure 7.19: Here we show x-magnetization over an offset range of ± 65 kHz after a COBBLE$'^{800}_0$ sequence that was optimized for (A) 0 kHz Ising coupling, (B) 30 kHz Ising coupling and (C) 60 kHz Ising coupling. Simulations were conducted without considering couplings.

range of couplings between 0 and the desired J scaling are to be tolerated. In case that a single coupling strength is supposed to be compensated, it is sufficient to consider the two offset domains $\nu + J/2$ and $\nu - J/2$ (c.f. Fig. 7.19).

Resonance frequencies larger than 100 Hz of the I-spin have no impact in the presence of Ising coupling alone (which is attributable to the fact that the corresponding operator commutes with both the initial density matrix and the Hamiltonian). If pseudosecular terms have to be considered, the overall figure of merit Φ is decreased significantly.

The optimizations here were carried out for application in EPR systems with hyperfine couplings. There in many cases the external B_0 field is weak enough, that the offset of the nucleus is small compared to the resonance frequency of the electron and the hyperfine coupling strength. Thus the optimizations conducted here should be applicable.

7.1.10 Pulseshapes

Fig. 7.21 shows amplitude and (colorcoded) phase for the best COBBLE sequences as a function of total pulse duration for $T^{tot} = 100$ μs I (A), $T^{tot} = 200$ μs I (B), $T^{tot} = 300$ μs I (C), $T^{tot} = 400$ μs I (D), $T^{tot} = 500$ μs I (E) and $T^{tot} = 600$ μs I (F).

It is interesting to note that for $T^{tot} = 100$ μs, the excitation pulse of the best COBBLE sequence converged to a simple rectangular 90° pulse with a duration $T^{(1)} = 25$ μs and approximately constant phase. The phase of the refocusing pulse of duration $T^{(2)} = 75$ μs is strongly modulated, resulting in $\beta^{(2)}(\nu)$ angles closer to the ideal value of π over the optimized range of offsets.

Figure 7.21 II shows the starting pulse and the pulse shape obtained after 1500 pre-

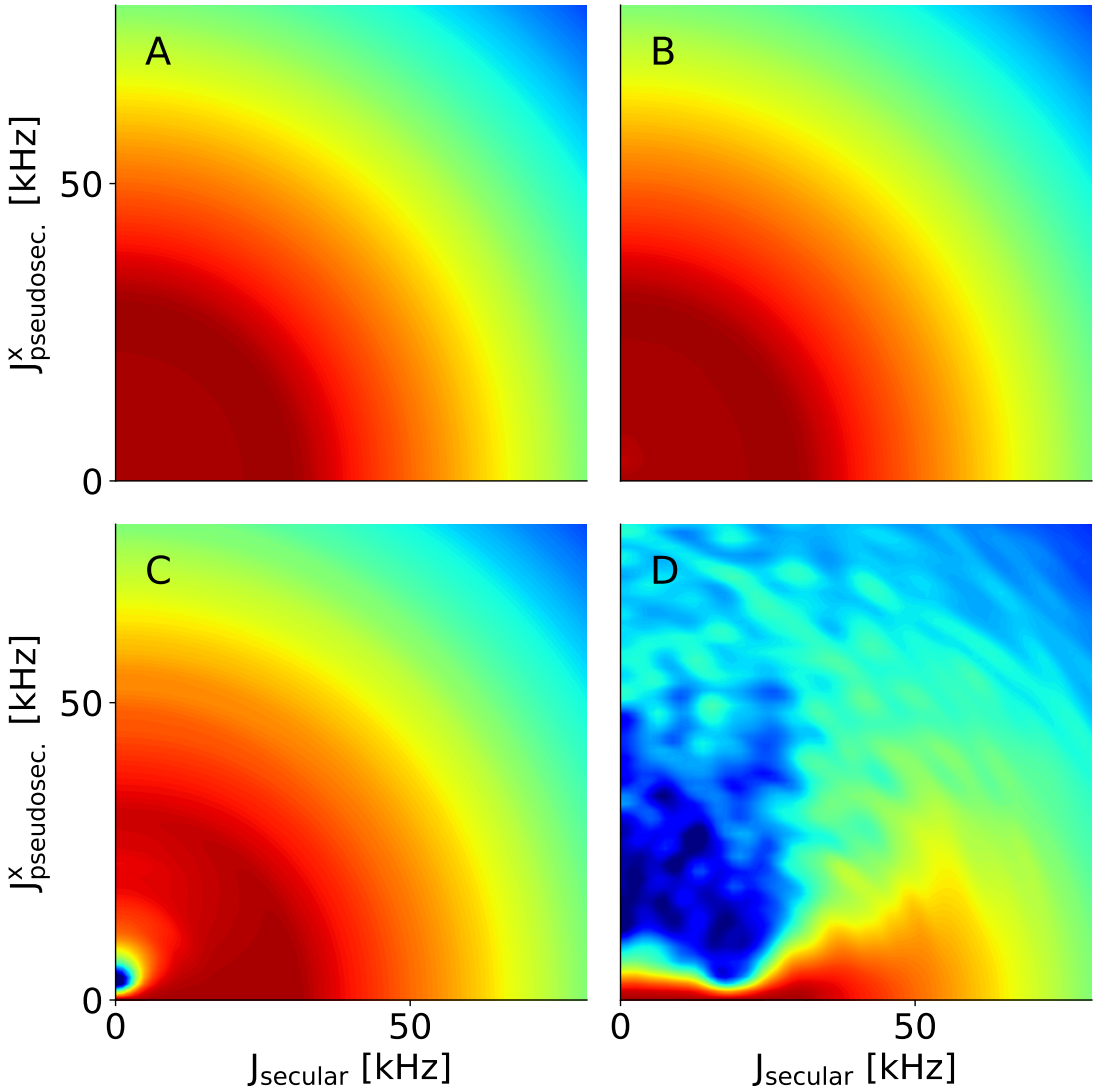

Figure 7.20: Here we show the fidelity of a COBBLE$_0^{\ell 800}$ sequence that was optimized for 30 kHz Ising coupling over an offset range for the S spin in the presence Ising and pseudosecular coupling and (A) 0 Hz, (B) 100 Hz, (C) 1 kHz and (D) 1000 kHz offset of the I spin. The dark blue color corresponds to a fidelity $\Phi = 0$, the dark red color to $\Phi = 1$.

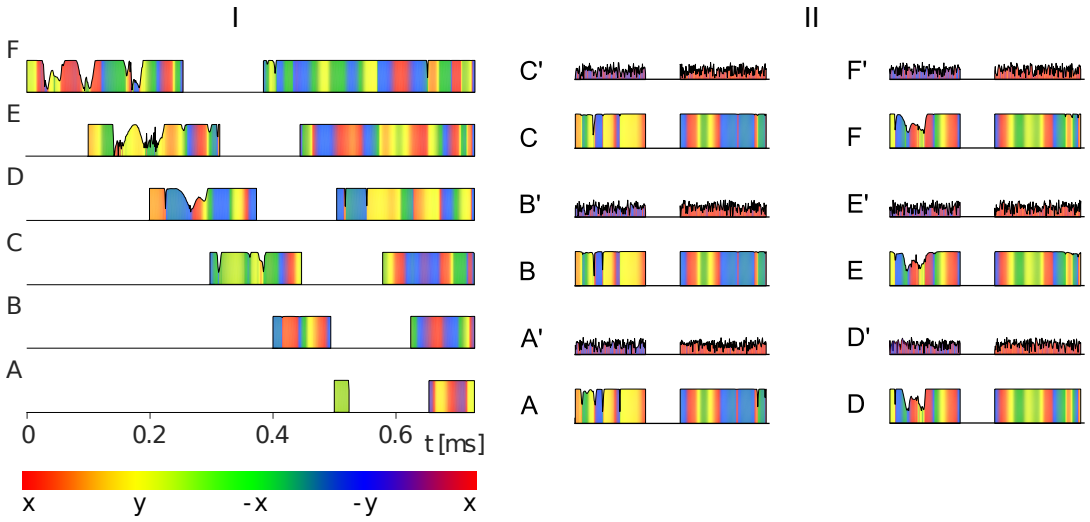

Figure 7.21: Subplot I depicts excitation and refocusing pulses of COBBLE sequences for $T^{tot} = T^{(1)} + T^{(2)}$ of (A) 100 μs, (B) 200 μs, (C) 300 μs, (D) 400 μs, (E) 500 μs, and (F) 600 μs. An arbitrary inter-pulse delay $\tau^{(1,2)}$ of 100 μs was inserted between the pulses in order to clearly separate them. The maximum rf amplitude was 10 kHz and the pulse phase is color coded (x: red, y: yellow, $-$x: green, $-$y: blue). The colormap is shown below the pulse shapes. Subplot II shows phase and amplitude of starting shapes (A$'$, B$'$, C$'$, D$'$, E$'$ and F$'$) and for the optimization and final shapes (A, B, C, D, E and F).

optimization and 1500 final optimizations iterations for selected COBBLE$_0^{300}$ sequences (subplots A, B, C, D, E and F) with a duration $T^{(1)} = 135$ μs and $T^{(2)} = 165$ μs for different random starting positions (A$'$, B$'$, C$'$, D$'$, E$'$ and F$'$). (Unwrapped) phases of the refocusing pulses were shifted to an average of 0. The starting shapes A$'$, B$'$ and C$'$ converged to highly similar final shapes, likewise the starting shapes presented in subfigure D$'$, E$'$ and F$'$. This is in agreement with our findings in section 7.1.2. Note that Fig. 7.21 II does not provide a comprehensive representation of all found pulse shapes. More solutions exist, however an extensive study of various pulse shapes is beyond the scope of the thesis at hand and currently conducted elsewhere.[156]

7.1.11 Spectrogram representation of cooperative Hahn echoes

Amplitude and phase representation of pulse shapes obtained by GRAPE optimization are highly modulated and rarely intuitively interpretable. Köcher et al. studied the representation of shaped pulses by a joint time-frequency representation through a short-time Fourier transform,[9] which provides time-resolved insight into the actions of a pulse.

Here we analyze a COBBLE$_{60}^{600}$ sequence optimized for an offset range of $\pm$25 kHz by such a representation (Fig. 7.22). The first pulse $S^{(1)}$ has a duration $T^{(1)} = 255$ μs, the

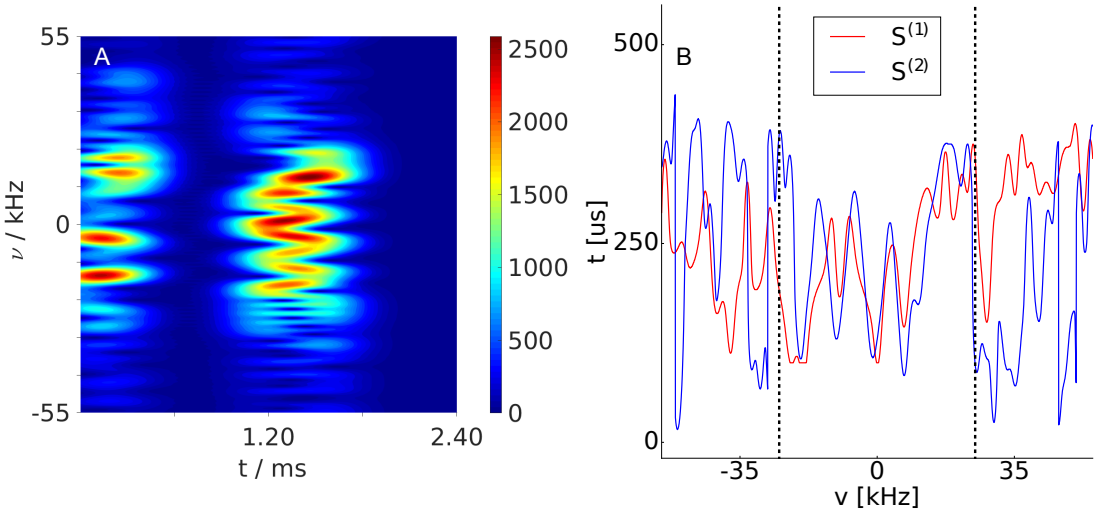

Figure 7.22: Spectrogram representation of a COBBLE$^{600}_{60}$ sequence optimized for a bandwidth ±25 kHz, with an interpulse delay $\tau^{(1,2)} = 600$ μs and a final delay with a duration of 600 μs (A). (B) shows the position of the maxima extracted from the spectrogram of the $S^{(1)}$ pulse (red curve) and of the $S^{(2)}$ pulse (blue curve) in the time dimension as a function of the frequency. The dashed curves represent the boundaries of the optimized region.

second pulse $S^{(2)}$ has a duration $T^{(2)} = 345$ μs. A delay of 600 μs was inserted before and after the second pulse to clearly separate it in the spectrogram representation. The spectrogram was computed for a frequency range of ±55 kHz with a frequency resolution of 55 Hz and a Gaussian window with a FWHM of 300 μs.

The pulse depicted in Fig. 7.22 A contains frequency components outside the optimized range. However, the amplitude of the spectrogram representation within the optimized range is significantly more pronounced. The position of the maxima in the spectrogram of $S^{(1)}$ pulse and the $S^{(2)}$ pulse (Fig. 7.22 B) are similar to an extent, albeit not an exact match.The exact reason for this might be subject of future investigations.

7.2 $\frac{\pi}{2} - \pi - \frac{\pi}{2}$ sequences

7.2.1 Nomenclature

In section 7.1.1 we defined a nomenclature for cooperatively optimized Hahn echo sequences. The acronym COBBLE^m_n was introduced to denote cooperatively optimized Hahn echo sequences, where the superscript m reflected the overall pulse duration m in μs and the subscript n the corresponding effective delay δ.

Henceforth $\frac{\pi}{2} - \pi - \frac{\pi}{2}$ sequences are referred to as COBBLE3^m_n sequences, the meaning of the subscript and the superscript is identical to Hahn echo sequences.

7.2.2 Optimization strategies

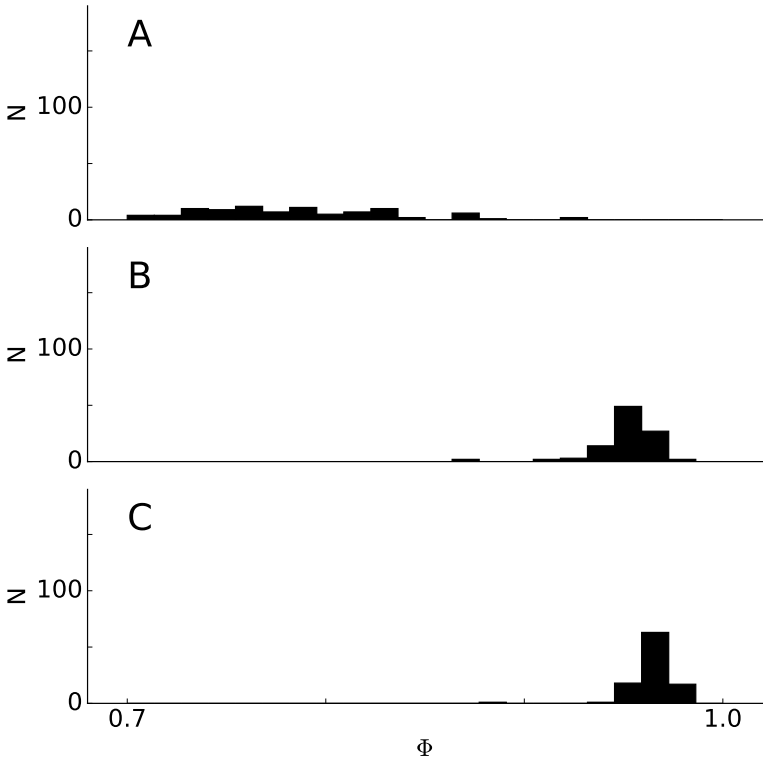

Figure 7.23: Histograms of the achieved figure of merits Φ for 100 optimized $\frac{\pi}{2} - \pi - \frac{\pi}{2}$ sequences starting with random $S^{(1)}$, $S^{(2)}$ and $S^{(3)}$ pulses with durations $T^{(1)} = T^{(3)} = 140$ μs and $T^{(2)} = 320$ μs using (A) direct optimization of $\frac{\pi}{2} - \pi - \frac{\pi}{2}$ sequences based on the gradient of Φ for 3000 iterations, (B) pre-optimization of $\frac{\pi}{2} - \pi - \frac{\pi}{2}$ sequences as described in section 6.3.3 for 3000 iterations, and (C) two-step approach based on pre-optimization for 1500 iterations followed by optimizations using the gradient of Φ for 1500 iterations. N is the number of $\frac{\pi}{2} - \pi - \frac{\pi}{2}$ sequences found in each bin.

In section 7.1.2 we discussed the performance of optimization strategies for Hahn echo sequences. We presented results for COBBLE′ sequences, COBBLE sequences and COBBLE without reoptimization. For $\frac{\pi}{2} - \pi - \frac{\pi}{2}$ sequences we conduct a similar analysis here.

The optimization algorithms for $\frac{\pi}{2} - \pi - \frac{\pi}{2}$ sequences are outlined in section 4.4.3 and 6.3.3. Figure 7.23 A shows a histogram of the figures of merit Φ achieved for optimization of 100 random initial sequences without pre-optimization over 3000 iterations. The pulse sequences have a total duration $T^{tot} = 600$ μs, where $T^{(1)} = 140$ μs, $T^{(2)} = 320$ μs and $T^{(3)} = 140$ μs and $\delta = 0$. Similar to Hahn echo sequences, the algorithm is frequently trapped in local maxima, which is reflected in an approximately equal distribution of Φ ranging from 0.62 to 0.94, with an average $\overline{\Phi} = 0.77$.

When the pre-optimization algorithm presented in section 6.3.3 is used, a narrower distribution of fidelities is achieved (c.f. Fig. 7.23 B) with a minimum $\Phi = 0.53$, a maximum $\Phi = 0.95$ and an average $\overline{\Phi} = 0.94$.

The best performance distribution is obtained for pre-optimization over 1500 iterations and subsequent optimization according to the algorithm presented in section 4.4.3. Here the minimum $\Phi = 0.87$, the maximum $\Phi = 0.98$ and the average $\overline{\Phi} = 0.96$.

7.2.3 Magnetization

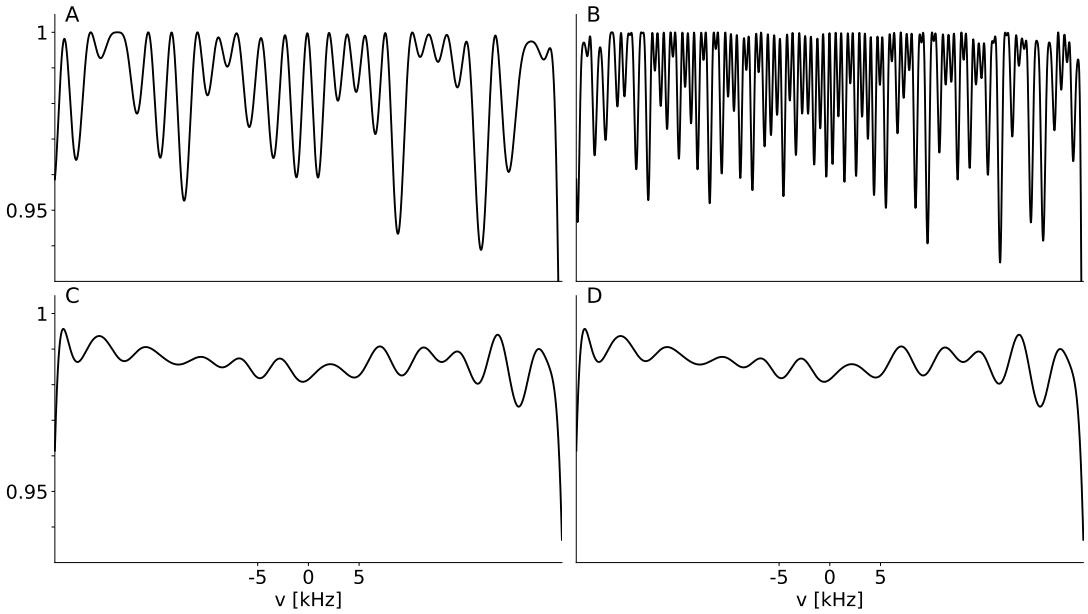

Figure 7.24: Here the offset-dependent z-component of magnetization of a COBBLE3$_0^{600}$ sequence is depicted for the optimized range of ±25 kHz. Simulation was carried out with an interpulse delay $\tau^{(1,2)} = 0$ (A and C) and $\tau^{(1,2)} = 0.6$ ms (B and C), with (C and D) and without (A and B) phase cycle.

In section 6.3.2, a transfer function for $\frac{\pi}{2} - \pi - \frac{\pi}{2}$ sequences was derived. The offset-dependent transfer function $s(\omega)$ corresponds to the offset-dependent z-magnetization after a $\frac{\pi}{2} - \pi - \frac{\pi}{2}$ experiment using the phase cycle introduced in section 6.3.1.

Figure 7.24 depicts offset-dependent z-magnetization after a $\frac{\pi}{2} - \pi - \frac{\pi}{2}$ sequence with (A and C) and without (B and D) an additional delay $\tau^{(1,2)} = \tau^{(2,3)} = 0.6$ ms. Subplot A and B show data obtained without phase cycling and C and D display z-magnetization using the phase cycle introduced in section 6.3.1.

In all cases the z-magnetization amounts between 0.94 and 1 independent of the offset. With coherence transfer pathway selection, the transfer function is independent of the interpulse delays $\tau^{(1,2)}$ and $\tau^{(2,3)}$ (c.f. Fig. 7.24 C and D) as derived in section 6.3.2. Without coherence selection, artefacts occur (c.f. Fig. 7.24): the transfer function

derived in section 6.3.2 is explicitly independent of the interpulse delays. Here we observe oscillations whose frequencies increase with the duration of $\tau^{(1,2)} = \tau^{(2,3)}$.

The findings are in agreement with the findings for COBBLE sequences presented in section 7.1.3).

7.2.4 Quality factor landscapes

Here we examine the dependency of the quality factor Φ as a function of pulse duration $T^{(1)}$, $T^{(2)}$ and $T^{(3)}$. In conventional $\frac{\pi}{2} - \pi - \frac{\pi}{2}$ sequences, the duration of the π pulse is twice as long as the duration of the two $\pi/2$ pulses. In section 7.1.4 we pointed out that this does not apply to COBBLE sequences a priori. Empirically we found an optimal ratio of 1 : 1.3. In addition, the optimal duration of the auxiliary delay is not a priori known. Here we conduct similar studies for $\frac{\pi}{2} - \pi - \frac{\pi}{2}$ sequences.

Figure 7.25 shows the figure of merit Φ as a function of $T^{(1)}$ and $T^{(2)}$ with a total duration $T^{tot} = 600$ μs. The optimal combination is indicated by a white cross. The best value of Φ was found for a COBBLE3$_0^{600}$ sequence, which we attribute to the fact that equal phase evolution α of the $S^{(1)}$ and γ of the $S^{(3)}$ add up to 0 due to the refocusing pulse. In addition, in contrast to COBBLE sequences, the highest figure of merit for COBBLE3 sequences was obtained for a ratio $T^{(1)} : T^{(2)} : T^{(3)} = 1 : 2 : 1$. This corresponds to the ratio expected for conventional rectangular pulses. Note that this is true for $\delta/T^{tot} = 0$. For $\delta/T^{tot} \neq 0$ the ratio changes, the changes are symmetric with respect to the sign of $\delta/T^{tot} = 0$. The pulse durations associated with the best quality factor lie on a flat plateau. Deviations from the ideal position have little impact on the overall fidelity.

In Fig. 7.25 the area that corresponds to minimum pulse durations $T^{(1)}_{\text{min}} = T^{(3)}_{\text{min}} = 25$ μs and $T^{(2)}_{\text{min}} = 50$ μs is indicated by a white triangle. These minimum pulse durations are required to achieve a flip angle $\beta = \pi/2$ and $\beta = \pi$. Note that the figure of merit decays most strongly with decreasing $T^{(2)}$ and least strongly with decreasing $T^{(3)}$. The asymmetry with respect to $T^{(1)}$ and $T^{(2)}$ may be of interest in future investigation.

7.2.5 Analysis of $\frac{\pi}{2} - \pi - \frac{\pi}{2}$ sequences in terms of effective evolution periods

In section 7.1.5 Hahn echo sequences were analyzed in terms of effective evolution periods. Here we perform similar analysis on $\frac{\pi}{2} - \pi - \frac{\pi}{2}$ sequences.

In Figs. 7.26 and 7.27, plots of the effective evolution periods introduced in section 6.3.5 are shown. In each of these figures, panel I depicts a pulse sequence using plot type I, where the effective evolution time $\tau_\alpha^{(1)}$ is shown at the trailing edge of the excitation pulse, $\tau_\gamma^{(2)}$ and $\tau_\alpha^{(2)}$ are shown at the leading and trailing edges of the refocusing pulse and $\tau_\gamma^{(3)}$ is shown at the leading edge of the third pulse, respectively. Panel II corresponds to plot type II, where $\tau_\alpha^{(1)}$ is unchanged, $\tau_\gamma^{\prime(2)}$ vanishes and $\tau_\alpha^{\prime(2)}$ is shown at the trailing edge of the refocusing pulse. Panel III corresponds to plot type III, where $\tau_\alpha^{\prime\prime(2)}$ is shown at the trailing edge of the refocusing pulse and $\tau_\gamma^{\prime\prime(3)}$ vanished.

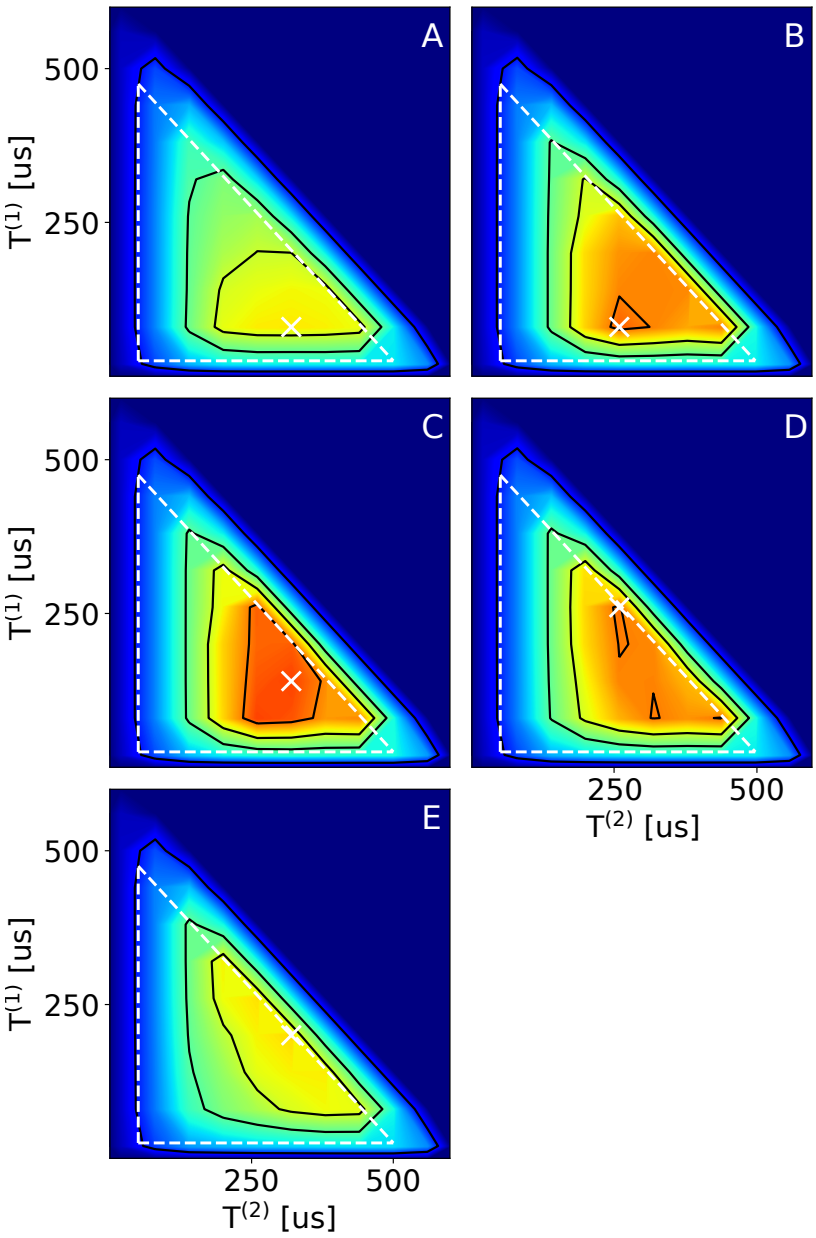

Figure 7.25: For an auxiliary delay δ/T^{tot} of (A) -0.3, (B) -0.15, (C) 0, (D) 0.15, (E) 0.3, the quality factor Φ is shown as a function of $T^{(2)}/T^{tot}$ (x axis) and $T^{(2)}/T^{tot}$ (y axis). A white cross indicates the location of the best quality factor for each δ/T^{tot}. Black contour lines are plotted at Φ levels 0.5, 0.9, 0.95 and 0.98. The left white dashed triangle indicates the region that satisfies the requirement $T^{(1)}_{\text{min}} = T^{(3)}_{\text{min}} = 25$ μs and $T^{(2)}_{\text{min}} = 50$ μs, which corresponds to the durations of rectangular $\pi/2$ and π pulses with the same amplitude. The plot employs a logarithmic color scale.

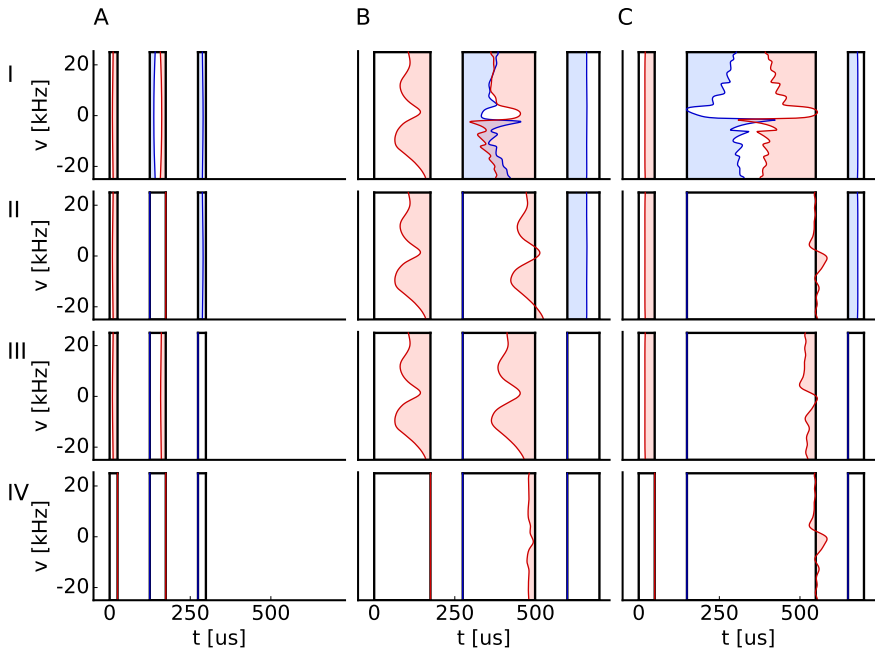

Figure 7.26: Graphical representation of the effective evolution periods for a $\frac{\pi}{2} - \pi - \frac{\pi}{2}$ sequence composed of rectangular pulses with a total duration T^{tot} of 100 μs (A), COBBLE$_{50}^{500}$ echo and time-reversed and phase-shifted ICEBERG ($\delta^{\mathrm{ICEBERG}}/T^{\mathrm{ICEBERG}} = 0.6$) pulses with an auxiliary delay $\delta = 20$ μs (B), and individually optimized ICEBERG ($\delta^{\mathrm{ICEBERG}}/T^{\mathrm{ICEBERG}} = 0.6$) and BURBOP pulses (C). The total duration of (B) and (C) each amounts ot 500 μs. Panels I to IV correspond to the plot types introduced in section 6.3.5.

In Panel IV, $\tau_\alpha^{\prime\prime(2)}$ and $\tau_\alpha^{\prime\prime(1)}$ are condensed into a single curve $\tau_\alpha^{\prime\prime\prime(2)}$ at the trailing edge of the refocusing pulse.

Fig. 7.26 shows a sequence of rectangular pulses for a total duration of 100 μs with with $T^{(1)} = T^{(3)} = 25$ μs and $T^{(2)} = 50$ μs (A), a sequence with a COBBLE$_{40}^{400}$ sequence and a time-reversed and phase-shifted ICEBERG pulse ($\delta^{\mathrm{ICEBERG}}/T^{\mathrm{ICEBERG}} = 0.6$) with a duration $T^{(3)} = 100$ μs and an auxiliary delay $\delta = 20$ μs (B) and a sequence with an individually optimized BURBOP pulse with a duration $T^{(2)} = 800$ μs and an ICEBERG pulse ($\delta^{\mathrm{ICEBERG}}/T^{\mathrm{ICEBERG}} = 0.6$) with $T^{(1)} = T^{(3)} = 50$ μs.

Fig. 7.27 shows effective evolution periods of individually optimized BURBOP pulses with a $T^{(1)} = T^{(3)} = 40$ μs and $T^{(2)} = 430$ μs (A), a COBBLE3$_0^{500}$ sequence with $T^{(1)} = T^{(3)} = 125$ μs and $T^{(2)} = 250$ μs (B) and a sequence with individually optimized BEBOP excitation pulses with $T^{(1)} = T^{(3)} = 162.5$ μs and a BURBOP pulse with $T^{(2)} = 180$ μs.

Note the good match of the the effective evolution periods $\tau_\alpha^{(1)}$ and $\tau_\alpha^{\prime\prime(2)}$ of the excitation and refocusing pulses in the COBBLE sequences shown in panel III of Figs. 7.27 B.

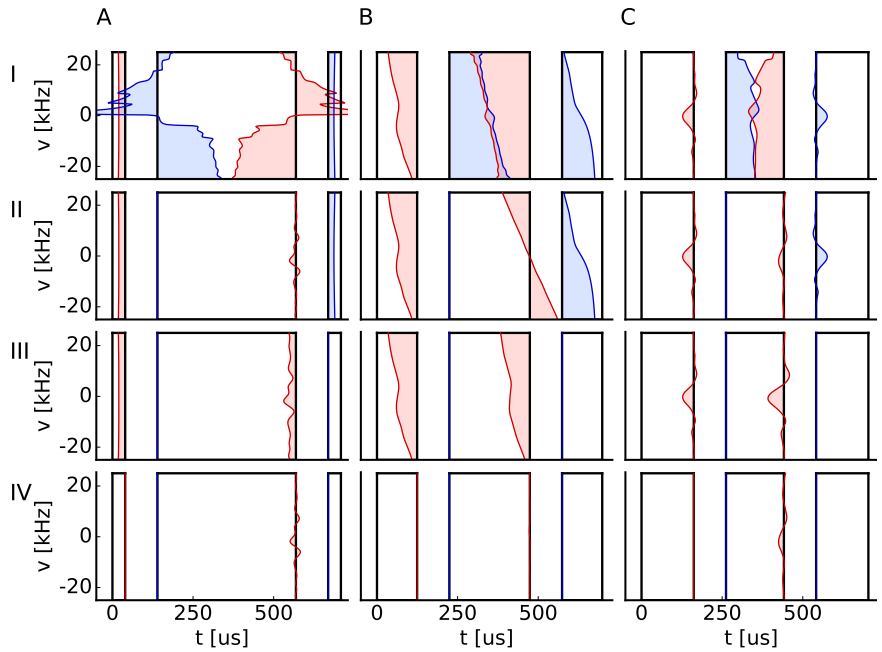

Figure 7.27: Graphical representation of the effective evolution periods for a $\frac{\pi}{2} - \pi - \frac{\pi}{2}$ sequence composed of individually optimized BURBOP pulses (A), a COBBLE3$_0^{500}$ sequence (B), and individually optimized BEBOP and BURBOP pulses (C). The total duration of (A), (B) and (C) each amounts to approx. 500 μs. Panels I to IV correspond to the plot types introduced in section 6.3.5.

This results in an overall $\tau_\alpha^{\prime\prime\prime(2)}$ in panel IV that is approximately offset independent, as desired.

7.2.6 Performance of different $\frac{\pi}{2} - \pi - \frac{\pi}{2}$ families

Here we compare the performance of the optimized COBBLE3 sequences with an echo sequence based on rectangular pulses and with conventional families of $\frac{\pi}{2} - \pi - \frac{\pi}{2}$ sequences discussed in section 6.3.4 in a similar fashion as Hahn echo sequences discussed in section 7.1.6. In order to compare the performance of COBBLE3 sequences with the performance of $\frac{\pi}{2} - \pi - \frac{\pi}{2}$ sequences consisting of combinations of

(A) individually optimized UR($\pi/2$) excitation and UR(π) refocusing pulses (c.f. section 6.2.4)

(B) individually optimized PP($z \rightarrow x$) excitation and UR(π) refocusing pulses (c.f. section 6.2.4),

(C) individually optimized ICEBERG($z \rightarrow \perp$) excitation and UR(π) refocusing pulses (c.f. section 6.2.4),

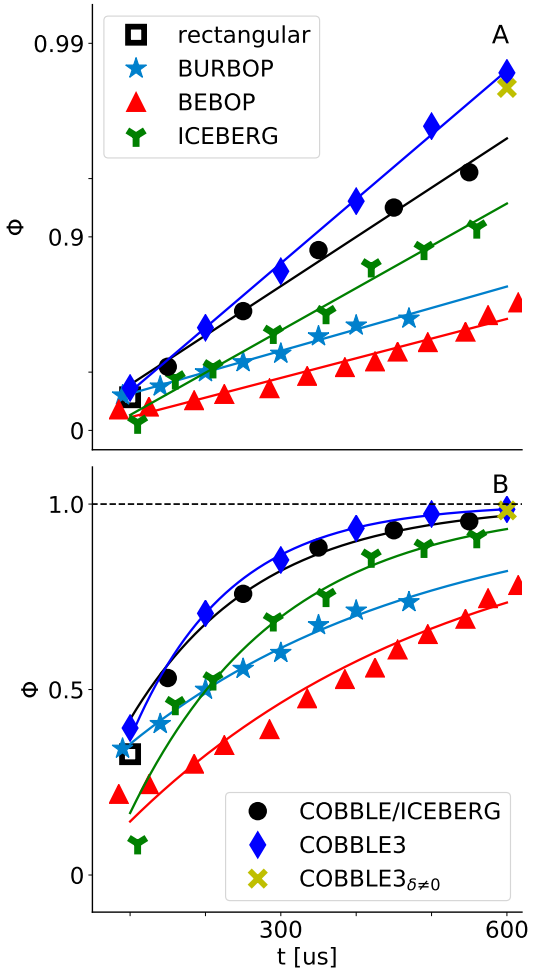

Figure 7.28: Maximum quality factor Φ plotted on a logarithmic (A) and linear (C) scale as a function of the total pulse duration T^{tot} for the optimal relative duration $T^{(1)}/T^{tot}$.

(D) individually optimized COBBLE pulses combined with individually optimized time-reversed and phase-shifted ICEBERG pulses

we determined the best combinations of individually optimized pulses with durations $T^{(1)}$, $T^{(2)}$ and $T^{(3)}$ for the considered total pulse durations T^{tot}. The COBBLE3 sequences employed here were optimized with the pre-optimization algorithm discussed in section 6.3.3 and correspond to those discussed in section 7.2.10.

Fig. 7.28 shows TOP curves of each family of pulses as a function of total pulse duration T^{tot}. For a given total pulse duration, the combination of ICEBERG excitation and BURBOP refocussing pulses are the best $\frac{\pi}{2} - \pi - \frac{\pi}{2}$ sequences based on individually optimized pulses, as expected based on the number of degrees of freedom (c.f. Table 6.4) and as expected from similar studies for Hahn echoes (c.f. Sec. 7.1.6). However,

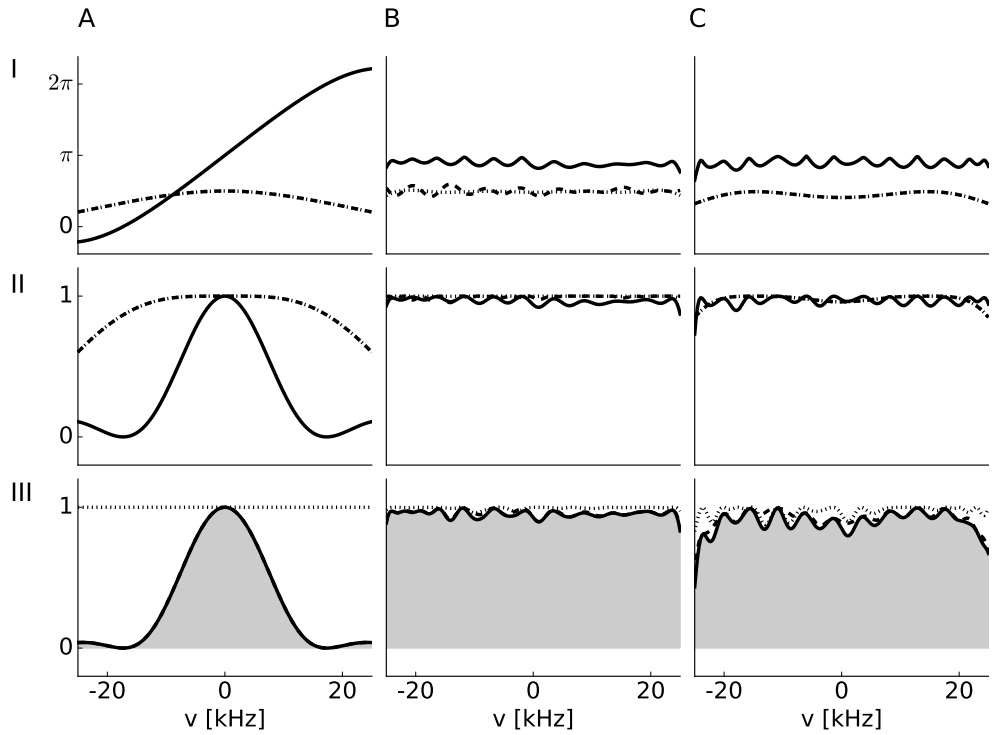

Figure 7.29: The figure shows the individual contributions to the offset-dependent local quality factor $\phi(\delta, \omega)$ (A) for a standard $\frac{\pi}{2} - \pi - \frac{\pi}{2}$ sequence composed of rectangular pulses with a total duration of 100 μs, (B) for a COBBLE$_{40}^{400}$ sequence shown in figure 7.21 D combined with a time-reversed and phase-shifted ICEBERG pulse with a total duration $T^{tot} = 500$ μs and (C) for an Echo sequence consisting of individually optimized ICEBERG and BURBOP pulses with a total duration of 500 μs. In panel I, the offset-dependent flip angles $\beta^{(1)}$ for $S^{(1)}$ (dashed curve), $\beta^{(2)}$ for $S^{(2)}$ (solid curve) and $\beta^{(3)}$ for $S^{(3)}$ (dotted curve) are displayed. In panel II, the absolute value $|f_1| = |\sin\ \beta^{(1)}|$ (dashed curve) of the transfer efficiency f_1 (c.f. Eq. 6.38) of the excitation pulse $S^{(1)}$, the absolute value $|f_2| = |\sin^2(\beta^{(2)}/2)|$ (solid curve) of the transfer efficiency f_2 (c.f. Eq. 6.41) of the refocusing pulse $S^{(2)}$ and the absolute value $|f_3| = |\sin\beta^{(3)}|$ (dotted curve) (c.f. Eq. 6.80) are shown. In panel III, the absolute value of the overall transfer efficiency $|f_1 \cdot f_2 \cdot f_3|$ (dashed curve), the phase fidelity $\cos\varphi$ (dotted curve) and the offset-dependent local quality factor $\phi(\delta, \omega)$ defined in Eq. (7.6) are plotted. The real value of the transfer function (Eq. 6.64) is shown as a solid black curve.

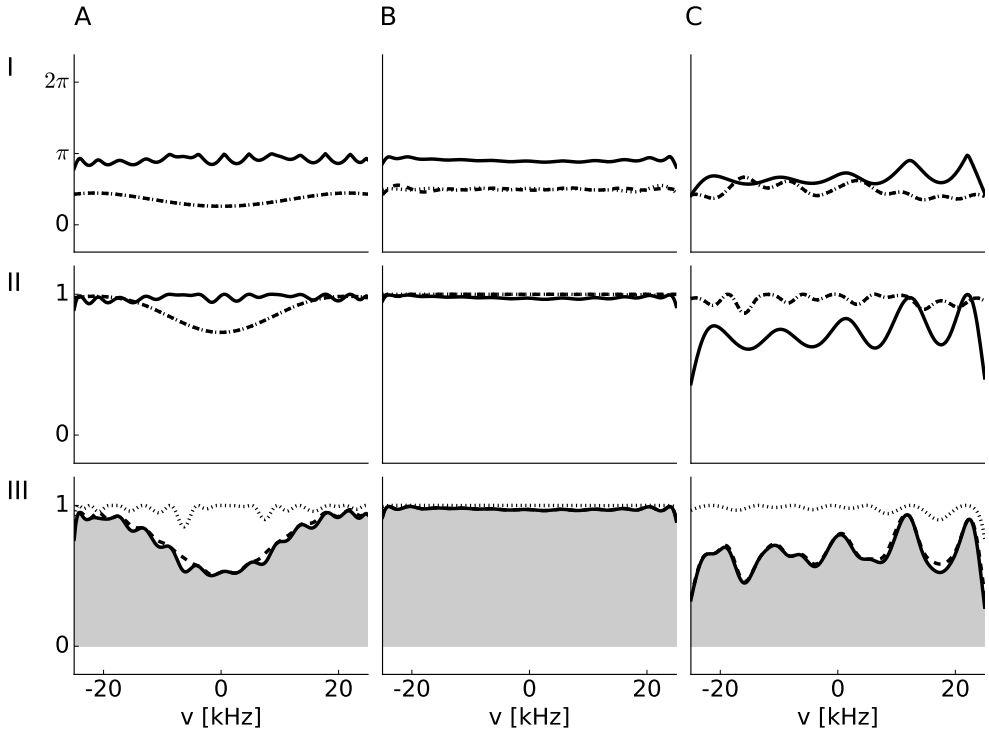

Figure 7.30: The figure shows the individual contributions to the offset-dependent local quality factor $\phi(\delta, \omega)$ (A) for a $\frac{\pi}{2} - \pi - \frac{\pi}{2}$ sequence composed of BURBOP pulses with a total duration of 500 μs, (B) for a COBBLE3$_0^{500}$ sequence shown in figure 7.34 D and (C) for an Echo sequence consisting of individually optimized BEBOP and BURBOP pulses with a total duration of 510 μs. In panel I, the offset-dependent flip angles $\beta^{(1)}$ for $S^{(1)}$ (dashed curve), $\beta^{(2)}$ for $S^{(2)}$ (solid curve) and $\beta^{(3)}$ for $S^{(3)}$ (dotted curve) are displayed. In panel II, the absolute value $|f_1| = |\sin\ \beta^{(1)}|$ (dashed curve) of the transfer efficiency f_1 (c.f. Eq. 6.38) of the excitation pulse $S^{(1)}$, the absolute value $|f_2| = |\sin^2(\beta^{(2)}/2)|$ (solid curve) of the transfer efficiency f_2 (c.f. Eq. 6.41) of the refocusing pulse $S^{(2)}$ and the absolute value $|f_3| = |\sin\beta^{(3)}|$ (dotted curve) (c.f. Eq. 6.80) are shown. In panel III, the absolute value of the overall transfer efficiency $|f_1 \cdot f_2 \cdot f_3|$ (dashed curve), the phase fidelity $\cos\varphi$ (dotted curve) and the offset-dependent local quality factor $\phi(\delta, \omega)$ defined in Eq. (7.6) are plotted. The real value of the transfer function (Eq. 6.64) is shown as a solid black curve.

Table 7.4: Global quality factors Φ of different families of optimized pulses with a total duration $T^{tot} \approx 500$ μs and of a standard $\frac{\pi}{2} - \pi - \frac{\pi}{2}$ sequences consisting of rectangular pulses with a total duration T^{tot} of 100 μs.

echo sequence	T^{tot} [μs]	Φ
rectangular	100	0.33
BURBOP/BURBOP	590	0.77
BEBOP/BURBOP	505	0.67
ICEBERG/BURBOP	500	0.92
COBBLE_{40}^{400}/ICEBERG	500	0.96
COBBLE3_{0}^{500}	500	0.97

in contrast to Hahn echo sequences, the performance of $\frac{\pi}{2} - \pi - \frac{\pi}{2}$ sequences comprised of individually optimized BURBOP pulses surpasses the performance of BEBOP pulses combined with a BURBOP refocusing pulse. This is in contrast to what is expected from table 6.4. We attribute that to the fact that the flip angle $\beta^{(1)} = \beta^{(3)}$ for BURBOP sequences is closer to the ideal value of $\pi/2$ over the considered offset range (c.f. Fig. 7.30). At the same time, short BURBOP pulses introduce additional effective evolution periods (c.f. Fig. 7.27), i.e. errors to $\gamma^{(1)}$ and $\alpha^{(3)}$. While it is not possible to mutually compensate for errors in the flip angles $\beta^{(1)}$ and $\beta^{(3)}$, both linear and non-linear errors in $\alpha^{(1)}$ and $\gamma^{(3)}$ can compensate each other, when a pulse is combined with its time-reversed and phase-shifted. In addition, note that for extended pulse durations beyond the scope shown in Fig. 7.28, BEBOP/BURBOP/BEBOP sequences surpass BURBOP/BURBOP/BURBOP sequences.

Considerable performance gains are obtained if COBBLE sequences are combined with individually optimized ICEBERG pulses. A minor gain over these is achieved for COBBLE3 sequences.

A quality factor of 0.7 is achieved with COBBLE3_{0}^{200} sequences, in order to achieve the same pulse duration with individually optimized ICEBERG and BURBOP pulses, a total pulse sequence duration $T^{tot} = 350$ μs is required.

Figs. 7.29 and 7.30 show the individual terms contributing to the offset-dependent local quality factor $\phi(\omega)$ for $\frac{\pi}{2} - \pi - \frac{\pi}{2}$ sequences of interest. In each of these figures, the top panel depicts the offset-dependent Euler angles $\beta^{(1)}(\omega)$ (solid curve), $\beta^{(2)}(\omega)$ (dashed curve) and $\beta^{(3)}$ (dotted curve) of the $S^{(1)}$, $S^{(2)}$ and $S^{(3)}$ pulses, respectively. The middle panel shows the absolute values $|f_1(\omega)| = \sin\beta^{(1)}$ (solid curve) $|f_2(\omega)| = \sin^2(\beta^{(2)}/2)$ (dashed curve) and $|f_3(\omega) = \sin\beta^{(3)}|$ of the partial quality factors defined in Eqs. (6.38), (6.41) and (6.80). The bottom panel shows the product $|f_1(\omega)| \cdot |f_2(\omega)| \cdot |f_3(\omega)|$ (dashed curve), which according to Eq. (7.5) is identical to $|s(\omega)|$. The dotted curve represents the term $\cos\varphi(\omega)$

$$\varphi(\omega) = \omega\delta - \alpha^{(1)}(\omega) + \alpha''^{(2)}(\omega), \tag{7.5}$$

which is the offset dependent phase of the transfer function at the auxiliary delay δ. The

solid curve shows the resulting offset-dependent local quality factor, which according to Eq. (7.6) is given by

$$\begin{aligned} \phi(\omega) &= \mathrm{Re}\{\ |s(t',\omega)|\ \exp(i\varphi(\omega))\ \} \\ &= |s(t',\omega)|\ \cos(\varphi(\omega)). \end{aligned} \tag{7.6}$$

The real value of the overall transfer function is represented by a solid black curve.

7.2.7 Impulse-response compensation

As outlined in section 4.4.7 the impulse response of an EPR spectrometer occurs on similar timescale as the individual time slices of a shaped pulse. Therefore, it cannot be neglected in all cases. A general procedure for pulse (sequence) optimization that considers the impulse response function of an apparatus was presented in section 4.4.7. [87]

In Fig. 7.31 we present results for a COBBLE3$_0^{1200}$ sequence that was optimized for characterizing charge transport complexes in phosphorus doped silicon. [151]

We considered an offset range of ±10 kHz and at a maximum RF amplitude of 10 kHz. The pulse sequence was discretized in steps of 1 μs. The corrsponding impulse response function that characterize the apparatus is shown in Fig. 7.31 E.

In Fig. 7.31 A and B we depict final z-magnetization after a COBBLE3$_0^{1200}$ sequence that was optimized for said impulse response (solid curve) and an equally long COBBLE3$_0^{1200}$ sequence optimized for a δ-shaped impulse response (dashed curve) without (A) and with considering the impulse response depicted in Fig. 7.31 E (B).

When no impulse response is considered, the sequence not optimized for impulse response compensation shows superior performance compared to the COBBLE3$_0^{1200}$ sequence optimized for impulse response compensation. In case that pulse distortions are acknowledged in the simulation, the compensated COBBLE3 sequence provides a nigh offset independent transfer to the desired target magnetization M_z.

The undistorted and distorted controls are shown in Fig. 7.31 C and D, respectively, where the solid curve represents the x-component and the dashed curve the y-component. Solid black lines separate the $S^{(1)}$, $S^{(2)}$ and $S^{(3)}$ pulse.

7.2.8 Band-selective pulse sequences

For Applications in EPR spectroscopy where charge transfer between pairs of spins is observed, it is necessary to confine excitation to one spin of the spin pair. [151] This is achieved by band selective pulses.

In section 6.3.6 a method to create band-selective pulses was reviewed. A COBBLE3$'^{1200}$ sequence where $T^{(1)} = T^{(2)} = T^{(3)} = 400$ μs was optimized according to Eq. (4.30) and (4.31) for a bandwidth of ±10 kHz with a maximum amplitude of 10 kHz. Frequencies $|\nu| > 20$ kHz $= \nu_{\mathrm{limit}}$ were removed.

Figure 7.32 shows z-magnetization for a bandselective (A) and non-selective (B) COBBLE3$_0^{1200}$ sequence. In the transition region for 10 kHz $\leq |\nu| \leq 20$ kHz for which no target magnetization is specified, final z-magnetization is not homogeneous. Within the

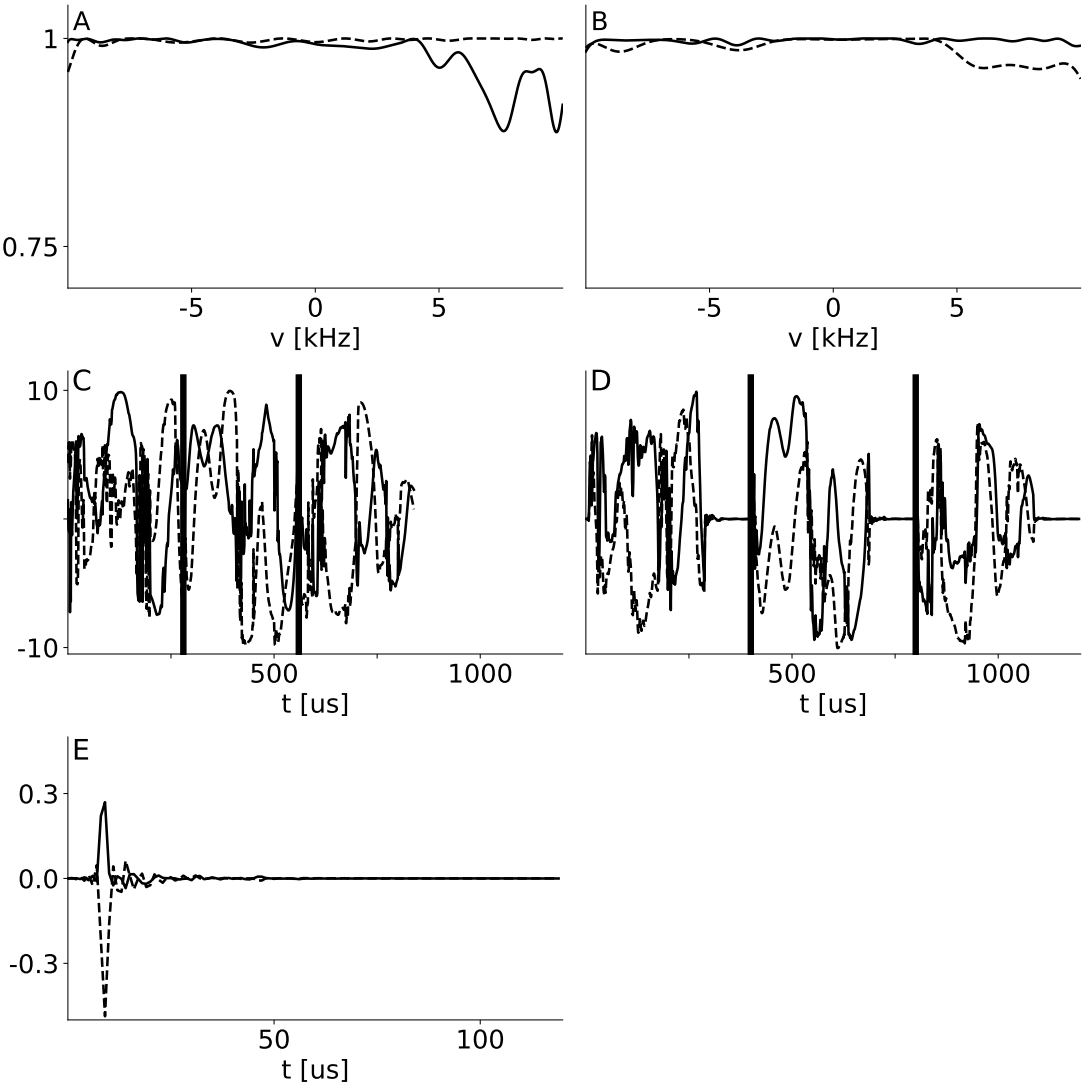

Figure 7.31: The effect of a non δ-shaped impulse response function is shown here. Subplot A shows the z-component of magnetization after a COBBLE3$_0^{1200}$ sequence over a bandwidth of 20 kHz with a maximum amplitude of 10 kHz that is not specifically optimized for the impulse response shown in E (the solid curve represents the x-component, the dashed curve the y-component of the impulse response function) (dashed curve) and of a sequence that is optimized for said impulse response (solid curve). Subplot B shows similar data when the impulse response depicted in E is considered. Subplots C shows the undistorted x-component (solid curve) and the y-component (dashed curve) of the COBBLE3$_0^{1200}$ sequence tuned for the aforementioned impulse response, subplot D shows the same sequence distorted by the considered impulse response function. The limits between individual pulses $S^{(1)}$, $S^{(2)}$ and $S^{(3)}$ are indicated by solid black lines.

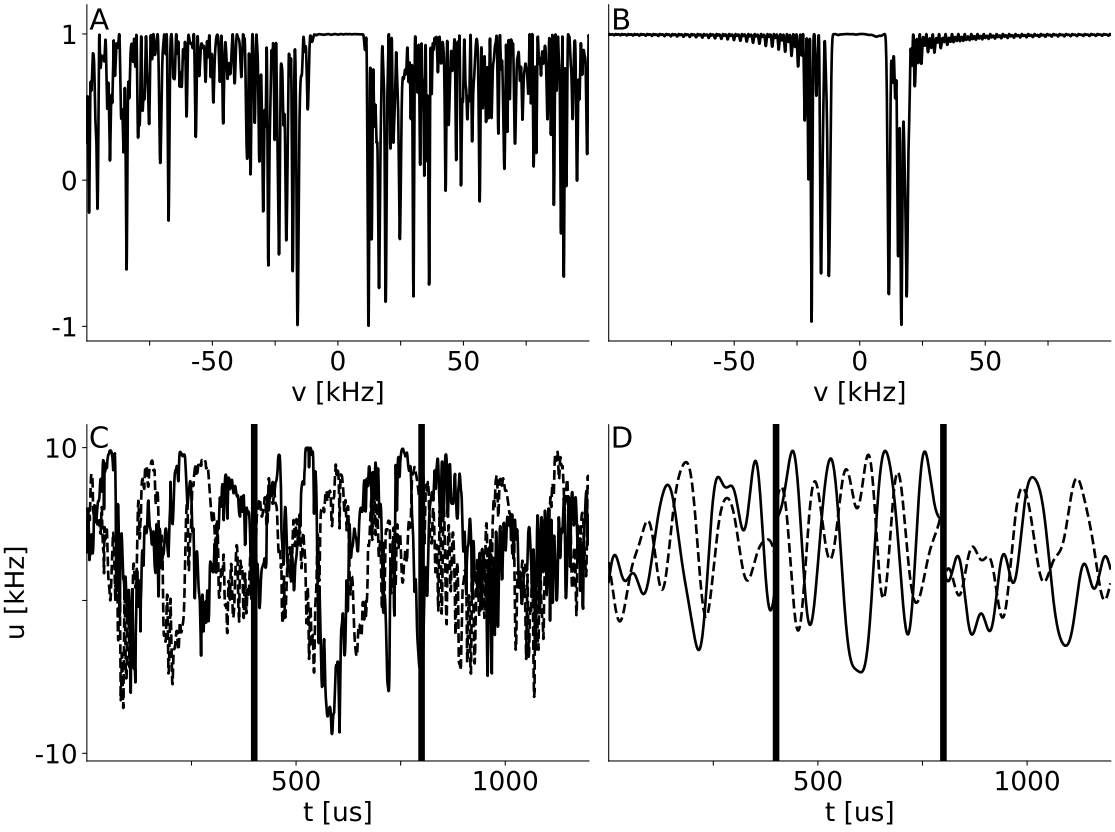

Figure 7.32: Here we depict z-magnetization after a COBBLE3$_0^{1200}$ sequence (A) which was optimized for a bandwidth of 20 kHz over ±100 kHz. In (B) we show a COBBLE3$_0^{1200}$ sequence optimized for the same bandwidth where all frequencies exceeding ±20 kHz were removed from the pulses. In (C) and (D) the x-component (solid curve) and the y-component of the rf pulse of the unfiltered and the filtered sequence are shown, respectively.

optimized region and in the region $|\nu| > \nu_{\text{limit}}$ magnetization is aligned nigh uniformly along z.

In Fig. 7.32 C and D, we show the x-component (solid curve) and the y-component (dashed curve) of the rf pulse of the non-selective and the band-selective COBBLE3$_0^{1200}$ sequence, respectively. Fig. 7.32 D illustrates that removing high frequency component from a pulse has the added advantage that the pulse becomes smooth.

7.2.9 Spectrograms

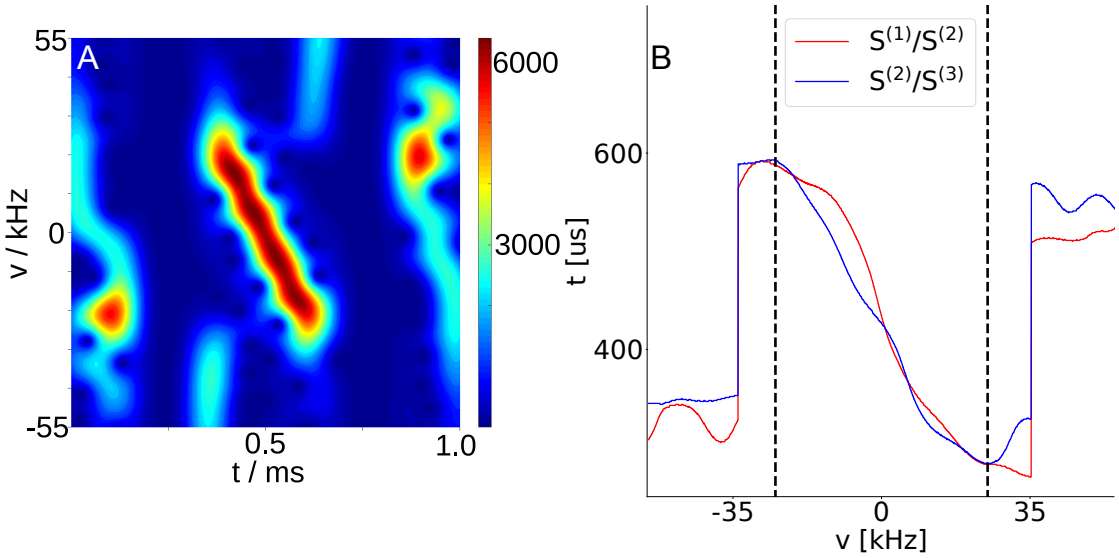

Figure 7.33: Here a joint time-frequency representation of a COBBLE3$_0^{600}$ sequence (A) (c.f. Fig. 7.34) is shown. $\tau^{(1,2)}$ and $\tau^{(2,3)}$ were set to 200 μs. The sequence was optimized for $\pm$25 kHz, the spectrogram representation covers a bandwidth of $\pm$55 kHz. In (B) we show the added position of the maxima of $S^{(1)}$ and $S^{(2)}$ (red curve) and $S^{(2)}$ and $S^{(3)}$ (blue curve). The former combination was incremented by a constant value of 80 μs. Dashed black curves signify the limits of the optimized range.

In section 7.1.11 COBBLE sequences were analyzed through a joint time-frequency representation. Here similar analysis is conducted for $\frac{\pi}{2} - \pi - \frac{\pi}{2}$ sequences.

Fig. 7.33 A shows a spectrogram for the COBBLE3$_0^{600}$ sequence depicted in Fig. 7.34 F. The pulse sequence was optimized for a bandwidth of $\pm$ 25 kHz, the spectrogram was created for $\pm$55 kHz. $\tau^{(1,2)}$ and $\tau^{(2,3)}$ were set to 200 μs.

Within the optimized range, the sum of maxima of the $S^{(1)}$ and $S^{(2)}$ (red curve in Fig. 7.33 B) and the sum of the maxima of the $S^{(2)}$ and $S^{(3)}$ pulse (blue curve in Fig. 7.33) approximately match like a jigsaw.

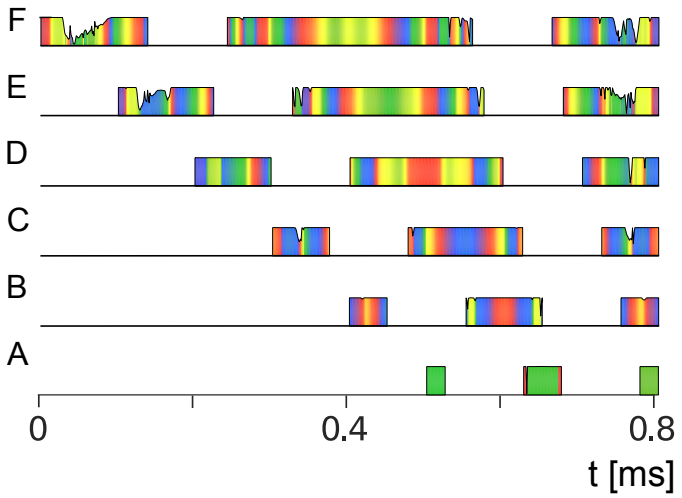

Figure 7.34: Here we depict $S^{(1)}$, $S^{(2)}$ and $S^{(3)}$ pulses of COBBLE3 sequences for $T^{tot} = T^{(1)} + T^{(2)} + T^{(3)}$ of (A) 100 μs, (B) 200 μs, (C) 300 μs, (D) 400 μs, (E) 500 μs, and (F) 600 μs. Arbitrary inter-pulse delays $\tau^{(1,2)} = \tau^{(2,3)}$ of 100 μs were inserted between the pulses in order to clearly separate them. The maximum rf amplitude was 10 kHz and the pulse phase is color coded (x: red, y: yellow, $-$x: green, $-$y: blue). The colormap is shown in Fig. 7.21.

7.2.10 Pulseshapes of $\frac{\pi}{2} - \pi - \frac{\pi}{2}$ sequences

In section 7.1.10 we studied the amplitude and phase modulation for COBBLE sequences. Here we conduct similar analysis for COBBLE3 sequences.

In Fig. 7.34 we show amplitude and phase modulation of (A) a COBBLE3$_0^{100}$, (B) a COBBLE3$_0^{200}$, (C) a COBBLE3$_0^{300}$, (D) a COBBLE3$_0^{400}$, (E) a COBBLE3$_0^{500}$ and (F) a COBBLE3$_0^{600}$ sequence.

The minimum pulse sequence duration T^{tot} for a COBBLE3 sequence based on rectangular pulses is 100 μs. Case A corresponds to the case with minimum pulse duration and the optimization procedure converged into rectangular pulses with only minor phase variations.

Note that for $T^{tot} = 100, 200$ and 300 μs the $S^{(3)}$ pulse corresponds to the time-reverse of the $S^{(1)}$ pulse and for $T^{tot} = 400, 500$ and 600 μs, the phases in the second half of the $S^{(1)}$ pulse correspond to the time-reversed phases in the first half of the $S^{(3)}$ pulse. From the analysis conducted in section 6.3.1 we would have expected a reversal of the phases as well.

The refocusing pulses appear to be highly symmetric. Symmetries in refocusing pulses and corresponding transfers are currently being investigated by Heydenreich et al.[156] Future work might consider symmetries in cooperative pulse sequences.

8 Conclusion

Here we extended the concept of single-scan cooperative pulses to broadband Hahn echo and $\frac{\pi}{2} - \pi - \frac{\pi}{2}$ sequences consisting of concurrently optimized broadband excitation and refocusing pulses. This is in contrast to Hahn echo and $\frac{\pi}{2} - \pi - \frac{\pi}{2}$ sequences based on individually optimized excitation and refocusing pulses. The concurrent cooperative optimization of excitation and refocusing pulses is also conceptionaly different from echo and $\frac{\pi}{2} - \pi - \frac{\pi}{2}$ sequences in which first one pulse (e.g. the refocusing pulse) is individually optimized and where the overall signal performance is increased by optimizing a second pulse (e.g. the excitation pulse) such that it is optimally adapted to the given pulse (e.g. the refocusing pulse).[157] Compared to the adaption of e.g. excitation pulses to a given refocusing pulse, the fully cooperative pulse sequence optimization treats both pulses on an equal footing. The possibility of pulses to mutually adapt in order to maximize the overall pulse sequence performance offers more degrees of freedom compared to the case, where only one pulse is allowed to adapt to a given individually optimized pulse.

In this study, we focused on the echo sequences in the presence of crusher gradients or EXORCYCLE phase cycling corresponding to the application of a +1-quantum filter after the excitation pulse and a −1-quantum filter after the refocusing pulse. In this case, the echo amplitude is independent of the inter-pulse delay if relaxation or diffusion effects are negligible. However, note that the COOP principle is not restricted to echo and $\frac{\pi}{2} - \pi - \frac{\pi}{2}$ sequences with coherence order pathway selection. COBBLE and COBBLE3 sequences also optimize the echo amplitude in experiments without crusher gradients or phase cycling, albeit additional signal components created by the FIDs of the excitation and of the refocusing pulses are not filtered out in this case.

The following main results were obtained:

(a) We have found a highly efficient two-step optimization strategy, which avoids being trapped in local maxima which are present if the echo amplitude is optimized without considering the offset-dependent global phase of the refocusing propagator. The pre-optimization scheme for $\frac{\pi}{2} - \pi - \frac{\pi}{2}$ sequences is straightforward to adapt to experiments with multiple refocusing times.

(b) We have demonstrated that the additional degrees of freedom in COOP echo (COBBLE) and $\frac{\pi}{2} - \pi - \frac{\pi}{2}$ (COBBLE3) sequences allow the algorithm to find sequences with significantly improved performance compared to individually optimized excitation and refocusing pulses for the same total pulse duration. (Conversely, the same performance of conventional echo sequences can be achieved with a significantly reduced total pulse duration.)

(c) The systematic study of the achievable Hahn echo and $\frac{\pi}{2} - \pi - \frac{\pi}{2}$ performance as a function of total pulse duration revealed a simple scaling law: For a given

bandwidth, maximum rf amplitude and rf inhomogeneity, the deviation from the ideal echo amplitude decreases exponentially with increasing total pulse duration.

(d) In contrast to conventional Hahn echo sequences based on hard pulses, for which the ratio of the durations of refocusing and excitation pulses is 2:1, for the best cooperative echo sequences this ratio is decreased to about 2:1.5. However, the dependence on this ratio is relatively flat and it is possible to further reduce the relative duration of the refocusing pulse without significantly reducing the echo performance. This may be beneficial for some applications, e.g. if minimal coupling evolution during refocusing pulses is desired. For cooperative $\frac{\pi}{2} - \pi - \frac{\pi}{2}$ sequences, the ideal ratio of the durations of the $S^{(1)}$, $S^{(2)}$ and $S^{(3)}$ pulses equal the ratios of the durations of the corresponding hard pulses.

(e) The optimized $\frac{\pi}{2} - \pi - \frac{\pi}{2}$ sequences can be made band-selective and accomodate transient effects in a straightforward manner by the same methods employed in individual pulse optimization.

(f) An intuitive graphical representation for the analysis of cooperative (and conventional) echo sequences was introduced based on Euler angles and associated effective evolution periods.

(g) For Hahn echo sequences, preliminary investigations indicate that the optimization converges into select families of pulse sequences that exhibit minuscule differences in amplitude and phase modulation. $\frac{\pi}{2} - \pi - \frac{\pi}{2}$ sequences show distinct symmetry properties.

For Hahn echo experiments, the increased overall signal amplitude is a result of a better phase alignment and/or a larger transverse component of the individual offset-dependent magnetization vectors at the time of the echo. For applications such as two-dimensional experiments, where frequency resolved signal contributions are measured, it may be desirable to further minimize the offset-dependent phase variations at the cost of a (slightly) decreased offset-dependent signal amplitude. This can be achieved by using a modified figure of merit in analogy to the cost function introduced by Skinner et al. [158] Furthermore, it is possible to minimize variations of offset-dependent signal amplitudes by defining the global quality factor not as the sum of the (potentially weighted) individual signal amplitudes but based on the squared difference between the signal amplitudes for each offset and the ideal (or averaged) signal amplitude. [159] In case of $\frac{\pi}{2} - \pi - \frac{\pi}{2}$ experiments, phase alignment is best defined in terms of mutual phase error compensation in the overall experiment, findings are similar to Hahn echos.

If the spin density is is not evenly distributed in the considered bandwidth, e.g. for broad powder patterns, a matched offset-dependent weighting factor could be included in Eq. (4.30). Further possible extensions of the presented approach include the design of highly selective (or band-selective) cooperative echo sequences. Although in this study we only considered limits of the available rf amplitude, well established approaches can be used to generalize this to constraints of pulse power or pulse energy [63] and to compensate for the effects of amplitude and phase transients. [86]

The broadband COOP echo and $\frac{\pi}{2} - \pi - \frac{\pi}{2}$ sequences presented here are directly applicable in experiments to measure diffusion constants and transverse relaxation rates [99] in NMR and EPR applications. In addition, we find that heteronuclear Ising couplings have negligible effects due to the offset-independent performance of the overall pulse sequence. In most cases that are of practical relevance, pseudosecular contributions are tolerated as well.

The presented approach can also be generalized for applications, where the excitation pulse is not supposed to bring the initial magnetization fully into the transverse plane. Examples are echo sequences with small flip angle excitation pulses in imaging. [160,161]

9 Acknowledgements

First and foremost I want to thank Prof. Dr. S. J. Glaser for the chance to write a thesis in his group, for the countless immensely valuable and clear, productive debates, your excellent guidance and letting me stray just enough.

The thesis at hand would not have been possible without the contributions of our collaborators.

In this respect I want to express my gratitude to Prof. Dr. M. S. Brandt and his group. A big thank you goes to him and Florian M. Hrubesch for the very fruitful collaboration and exchange on professional and non-professional matters.

Furthermore I thank Sam Asami for the successful collaboration on Ramsey experiments. Even though our joint efforts ended somewhat prematurely, I hope the optimization program is in a state that is of use to you.

A big thank you goes to my roommate Thomas Heydenreich for taking care of all the stuff that has to be done, but mostly go unnoticed. I do not know, how moving to the new building would have worked out without you. Thank you for the many distractions during some of the more tedious hours.

I want to thank Mrs Heinemann for all her help on administrative matters.

Thank you to Raimund for his immeasurably valuable help with the spectrometer.

A big thank you goes to all the people I met during P&P roleplaying for the tremendous amount of fun I had, for all the dramatic and whacky moments we shared.

I want to thank my family. They supported me in many ways before and during this endeavour.

Finally, I want to thank the DFG for the funding through the SPP 1601 project.

List of Figures

List of Tables

Bibliography

[1] Shaw, D. *Fourier Transform N.M.R. Spectroscopy*; Elsevier, 1976.

[2] Keeler, J. *Understanding NMR Spectroscopy*, 2nd ed.; John Wiley & Sons, Inc.: Weinheim, 2010.

[3] Ernst, R. R., Bodenhausen, G., and Wokaun, A. *Principles of Nuclear Magnetic Resonance in One and Two Dimensions*; Oxford University Press, 2014.

[4] Friebolin, H. *Ein- und zweidimensionale NMR-Spektroskopie*; Wiley: Weinheim, 2013; Vol. 5.

[5] Ledbetter, M. P., Crawford, C. W., Pines, A., Wemmer, D. E., Knappe, S., Kitching, J., and Budker, D. (2009) Optical detection of NMR J-spectra at zero magnetic field. *J Magn Reson 199*, 25–29.

[6] Mispelter, J., Lupu, M., and Briquet, A. *NMR Probeheads for Biophysical and Biomedical Experiments*; Imperial College Press, 2015.

[7] Braun, M., and Glaser, S. J. (2014) Concurrently optimized cooperative pulses in robust quantum control: application to broadband Ramsey-type pulse sequence elements. *New J. Phys 16*, 39.

[8] Gershenzon, N. I., Skinner, T. E., Khaneja, N., Luy, B., Glaser, S. J., and Brutscher, B. (2008) Linear Phase Slope in pulse design: Application to coherence transfer. *J Magn Reson 192*, 235–243.

[9] Köcher, S. S., Heydenreich, T., and Glaser, S. J. (2014) Visualization and analysis of modulated pulses in magnetic resonance by joint timefrequency representations. *J Magn Reson 249*, 63–71.

[10] Svanberg, S. *Atomic and Molecular Spectroscopy*; Springer, 2004.

[11] Pauli, W. (1924) Zur Frage der theoretischen Deutung der Satelliten einiger Spektrallinien und ihrer Beeinflussung durch magnetische Felder. *Naturwissenschaften 12*, 741–743.

[12] Bloch, F. (1946) Nuclear Induction. *Phys. Rev 70*, 460–474.

[13] Purcell, E. M., Torrey, H. C., and Pound, R. V. (1946) Resonance Absorption by Nuclear Magnetic Moments in a Solid. *Phys. Rev 69*, 37–38.

[14] Spindler, P. E., Schöps, P., Kallies, W., Glaser, S. J., and Prisner, T. F. (2017) Perspectives of shaped pulses for EPR spectroscopy. *J Magn Reson 280*, 30–45.

[15] Schatz, G. C., and Ratner, M. A. Quantum Mechanics in Chemistry. 2002.

[16] Goldman, M. *Quantum Description of High-Resolution NMR in Liquids*; International Series of Monographs on Chemistry; Clarendon Press: Oxford, 1988; Vol. 15.

[17] Atkins, P., and Friedman, R. *Molecular Quantum Mechanics*; Oxford university press, 2005.

[18] Wago, K., Botkin, D., Yannoni, C., and Rugar, D. (1998) Force-detected electron-spin resonance: Adiabatic inversion, nutation, and spin echo. *Phys. Rev. B 57*, 1108–1114.

[19] Mueller, L. J. (2011) Tensors and rotations in NMR. *Concepts Magn Reson Part A 38A*, 221–235.

[20] Blümich, B., and Spiess, H. W. (1985) Quaternions as a Practical Tool for the Evaluation of Composite Rotations. *J Magn Reson 61*, 356–362.

[21] Siminovitch, D. (1997) Rotations in NMR: 1. Euler-Rodrigues parameters and quaternions. *Concepts Magn Reson 9*, 149–171.

[22] Siminovitch, D. (1997) Rotations in NMR .2. Applications of the Euler-Rodrigues parameters. *Concepts Magn Reson 9*, 211–225.

[23] Millot, Y., and Man, P. P. (2012) Active and passive rotations with Euler angles in NMR. *Concepts Magn Reson Part A 40A*, 215–252.

[24] Khaneja, N., Brockett, R., and Glaser, S. J. (2001) Time Optimal Control in Spin Systems. *Phys Rev A 63*, 032308.

[25] Keeler, J. In *Multinuclear Magnetic Resonance in Liquids and Solids Chemical Applications*; Granger, P., and Harris, R. K., Eds.; Springer Netherlands: Dordrecht, 1990; pp 201–238.

[26] McDonald, S., and Warren, W. S. (1991) Uses of shaped pulses in NMR: A primer. *Concepts Magn Reson 3*, 55–81.

[27] Freeman, R. (1998) Shaped radiofrequency pulses in high resolution NMR. *Prog Nucl Magn Reson Spectrosc 32*, 59–106.

[28] Levitt, M. H., and Freeman, R. (1979) NMR population inversion using a composite pulse. *J Magn Reson 33*, 473–476.

[29] Levitt, M. H. (1986) Composite pulses. *Prog Nucl Magn Reson Spectrosc 18*, 61–122.

[30] Brown, K. R., Harrow, A. W., and Chuang, I. L. (2004) Arbitrarily accurate composite pulse sequences. *Phys Rev A 70*, 4.

[31] Counsell, C., Levitt, M. H., and Ernst, R. R. (1985) Analytical Theory of Composite Pulses. *J Magn Reson 63*, 133–141.

[32] Odedra, S., Thrippleton, M. J., and Wimperis, S. (2012) Dual-compensated antisymmetric composite refocusing pulses for NMR. *J Magn Reson 225*, 81–92.

[33] Koroleva, V. D. M., Mandal, S., Song, Y. Q., and Hurlimann, M. D. (2013) Broadband CPMG sequence with short composite refocusing pulses. *J Magn Reson 230*, 64–75.

[34] Odedra, S., and Wimperis, S. (2012) Use of composite refocusing pulses to form spin echoes. *J Magn Reson 214*, 68–75.

[35] Shaka, A. J. (1985) COMPOSITE PULSES FOR ULTRA-BROADBAND SPIN INVERSION. *Chem. Phys. Lett. 120*, 201–205.

[36] Xujie, Y., Keniry, M. A., and Sanctuary, B. C. (1993) Composite inversion pulses of short total duration. *J. Magn. Reson., Ser A 105*, 295–297.

[37] Xujie, Y., Jinsong, L., Baohua, G., Lude, L., Xin, W., and Sanctuary, B. C. (1995) Optimized phase-alternating composite pulse NMR. *Spectrosc. Lett. 28*, 1191–1201.

[38] Freeman, R., Kempsell, S. P., and Levitt, M. H. (1980) RADIOFREQUENCY PULSE SEQUENCES WHICH COMPENSATE THEIR OWN IMPERFECTIONS. *J Magn Reson 38*, 453–479.

[39] Haase, V. J. (1987) Composite pulses in nuclear magnetic resonance. *Ann. Phys. (Berl.) 44*, 507–513.

[40] Ichikawa, T., Bando, M., Kondo, Y., and Nakahara, M. (2012) Geometric aspects of composite pulses. *Philos. Trans. Royal Soc. B 370*, 4671–4689.

[41] Kabytayev, C., Green, T. J., Khodjasteh, K., Biercuk, M. J., Viola, L., and Brown, K. R. (2014) Robustness of composite pulses to time-dependent control noise. *Phys Rev A 90*, 9.

[42] Huerlimann, M. D. (2001) CarrPurcell Sequences with Composite Pulses. *J Magn Reson 152*, 109–123.

[43] Bunkenborg, J., Nielsen, N. C., and Sorensen, O. W. (2000) Doubling the sensitivity of natural abundance 13C-13C INADEQUATE with off-resonance compensation. *Magnetic Resonance in Chemistry 38*, 58–61.

[44] Tannus, A., and Garwood, M. (1997) Adiabatic pulses. *NMR Biomed 10*, 423–434.

[45] Michael Garwood, L. D. (2001) The Return of the Frequency Sweep: Designing Adiabatic Pulses for Contemporary NMR. *J Magn Reson 153*, 155 – 177.

[46] Rosenfeld, D., Panfil, S. L., and Zur, Y. (1997) Design of selective adiabatic inversion pulses using the adiabatic condition. *J Magn Reson 129*, 115–124.

[47] Cai, S., Zhang, W., and Chen, Z. (2009) High-Resolution Solution NMR Spectra in Inhomogeneous Magnetic Fields. *Curr Anal Chem 5*, 70–83.

[48] Kupce, E., and Freeman, R. (1995) Adiabatic Pulses for Wideband Inversion and Broadband Decoupling. *J. Magn. Reson., Ser A 115*, 273–276.

[49] Böhlen, J.-M., and Bodenhausen, G. (1993) Experimental Aspects of Chirp NMR Spectroscopy. *J Magn Reson 102*, 293–301.

[50] Janich, M. A., McLean, M. A., Noeske, R., Glaser, S. J., and Schulte, R. F. (2012) Slice-selective broadband refocusing pulses for the robust generation of crushed spin-echoes. *J Magn Reson 223*, 129–37.

[51] Upreti, S. R. Optimal Control for Chemical Engineers. 2013.

[52] Skinner, T. E., Reiss, T. O., Luy, B., Khaneja, N., and Glaser, S. J. (2003) Application of optimal control theory to the design of broadband excitation pulses for high-resolution NMR. *J Magn Reson 163*, 8–15.

[53] Stephens, C. R., and Cervantes, J. *Foundations of Genetic Algorithms*; Springer, 2007.

[54] Mitchell, M. *An introduction to genetic algorithms*; MIT Press, 1999.

[55] Pang, Y., and Shen, G. X. (2007) Improving excitation and inversion accuracy by optimized RF pulse using genetic algorithm. *J Magn Reson 186*, 86–93.

[56] Bechmann, M., Clark, J., and Sebald, A. (2013) Genetic algorithms and solid state NMR pulse sequences. *J Magn Reson 228*, 66–75.

[57] Zahedinejad, E., Schirmer, S., and Sanders, B. C. (2014) Evolutionary algorithms for hard quantum control. *Phys Rev A 90*, 032310.

[58] Speyer, J. L., and Jacobson, D. H. *Primer on optimal control*; SIAM, 2010.

[59] Khaneja, N., Reiss, T., Kehlet, C., Schulte-Herbrüggen, T., and Glaser, S. J. (2005) Optimal control of coupled spin dynamics: design of NMR pulse sequences by gradient ascent algorithms. *J Magn Reson 172*, 296–305.

[60] Machnes, S., Sander, U., Glaser, S. J., de Fouquières, P., Gruslys, A., Schirmer, S., and Schulte-Herbrüggen, T. (2011) Comparing, optimizing, and benchmarking quantum-control algorithms in a unifying programming framework. *Phys Rev A 84*, 022305.

[61] Kobzar, K. Optimal Control, Partial Alignment and More: The Design of Novel Tools for NMR Spectroscopy of Small Molecules. Ph.D. Thesis, 2007.

[62] Kobzar, K., Skinner, T. E., Khaneja, N., Glaser, S. J., and Luy, B. (2004) Exploring the limits of broadband excitation and inversion pulses. *J Magn Reson 170*, 236–43.

[63] Kobzar, K., Skinner, T. E., Khaneja, N., Glaser, S. J., and Luy, B. (2008) Exploring the limits of broadband excitation and inversion: II. Rf-power optimized pulses. *J Magn Reson 194*, 58–66.

[64] Skinner, T. E., Reiss, T. O., Luy, B., Khaneja, N., and Glaser, S. J. (2004) Reducing the duration of broadband excitation pulses using optimal control with limited RF amplitude. *J Magn Reson 167*, 68–74.

[65] Gershenzon, N. I., Kobzar, K., Luy, B., Glaser, S. J., and Skinner, T. E. (2007) Optimal control design of excitation pulses that accommodate relaxation. *J Magn Reson 188*, 330–336.

[66] Skinner, T. E., Gershenzon, N. I., Nimbalkar, M., and Glaser, S. J. (2012) Optimal control design of band-selective excitation pulses that accommodate relaxation and RF inhomogeneity. *J Magn Reson 217*, 53–60.

[67] Zhang, Y. Optimal Robust Pulse Design for Magnetic Resonance. Thesis, 2012.

[68] Nimbalkar, M., Luy, B., Skinner, T. E., Neves, J. L., Gershenzon, N. I., Kobzar, K., Bermel, W., and Glaser, S. J. (2013) The Fantastic Four: A plug 'n' play set of optimal control pulses for enhancing NMR spectroscopy. *J Magn Reson 228*, 16–31.

[69] Reddy, G. N., and Caldarelli, S. (2011) Maximum-quantum (MaxQ) NMR for the speciation of mixtures of phenolic molecules. *Chem Commun (Camb) 47*, 4297–9.

[70] Reddy, G. N., and Caldarelli, S. (2012) Identification and quantification of EPA 16 priority polycyclic aromatic hydrocarbon pollutants by Maximum-Quantum NMR. *Analyst 137*, 741–6.

[71] Köcher, S. S., Heydenreich, T., Zhang, Y., Reddy, G. N. M., Caldarelli, S., Yuan, H., and Glaser, S. J. (2016) Time-optimal excitation of maximum quantum coherence: Physical limits and pulse sequences. *J. Chem. Phys. 144*, 164103.

[72] Emsley, L., and Bodenhausen, G. (1992) Optimization of Shaped Selective Pulses for NMR Using a Quaternion Description of Their Overall Propagators. *J Magn Reson 97*, 135–148.

[73] Kobzar, K., Ehni, S., Skinner, T. E., Glaser, S. J., and Luy, B. (2012) Exploring the limits of broadband 90 degrees and 180 degrees universal rotation pulses. *J Magn Reson 225*, 142–160.

[74] Luy, B., Kobzar, K., Skinner, T. E., Khaneja, N., and Glaser, S. J. (2005) Construction of universal rotations from point-to-point transformations. *J Magn Reson 176*, 179–86.

[75] Köcher, S. Optimization of Unitary Rotation Double-ICEBERG Pulses by Euler Decomposition. Thesis, 2013.

[76] Van Damme, L., Ansel, Q., Glaser, S. J., and Sugny, D. (2017) Robust optimal control of two-level quantum systems. *Phys Rev A 95*, 063403.

[77] Braun, M. Cooperative Pulses: Towards Global Pulse Sequence Optimization. PhD, 2011.

[78] Braun, M., and Glaser, S. J. (2010) Cooperative pulses. *J Magn Reson 207*, 114–123.

[79] Neves, J. L., Heitmann, B., Khaneja, N., and Glaser, S. J. (2009) Heteronuclear decoupling by optimal tracking. *J Magn Reson* 7–17.

[80] Wei, D. X., Chang, Y., Glaser, S. J., and Yang, X. D. (2014) Cooperative pulses for pseudo-pure state preparation. *Appl. Phys. Lett. 104*, 5.

[81] Reinsperger, T., Schilling, F., Glaser, S. J., and Luy, B. The BROCODE of NMR: BROadband COoperative DEcoupling of Nuclear Spins. 2015.

[82] de Fouquieres, P., Schirmer, S. G., Glaser, S. J., and Kuprov, I. (2011) Second order gradient ascent pulse engineering. *J Magn Reson 212*, 412–7.

[83] Wächter, A., and Biegler, L. T. (2006) On the implementation of an interior-point filter line-search algorithm for large-scale nonlinear programming. *Math. Prog 106*, 25–57.

[84] Anand, C. K., Bain, A. D., Curtis, A. T., and Nie, Z. (2012) Designing Optimal Universal Pulses Using Second-Order, Large-Scale, Nonlinear Optimization. *J Magn Reson 219*, 61–74.

[85] Goodwin, D. L., and Kuprov, I. (2016) Modified Newton-Raphson GRAPE methods for optimal control of spin systems. *J. Chem. Phys. 144*, 204107.

[86] Spindler, P. E., Zhang, Y., Endeward, B., Gershernzon, N., Skinner, T. E., Glaser, S. J., and Prisner, T. F. (2012) Shaped optimal control pulses for increased excitation bandwidth in EPR. *J Magn Reson 218*, 49–58.

[87] Hincks, I. ., Granade, C. ., Borneman, T. ., and Cory, D. . (2015) Controlling Quantum Devices with Nonlinear Hardware. *Phys. Rev. Applied 4*, 024012.

[88] Tosner, Z., Vosegaard, T., Kehlet, C., Khaneja, N., Glaser, S. J., and Nielsen, N. C. (2009) Optimal control in NMR spectroscopy: numerical implementation in SIMPSON. *J Magn Reson 197*, 120–34.

[89] Johansson, J. R., Nation, P. D., and Nori, F. (2012) QuTiP: An open-source Python framework for the dynamics of open quantum systems. *Comput. Phys. Commun. 183*, 1760–1772.

[90] Johansson, J. R., Nation, P. D., and Nori, F. (2013) QuTiP 2: A Python framework for the dynamics of open quantum systems. *Comput. Phys. Commun. 184*, 1234–1240.

[91] Hogben, H. J., Krzystyniak, M., Charnock, G. T. P., Hore, P. J., and Kuprov, I. (2011) Spinach A software library for simulation of spin dynamics in large spin systems. *J Magn Reson 208*, 179–194.

[92] Wan, X., Parker, D. L., Lee, J. N., Buswell, H. R., and Gullberg, G. T. (1995) Reduction of phase error ghosting artifacts in thin slice fast spin-echo imaging. *Magn Reson Med 34*, 632–8.

[93] Walderhaug, H., Soderman, O., and Topgaard, D. (2010) Self-diffusion in polymer systems studied by magnetic field-gradient spin-echo NMR methods. *Prog Nucl Magn Reson Spectrosc 56*, 406–25.

[94] Van Lokeren, L., Ben Sassi, H., Van Assche, G., and Ribot, F. (2013) Quantitative analysis of polymer mixtures in solution by pulsed field-gradient spin echo NMR spectroscopy. *J Magn Reson 231*, 46–53.

[95] Occhipinti, P., and Griffiths, P. C. (2008) Quantifying diffusion in mucosal systems by pulsed-gradient spin-echo NMR. *Adv Drug Deliv Rev 60*, 1570–82.

[96] Atta-Ur-Rahman, T. *Nuclear Magnetic Resonance: Basic Principles*; Springer: New York, 1986; Vol. 1.

[97] Atta-ur Rahman, T. *One And Two Dimensional NMR Spectoscopy*; Elsevier: Amsterdam, 1989.

[98] Braun, S., Kalinowski, H.-O., and Berger, S. *100 and More Basic NMR Experiments*; Wiley, 1996.

[99] Berger, S., and Braun, S. *200 and More NMR Experiments*; Wiley, 2004.

[100] Cano, K. E., Smith, M. A., and Shaka, A. J. (2002) Adjustable, Broadband, Selective Excitation with Uniform Phase. *J Magn Reson 155*, 131–139.

[101] Schöps, P., Spindler, P. E., Marko, A., and Prisner, T. F. (2015) Broadband spin echoes and broadband SIFTER in EPR. *J Magn Reson 250*, 55–62.

[102] Jeschke, G., Pribitzer, S., and Doll, A. (2015) Coherence Transfer by Passage Pulses in Electron Paramagnetic Resonance Spectroscopy. *J. Phys. Chem. B 119*, 13570–13582.

[103] Bernstein, M., Kevin, K., and Zhou, Z. *Handbook of MRI Pulse Sequences*; Elsevier, 2004.

[104] Jung, B. A., and Weigel, M. (2013) Spin echo magnetic resonance imaging. *J Magn Reson Imaging 37*, 805–17.

[105] Bitar, R., Leung, G., Perng, R., Tadros, S., Moody, A. R., Sarrazin, J., McGregor, C., Christakis, M., Symons, S., Nelson, A., and Roberts, T. P. (2006) MR Pulse Sequences: What Every Radiologist Wants to Know but Is Afraid to Ask. *Radiographics 26*, 513–537.

[106] Boyle, G. E., Ahern, M., Cooke, J., Sheehy, N. P., and Meaney, J. F. (2006) An Interactive Taxonomy of MR Imaging Sequences. *Radiographics 26*.

[107] Sodickson, A., Mortele, K. J., Barish, M. A., Zou, K. H., Thibodeau, S., and Tempany, C. M. (2006) Three-dimensional fast-recovery fast spin-echo MRCP: comparison with two-dimensional single-shot fast spin-echo techniques. *Radiology 238*, 549–59.

[108] Janich, M. A., Schulte, R. F., Schwaiger, M., and Glaser, S. J. (2011) Robust slice-selective broadband refocusing pulses. *J Magn Reson 213*, 126–135.

[109] Sasaki, K., Ito, K., Koike, S., Fujita, T., Okazaki, H., and Matsunaga, N. (2005) Differentiation between hepatic cyst and hemangioma: additive value of breath-hold, multisection fluid-attenuated inversion-recovery magnetic resonance imaging using half-Fourier acquisition single-shot turbo-spin-echo sequence. *J Magn Reson Imaging 21*, 29–36.

[110] Sasaki, K., Ito, K., Fujita, T., Shimizu, A., Yasui, M., Hayashida, M., Tanabe, M., and Matsunaga, N. (2007) Small hepatic lesions found on single-phase helical CT in patients with malignancy: diagnostic capability of breath-hold, multisection fluid-attenuated inversion-recovery (FLAIR) MR imaging using a half-fourier acquisition single-shot turbo spin-echo (HASTE) sequence. *J Magn Reson Imaging 25*, 129–36.

[111] Bhosale, P., Kwek, J., Iyer, R., Wei, W., Bassett, R., and Kundra, V. (2011) Follow-Up of Known Carcinoid Liver Metastases: Is Respiratory-Gated T2 Fast Spin-Echo Enough? *Neuroendocrinology 93*, 241–248.

[112] Fukukura, Y., Kamiyama, T., Takumi, K., Shindo, T., Higashi, R., and Nakajo, M. (2010) Comparison of ferucarbotran-enhanced fluid-attenuated inversion-recovery echo-planar, T2-weighted turbo spin-echo, T2*-weighted gradient-echo, and diffusion-weighted echo-planar imaging for detection of malignant liver lesions. *J Magn Reson Imaging 31*, 607–16.

[113] Yoshikawa, T., Mitchell, D. G., Hirota, S., Ohno, Y., Oda, K., Maeda, T., Fujii, M., and Sugimura, K. (2006) Gradient- and spin-echo T2-weighted imaging for SPIO-enhanced detection and characterization of focal liver lesions. *J Magn Reson Imaging 23*, 712–9.

[114] van den Bos, I. C., Hussain, S. M., Krestin, G. P., and Wielopolski, P. A. (2008) Liver imaging at 3.0 T: diffusion-induced black-blood echo-planar imaging with large anatomic volumetric coverage as an alternative for specific absorption rate-intensive echo-train spin-echo sequences: feasibility study. *Radiology 248*, 264–71.

[115] Bruegel, M., Gaa, J., Woertler, K., Ganter, C., Waldt, S., Hillerer, C., and Rummeny, E. J. (2007) MRI of the lung: value of different turbo spin-echo, single-shot turbo spin-echo, and 3D gradient-echo pulse sequences for the detection of pulmonary metastases. *J Magn Reson Imaging 25*, 73–81.

[116] Ba-Ssalamaha, A., Schick, S., Heimberger, K., Linnau, K. F., Schibany, N., Prokesch, R., and Trattnig, S. (2000) Ultrafast magnetic resonance imaging of the brain. *Magn Reson Imaging 18*, 237–43.

[117] Minati, L., and Wglarz, W. P. (2007) Physical foundations, models, and methods of diffusion magnetic resonance imaging of the brain: A review. *Concepts Magn Reson Part A 30A*, 278–307.

[118] Wolff, A. B., Pesce, L. L., Wu, J. S., Smart, L. R., Medvecky, M. J., and Haims, A. H. (2009) Comparison of spin echo T1-weighted sequences versus fast spin-echo proton density-weighted sequences for evaluation of meniscal tears at 1.5 T. *Skeletal Radiol 38*, 21–9.

[119] Gold, G. E., Busse, R. F., Beehler, C., Han, E., Brau, A. C., Beatty, P. J., and Beaulieu, C. F. (2007) Isotropic MRI of the knee with 3D fast spin-echo extended echo-train acquisition (XETA): initial experience. *AJR Am J Roentgenol 188*, 1287–93.

[120] Andreisek, G., White, L. M., Theodoropoulos, J. S., Naraghi, A., Young, N., Zhao, C. Y., Mamisch, T. C., and Sussman, M. S. (2010) Synthetic-echo time postprocessing technique for generating images with variable T2-weighted contrast: diagnosis of meniscal and cartilage abnormalities of the knee. *Radiology 254*, 188–99.

[121] Tuite, M. J., De Smet, A. A., Norris, M. A., and Orwin, J. F. (1997) Anteroinferior tears of the glenoid labrum: fat-suppressed fast spin-echo T2 versus gradient-recalled echo MR images. *Skeletal Radiol 26*, 293–7.

[122] Tello, R., Mitchell, P. J., Witte, D. J., and Thomson, K. R. (1998) Detection of renal arteries with fast spin-echo magnetic resonance imaging. *Australas Radiol 42*, 179–82.

[123] Schweiger, A. (1991) Pulsed Electron Spin Resonance Spectroscopy: Basic Principles, Techniques, and Examples of Applications[New Analytical Methods(43)]. *Angewandte Chemie International Edition in English 30*, 265–292.

[124] Schweiger, A., and Jeschke, G. *Principles of Pulse Electron Paramagnetic Resonance*; Oxford University Press, 2001.

[125] Saxena, S., and Freed, J. H. (1997) Absorption lineshapes in two-dimensional electron spin resonance and the effects of slow motions in complex fluids. *J Magn Reson 124*, 439–54.

[126] Saxena, S., and Freed, J. H. (1997) Theory of double quantum two-dimensional electron spin resonance with application to distance measurements. *J. Chem. Phys. 107*, 1317.

[127] Höfer, P., Grupp, A., Nebenführ, H., and Mehring, M. (1986) Hyperfine sublevel correlation (hyscore) spectroscopy: a 2D ESR investigation of the squaric acid radical. *Chem. Phys. Lett. 132*, 279–282.

[128] Pilbrow, J. R. (1996) ESR fundamentals. *Appl. Radiat. Isot. 47*, 1465–1470.

[129] Callaghan, P. T., Coy, A., Dormann, E., Ruf, R., and Kaplan, N. (1994) Pulsed-Gradient Spin-Echo ESR. *J. Magn. Reson., Ser A 111*, 127–131.

[130] Millhauser, G. L., and Freed, J. H. (1984) Two-dimensional electron spin echo spectroscopy and slow motions. *J. Chem. Phys. 81*, 37.

[131] Ohno, K. (1982) Application of ESR imaging to a continuous flow method for study on kinetics of short-lived radicals. *J Magn Reson 49*, 56–63.

[132] Milov, A. D., Pusep, A. Y., Dzuba, S. A., and Tsvetkov, Y. D. (1985) Electron spin echo as a method of ESR tomography. *Chem. Phys. Lett. 119*, 421–425.

[133] Sloop, D. J., Yu, H.-L., and Lin, T.-S. (1986) ESR imaging via electron spin echo and pulsed field gradient techniques. *Chem. Phys. Lett. 124*, 456–458.

[134] Sukhoroslov, A. A., Samoilova, R. I., and Milov, A. D. (1991) Application of electron spin echo ESR-tomography to study radical diffusion in porous media. *Appl. Magn. Reson. 2*, 577–586.

[135] Dikanov, S. A., and Tsvetkov, Y. D. *Electron Spin Echo Envelope Modulation (ESEEM) Spectroscopy*; CRC Press, 1992.

[136] Kasumaj, B., Dube, H., Zolch, N., Diederich, F., and Jeschke, G. (2012) Relaxation and modulation interference effects in two-pulse electron spin echo envelope modulation (ESEEM). *J Magn Reson 223*, 187–97.

[137] Milov, A. D., Maryasov, A. G., and Tsvetkov, Y. D. (1998) Pulsed electron double resonance (PELDOR) and its applications in free-radicals research. *Appl. Magn. Reson. 15*, 107–143.

[138] Reginsson, G. W. Distance and orientation measurements on nucleic acids using PELDOR and non-covalent spin-labeling. Thesis, 2010.

[139] Spindler, P. E., Glaser, S. J., Skinner, T. E., and Prisner, T. F. (2013) Broadband Inversion PELDOR Spectroscopy with Partially Adiabatic Shaped Pulses. *Angew. Chem. Int. Ed. 52*, 3425–3429.

[140] Tsvetkov, Y. D., Milov, A. D., and Maryasov, A. G. (2008) Pulsed electronelectron double resonance (PELDOR) as EPR spectroscopy in nanometre range. *Russian Chemical Reviews 77*, 487–520.

[141] Chen, X., McManus, H., and Kevan, L. *Electron Spin Resonance, Electron Nuclear Double Resonance, and Electron Spin-Echo Spectroscopic Studies of Argonne Premium Coals*; ACS, 1992; Vol. 229; pp 451–466.

[142] Doll, A., and Jeschke, G. (2014) Fourier-transform electron spin resonance with bandwidth-compensated chirp pulses. *J Magn Reson 246*, 18.

[143] Zhu, J.-M., and Smith, I. C. P. (1995) Selection of coherence transfer pathways by pulsed-field gradients in nmr spectroscopy. *Concepts Magn Reson 7*, 281–291.

[144] Cavanagh, J., Fairbrother, W. J., and Palmer III, A. G. *Protein NMR Spectroscopy: Principles and Practice*; Elsevier, 1996.

[145] Ballentine, L. E. *Quantum Mechanics: A Modern Development*; World Scientific Publishing, 1998.

[146] Bertini, S., Cacciatori, S. L., and Cerchiai, B. L. (2006) On the Euler angles for SU(N). *J. Math. Phys. 47*, 043510.

[147] Pauly, J., Le Roux, P., Nishimura, D., and Macovski, A. (1991) Parameter relations for the Shinnar-Le Roux selective excitation pulse design algorithm [NMR imaging]. *IEEE Trans Med Imaging 10*, 53–65.

[148] Singla, P., Mortari, D., and Junkins, J. (2005) How to avoid singularity when using Euler angles? *Adv Astronaut Sci 119*, 1409–1426.

[149] Lescop, E., Kern, T., and Brutscher, B. (2010) Guidelines for the use of band-selective radiofrequency pulses in hetero-nuclear NMR: Example of longitudinal-relaxation-enhanced BEST-type 1H15N correlation experiments. *J Magn Reson 203*, 190–198.

[150] Li, Y., Rance, M., and Palmer, A. G. (2014) Rotation operator propagators for time-varying radiofrequency pulses in NMR spectroscopy: Applications to shaped pulses and pulse trains. *J Magn Reson 248*, 105–114.

[151] Huebl, H., Hoehne, F., Grolik, B., Stegner, A. R., Stutzmann, M., and Brandt, M. S. (2008) Spin Echoes in the Charge Transport through Phosphorus Donors in Silicon. *Physical Review Letters 100*, 177602.

[152] Xu, D., King, K. F., Zhu, Y., McKinnon, G. C., and Liang, Z.-P. (2008) Designing Multichannel, Multidimensional, Arbitrary Flip Angle RF Pulses Using an Optimal Control Approach. *Magn. Reson. Med. 59*, 547–560.

[153] Conolly, S., Nishimura, D., and Macovski, A. (1986) Optimal Control Solutions to the Magnetic Resonance Selective Excitation Problem. *IEEE Transactions on Medical Imaging 5*, 106–115.

[154] Neves, J. L., Heitmann, B., Reiss, T. O., Schor, H. H., Khaneja, N., and Glaser, S. J. (2006) Exploring the limits of polarization transfer efficiency in homonuclear three spin systems. *J Magn Reson 181*, 126–34.

[155] Skinner, T. E., Kobzar, K., Luy, B., Bendall, M. R., Bermel, W., Khaneja, N., and Glaser, S. J. (2006) Optimal control design of constant amplitude phase-modulated pulses: application to calibration-free broadband excitation. *J Magn Reson 179*, 241–9.

[156] Heydenreich, T., and Glaser, S. J. in preparation.

[157] Mandal, S., Koroleva, V. D. M., Borneman, T. W., Song, Y.-Q., and Hürlimann, M. D. (2013) Axis-matching excitation pulses for CPMG-like sequences in inhomogeneous fields. *J Magn Reson 237*, 1–10.

[158] Skinner, T. E., Reiss, T. O., Luy, B., Khaneja, N., and Glaser, S. J. (2005) Tailoring the optimal control cost function to a desired output: application to minimizing phase errors in short broadband excitation pulses. *J Magn Reson 172*, 17–23.

[159] Schilling, F., and Glaser, S. J. (2012) Tailored real-time scaling of heteronuclear couplings. *J Magn Reson 223*, 207–18.

[160] Haase, A., Frahm, J., Matthaei, D., Hanicke, W., and Merboldt, K. D. (1986) FLASH imaging. Rapid NMR imaging using low flip-angle pulses. *J Magn Reson 67*, 258–266.

[161] Assländer, J., Glaser, S. J., and Hennig, J. (2016) Spin echoes in the regime of weak dephasing. *Magn Reson Med 75*, 150–160.